

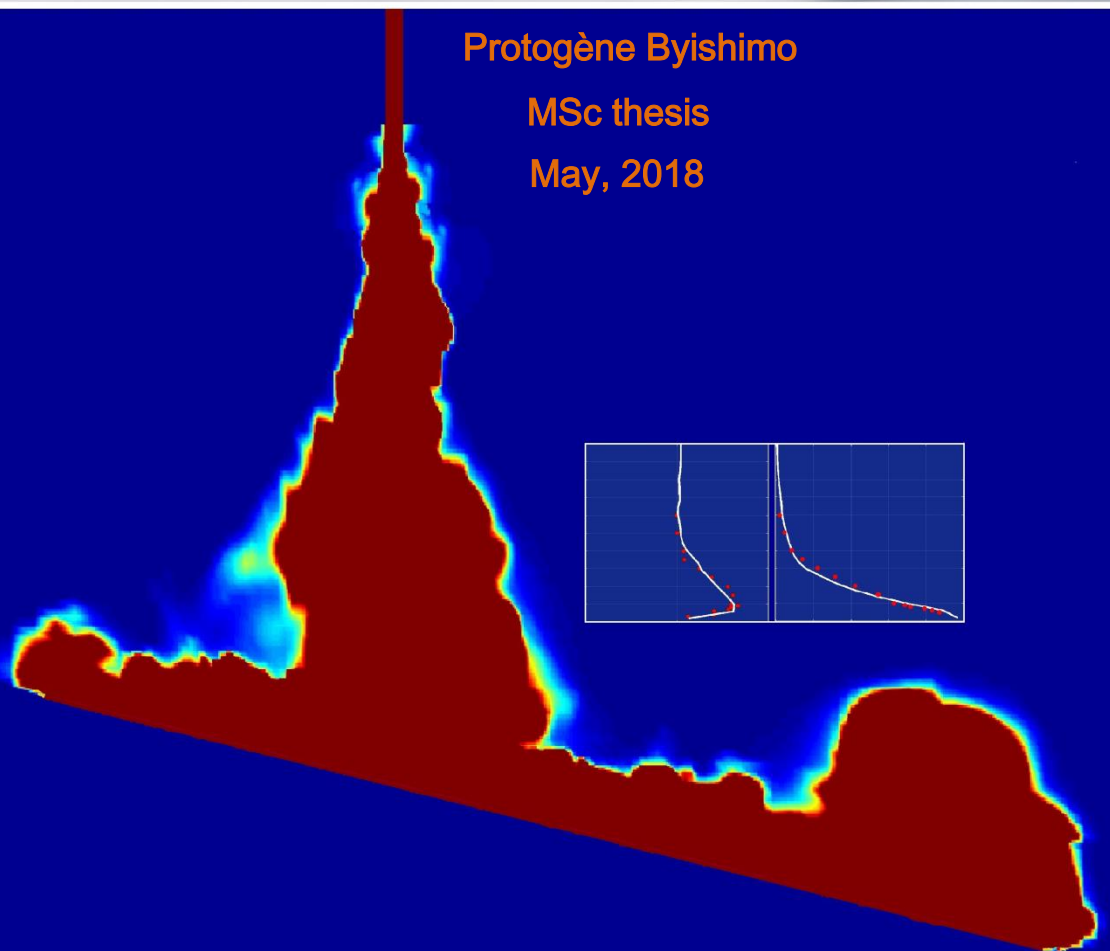


EXPERIMENTS AND 3D CFD SIMULATIONS OF DEEP-SEA  
MINING PLUME DISPERSION AND SEABED INTERACTIONS

Protogène Byishimo

MSc thesis

May, 2018





# EXPERIMENTS AND 3D CFD SIMULATIONS OF DEEP-SEA MINING PLUME DISPERSION AND SEABED INTERACTIONS

**Master of Science Thesis**

**By**

Protogène Byishimo  
Student number 4472640

**Supervisor**

Prof. dr. ir. C. van Rhee

**Mentors**

Ir. F. van Grunsven	- TU Delft
Dr. Ir. L. de Wit	- Svašek Hydraulics
Dr. Ir. Geert Keetels	-TU Delft

**Examination committee**

Prof. dr. ir. C. van Rhee	- TU Delft
Prof. dr. ir. C. Poelma	- TU Delft
Ir. F. van Grunsven	- TU Delft
Dr. Ir. L. de Wit	- Svašek Hydraulics
Dr. Ir. G. Keetels	-TU Delft

**The research was supported by**



**Delft**

**Friday, 18 May 2018**



# Summary

Growing markets for sustainable technologies such as solar panels, wind turbines, and electric cars require an enormous amount of raw materials that might not be available from sources on land. Exploitation of seafloor mineral resources could secure the supply of raw materials for the future. Proposed deep-sea mining (DSM) systems cut the crusts or collect the rock deposits containing minerals and transport the ore-seawater mixture to the support vessel at the sea surface. The ore is separated from the seawater and transported to a processing facility on land, whilst the wastewater containing fine sediments is returned back to the sea and released close to the seabed. Concerns are that the released sediment plume creates a significant pressure on various components of the mostly uncharted deep-sea ecosystem. The International Seabed Authority (ISA) is still busy developing an environmental license procedure. Accurate numerical models to predict the behavior of returned DSM plumes are still lacking.

This research aims to support environmental impact assessments for DSM operations. Laboratory tests were carried out to provide validation data for numerical models that can be used to predict the spreading of DSM plumes in the near-field domain. Additionally, a numerical technique called computational fluid dynamics (CFD) was used to analyse the laboratory simulations. Experiments and CFD calculations used a wide range of initial parameters: Three different DSM wastes release elevations relative to the bed, three different initial suspended sediment concentrations (SSC) at the source and two different bed slopes.

Results obtained from both experiments and CFD agreed well. Discharged negatively buoyant plumes fall vertically towards the bed where they impinge generating outwards flow turbidity currents. The velocity and SSC profiles predicted by the CFD model fit well the laboratory data taken inside the turbidity currents. It was observed that due to excess buoyancy gained by increasing the initial SSC at the discharge source led to a considerable increase of the dispersion rate of a formed turbidity current. Plumes release height from the bed was found to be an important parameter. Releasing plumes closer to the bed leads to the formation of a circular levee at a distance around the impingement point of about 10 times the orifice diameter. The formed sedimentation ring acts as a barrier against the turbidity current, which leads to the deposition of sediments on the bed outside the ring. As a consequence, the presence of a barrier reduced the plume dispersion rate thus returned DSM wastes stayed closer to the disposal location. In case the plume is released from a greater height, due to a longer falling distance and settling of particles, the generated turbidity current accelerated and the sediments particles were transported in suspension to a large distance from the disposal location.

The main goal of this research, to provide a unique set of validation data for numerical models, was achieved and a Large Eddy Simulation CFD model was successfully used, tested and approved for its capability to accurately predict the near-field spreading of DSM plumes. Based on obtained results, in order to minimise the environmental impacts, the velocity at the bed should be minimised preventing re-suspension of already deposited sediments. It is recommended that sediment waste and other effluents should be released close to the seabed. CFD model setup considered only sedimentation of particles and ignored erosion. Based on observed seabed morphology changes during the laboratory experiments, it is recommended that erosion should be considered within numerical models even for simplified laboratory experiments without a pre-existing bed. To fully predict the environmental impacts of DSM operations on a field scale, a near-field model used in this research should be coupled to a far-field model and a detailed study of multiple other environmental pressures is required.

**Keywords:** Deep-Sea Mining, sediment wastes disposal, jets and plumes spreading, turbidity current, sediment deposition.

# Acknowledgments

The successful completion of this MSc thesis work was a result of combined efforts. I would like to acknowledge the following:

I sincerely thank my family, my mother Georgette, my sisters Ernestine, Angelique, Josiane, and Sandrine, my brothers Augustin and Charles for their care, moral support and especially for accepting my absence for all these years I lived abroad far away from our family.

It is from the bottom of my heart that I would like to thank Amadea Gloudemans for her help and motivations. I would also like to thank her uncle and aunt Roland and Corry Coppens for helping me with a financial loan to pay for the extras needed in 2017.

I am deeply grateful to my daily mentor and friend Frans van Grunsven. I cannot but appreciate his constructive suggestions, discussions, and encouragement enough. He devoted much of his time in facilitating practical research and for the efficient supervision, help, and support. I am forever grateful. I would like to thank Svašek Hydraulics for their hospitality and collaboration during the time I spent at their company. I would like to acknowledge especially the supervision given by Dr. Ir. Lynyrd de Wit for my CFD simulation work. I appreciate how much time he spent helping me to modify the TUDflow3D code and make it applicable to my specific research case. It is an honor for me to express my sincere thanks to my supervisor Prof. Dr. ir. Cees van Rhee for his advice during my research. I also thank Dr. Ir. Geert Keetels for his critics, suggestions, and advice that helped me to improve my work.

I am thankful for the help by Sjoerd Warringa for helping with the laboratory experiments filming and image analysis. Also, I would like to thank staffs of the TU Delft dredging lab, Freek Brakel and Ed Stok for making their resources available to me to conduct my research. I appreciated the help they provided by doing their best to help in setting up the experimental setup.

My acknowledgments go to my academic advisor Mr. Evert Vixseboxse and the TU Delft Student Counsellors Suze-Anne van Geffen and John Stals for their mental support, motivation, and coaching that helped to study at TU Delft in a situation without a scholarship.

I am pleased and thankful for the friendships I received from new people I met at the TU Delft: Maria and Lennart Lems, Charlotte Spaargaren, Luuk van Dun, Karin Bremer. Also, other friends, I met in the Netherlands; Lieke Gouma and Suzanne van Hees. I appreciate the hospitality received from my Dutch family friends Marloes and Stephen Mans and their daughters Bente, Anneloes, Emma, and Juliet. I appreciate the support given by Leonie Zweekhorst and Waltraut Stroh during my first-year study at TU Delft. They were all very kind people to me.

I extend my gratitude to my colleagues from TU Delft Dredging department: Joep Goeree, Rudy Helmons, Xiuhan Chen, Bas Nieuwboer, Dave Weij, Thijs Schouten, and Ershad Ahamed Chemmalasseri. I did enjoy the time I spent with them.

My last but not least appreciation goes who supported me and advised me to start my MSc at TU Delft, specifically Dr. Ir. Erik Mosselman, Dr. Alessandra Crosato, Rens Hasman and Lidewij de vries. Their ideas and motivation helped me to make my decision to follow my second Master of Science study at TU Delft. I am grateful that Alessandra always had time for me and whenever I needed advice.

Protogene BYISHIMO  
Delft, May 2018

# Contents

<b>1. Summary</b>	<b>i</b>
<b>2. Acknowledgments</b>	<b>ii</b>
<b>3. List of figures</b>	<b>vii</b>
<b>4. List of tables</b>	<b>xi</b>
<b>5. Abbreviations</b>	<b>xii</b>
<b>6. List of symbols</b>	<b>xiii</b>
<b>7. CHAPTER 1</b>	<b>1</b>
1.1. General background	1
1.2. Deep-sea mining	2
1.2.1. Valuable and targeted mineral deposits	2
1.2.2. Deep Sea Mining systems	3
1.2.3. Environmental aspects of deep-sea mining	4
1.3. Research outcomes and relevancy	5
1.4. Problem identification	5
1.4.1. Problem definition	5
1.4.2. Research questions	6
1.5. Objectives	7
1.6. Assumptions and limitations	7
1.7. Research methodology	8
1.8. Outline	8
<b>8. CHAPTER 2</b>	<b>10</b>
2.1. Description of a deep-sea mining plume	10
2.1.1. Classification of turbulent jets and plumes	10
2.2. Turbulence	11
2.2.1. General	11
2.2.2. Turbulent buoyant jets in a still environment	13
2.2.3. Turbulent negatively buoyant jets in a still environment	14
2.2.4. Negatively buoyant jet and plumes	15
2.2.5. Negatively buoyant jet spreading	16
2.2.6. The entrainment hypothesis	16
2.2.7. Negatively buoyant jet profile	17
2.2.8. Top-hat approximation	18
2.3. Turbidity Currents	19
2.3.1. Introduction	19
2.3.2. Sediment fall velocity in still water	20
2.3.3. Zone of boundary influence (ZBI)	21
2.3.4. Gravity Currents	22
2.3.5. Sediment transport in turbidity currents	23
2.3.6. Sediment concentration in turbidity currents	23
2.3.7. Interaction of the turbidity current with the bed	24

<b>9. CHAPTER 3</b>	<b>25</b>
3.1. Introduction	25
3.2. Experimental setup	26
3.2.1. The modular tank	26
3.2.2. The artificial seabed table	28
3.3. Sediment minerals	28
3.4. Sediment mixing tank	29
3.5. The discharge Jet pipe	30
3.6. Experiment scenarios	31
3.7. Experiments conditions	31
3.8. Measurement techniques	32
3.8.1. Flow velocity measurements	32
3.8.2. Suspended sediment concentration measurement	35
3.8.3. Jet/plume and density current Video imaging	37
3.9. Experimental method and procedure	38
<b>10. CHAPTER 4</b>	<b>41</b>
4.1. CFD model introduction	41
4.2. Model description	41
4.3. TUDflow3D governing equations	42
4.4. Plume and density current interactions with the bed	42
4.5. Modeling of turbulence in TUDflow3D	43
4.6. CFD model set-up	43
4.6.1. General setup	43
4.6.2. JETPLUME	44
4.7. LES model boundary conditions	44
4.7.1. Inflow and outflow	44
4.7.2. The free surface	45
4.7.3. Bottom solid wall	46
4.8. Discretization schemes	46
4.9. Grids construction	46
4.10. Bathymetry	47
4.11. Implemented of slope in TUDflow3D CFD model	48
<b>11. CHAPTER 5</b>	<b>49</b>
5.1. Introduction	49
5.2. Image analysis	50
This part of the work was done in corroboration with Sjoerd Warringa, an MSc student in Offshore and Dredging Engineering during his Research Exercise which is a requirement for his MSc study package.	51
5.2.1. Flow time elapse turbidity current development	51
5.2.2. Turbidity current front Position	55
5.2.3. Turbidity current front velocity	56
5.2.4. Sediment deposition ring	56
5.3. Direct local turbidity measurements	58
5.4. Foslim optical suspended sediment concentration	59
5.5. Density current velocity profile (ADV)	59
<b>12. CHAPTER 6</b>	<b>61</b>
6.1. Introduction	61

6.2.	CFD simulation results of impinging Jet under submerged condition	63
6.3.	Turbidity current flow reflection on the vertical sidewalls	63
6.4.	Turbidity current interactions with the bed	64
6.5.	Turbidity current flow velocity and SSC profiles CFD prediction	65
6.5.1.	Turbidity underwater current flow velocity profile	67
6.5.2.	Turbidity underwater current SSC profile	67
6.6.	Comparison for different initial plume conditions at the source	68
6.6.1.	Effects due to changes in initial suspended sediment concentration	68
6.6.2.	Effects due to changes in the plume release heights from the bed	69
6.6.3.	Effects of the sloping seabed topography	70
6.6.4.	Effects of a uniform ambient current on deep-sea mining plume dispersion	71
<b>13.</b>	<b>CHAPTER 7</b>	<b>74</b>
7.1.	Conclusions	74
7.2.	Recommendations	75
<b>14.</b>	<b>Appendix A. Average flow velocity and SSC profiles</b>	<b>79</b>
<b>15.</b>	<b>Appendix B. ADV flow velocity and SNR measurements</b>	<b>88</b>
<b>16.</b>	<b>Appendix C. Granulometric data and physical characteristics</b>	<b>94</b>



# List of figures

Figure 1-1. Examples of the future world green technologies with clean renewable and low-carbon energy. (Solar Pane(left) , wind turbines(middle), and electric cars(right). Source: MarineE-tech).....	1
Figure 1-2. Examples of deep-sea minerals (Massive Sulphides(left), Manganese nodules(center) and Black smoker Sulphides(right) (Source: Schriever & Thiel, 2013).....	3
Figure 1-3. Impression of a deep-sea mining system and processes involved. The proposed system for a project off the coast of Papua New Guinea, underway by early 2019(Source: Nautilus Minerals Inc.).....	3
Figure 1-4. Examples of deep-sea animals. Sea cucumber roaming on mineral-rich manganese nodules(left). Sulphide vent with tube worms (center) and sponges discovered in the Pacific Ocean where deep-sea hydrothermal vents have been discovered and on mineral-rich manganese nodules(center). Source: NIOZ. ....	4
Figure 1-5. Impression of the studied physical processes in this research. submerged dense jet impinges on a sloped bed and with erosion-deposition processes, it interacts with the bed (left). CFD simulation of a development of an impinging jet over time visualized by a passive scalar(right). van Grunsven et al., (2016). ....	6
Figure 1-6. Global distribution of known sites of discovered seafloor minerals ( Phosphorites, Massive sulfides, and Polymetallic nodules). X, MS by the squares and the polymetallic nodules by the small dots represents phosphorite fields in the figure: Source: United States Environmental Protection Agency (UAPA). ....	9
Figure 2-1 Examples of turbulent flows. (left): A high Reynolds number turbulent jet produced by the test of a rocket in the hills of Redland in California. (right): A thermal plume generated by fire in Barcelona in Feb 1994(Gamma-Imaginechina). Source: Lee and Chu (2003). ....	12
Figure 2-2 RMS concentration fluctuations of an advected line puff. vertical centerline profile(left) and horizontal profile at the level of the center of mass(right). Experimental data from Lee and Chu (2003). ....	14
Figure 2-3 Schematic of the underflow generated from a dense buoyant jet impinging on a horizontal bottom. Figure adapted from Chowdhury (2014). ....	14
Figure 2-4. Radial velocity, concentration, and top-hat profile. Bottom-right figure reproduced after Chu and Lee (2003). Figure on the right is for an experiment in this research (H=1m; SSC <sub>0</sub> =20g/l). Initial w <sub>jo</sub> =0.7m/s and the Gaussian profile are obtained at a falling distance H*=1m from the source. Photography: Ivar Pel. ....	17
Figure 2-5 Example of seabed bathymetries. Monterey submarine canyon of about 1 km wide (source: D. Smith, USGS)(Left image). 3-dimensional topographic features of of proposed mining area at Salwara1project in Papua New Guinea (Source: Nautilus Minerals Niugini)(right image).....	19
Figure 2-6 Centre slices of a turbidity current resulted from a CFD simulation with the plume released from a height H=1m containing SSC <sub>0</sub> =20g/l impinging on a sloped bed. The current front position plotted by tracking 10% of initial SSC <sub>0</sub> released from the source. ....	20
Figure 2-7 Turbidity current flow velocity and suspended sediment concentration profiles.....	23
Figure 2-8. Classification of sediment transport mode in a river (Crosato lecture notes, 2012, UNESCO-IHE). ....	23
Figure 3-1 Experimental setup. A tank full of 23 m <sup>3</sup> tap water. (Picture was taken by Ivar Pel (© NWO). ...	26
Figure 3-2. Main parts of the experimental setup: Front view of the modular tank, mixing tank and table inside the modular tank. ....	26
Figure 3-3 Experimental measurements map: Top view of the modular tank and table with Plexiglas surface with installed underwater lights.....	27
Figure 3-4 0.8 m <sup>3</sup> Mixing tank/reservoir (left) and grain size distribution (right). ....	29

Figure 3-5 Katronic KATflow 200 in operation (A), Working principle (B) and Flow hydrograph. ....	30
Figure 3-6 Different ADV component (left) and positioning of the probe during measurement (right). ....	34
Figure 3-7 Exp 00 100 20: location $P_6$ background (top), steady state (middle) and actual (bottom) measurements at elevation $z=15$ mm. ....	34
Figure 3-8. velocity time series measurement at $z=0.01$ m above a flatbed. ....	35
Figure 3-9 Turbidimeter AL450T-IR components, working principle, and a calibration curve. ....	36
Figure 3-10 Steps for Turbidimeter AL450T-IR. (a): Samling, (b): Mixing, (c): 3 vials sampling, (d): vial mixing and (e): NTU measurement. ....	36
Figure 3-11. Flow streamlines and vertical velocity profile during turbid water sampling at $P_4$ . ....	36
Figure 3-12. FOSLIM components and a calibration curve. ....	37
Figure 3-13. Darkened tank using curtains, fluorescent ink, camera and raw and its processed image. ....	38
Figure 4-1 TUDflow3D domain and buoyant jet integral model JETPLUME domain ( Exp 00 050 20). ....	43
Figure 4-2 JETPLUME simulation for TUDflow3D boundary inputs. ....	45
Figure 4-3 Used grid for simulating jet/plumes spreading and density current flows. ....	47
Figure 4-4 Used grid for simulating jet/plumes spreading and density current flows (Note that this is not the grids used during simulations done during this thesis. This is a zoomed to illustrate how a slope was implemented in TUDflow3D. The grid used is shown in Figure 4-3). ....	48
Figure 5-1 Images of the negatively buoyant jet and formed turbidity current after impingement. Flatbed (top) and 10 degrees inclined bed(Bottom. Images taken during experiment $H=0.5$ , $SSC_0=20g/l$ . ....	50
Figure 5-2 Grayscale intensity 80 contours. Processed image for Exp 00 025 20 ( $S=0$ , $H=0.25m$ , $SSC_0=20g/l$ ). ....	51
Figure 5-3 Sideview snapshots without video processing: (a) the first test and (b) during the last test. Both videos are taken during an experiment with initial $SSC=20g/l$ . ....	51
Figure 5-4 Top-view of radially spreading plume on a horizontal bed (Exp Slope=0, $H=0.25m$ , $SSC_0=20g/l$ ). ....	52
Figure 5-5 Steady states 60 seconds averaged images of each experiment plotted on a 100x100mm grid. ....	53
Figure 5-6 Snapshots at time = 10s, 30s, 50s, and 75s, images are plotted on 0.1x0.1m grid. Note that for $H=1$ , the turbidity current front is out of the camera frame. ....	54
Figure 5-7 Radial spreading turbid driven current plume at flatbed as a function of time. Note that the curves that end soon for instance for the plume released at $H=1m$ , means that the front of the turbidity current was already outside the camera frame. ....	55
Figure 5-8 Density current front velocity $u_f$ as a function of time and logarithmic fitting curve. ....	56
Figure 5-9 Sediment deposition rings formed after 30 minutes. (a) shows a side view of a semi-elliptic sedimentation ring formed during the experiment ( $H=0.5m$ , $SSC_0=20g/l$ ) impinging on a sloped bed and (c) shows its top view. (d) shows a top view of a circular sedimentation ring of the same experiment source parameters ( $H=0.5m$ , $SSC_0=20g/l$ ) but impinging on a flatbed. (b) and (e) show a side and a top view for the experiment ( $H=1m$ , $SSC_0=20g/l$ ) impinging on a sloped bed. Note that for this test there are no sediment deposition rings observed (they are plume-like impingement regime). ....	57
Figure 5-10. SSC (right) and average dilution (left) measured at the impingement point. ....	58
Figure 5-11 Direct local turbidity measurements by AL450T-IR standards NTU. ....	58
Figure 5-12 Logarithmic plots of Direct local turbidity measurements by AL450T-IR standards NTU. ....	59
Figure 6-1 CFD LES model results. Centre slices images of sediments plume spreading for the simulation $H=0.5$ m and $SSC_0=20$ g/l. On a flatbed and without ambient current(left column). Flatbed and ambient current (middle column) and sloped bed without ambient current(right column). ....	62
Figure 6-2 Instantaneous front view images of laboratory tests and CFD centre slice images. Flatbed, $SSC_0=20g/l$ , $H=1m$ (Top panel) and 10 degree slope bed, $SSC_0=20g/l$ , $H=1m$ (lower	

panel). <b>Note</b> that the laboratory images are not scaled and show front views while the CFD images are cross sections at the plume center.....	63
Figure 6-3 Three dimensional CFD results, sediment plume spreading after 6 minutes for the plume mixture release at H=1m with SSC <sub>0</sub> =20g/l. The top figure shows the spreading on a horizontal bed while the bottom figure shows a similar simulation with the same boundary conditions but falling on a 10 degree sloped bed.....	64
Figure 6-4. Two dimensional (x,y) top views of CFD resulted in horizontal velocity (top images) and cumulative sediment deposition (bottom images) at the bed after 360s. Simulation of experiment with a flatbed and three different cases of initial SSC <sub>0</sub> =20g/l SSC <sub>0</sub> =10g/l and SSC <sub>0</sub> =5g/l all released from H=1m. <b>Note</b> that the color-bar have different scales. The size of the deposition ring and color-bar scale decrease from left to right. ....	64
Figure 6-5 y-axis centre slice at x=0 of LES results. Predicted horizontal velocity and SSC ( Run 00 100 20).....	65
Figure 6-6 Typical (top row) velocity and (bottom row) suspended sediment concentration profiles of turbidity current flow generated by impinging plumes. ....	66
Figure 6-7. ADV Signal-to-Noise Ratio during the flow velocity measurements. The calibration measurement was done before the plume release and followed with steady-state measurement. After a steady state, the velocity profile is measured by a single point from z=60mm). This figure is produced for Experiment S=10°, H=0.25m and SSC <sub>0</sub> =20g/l. ...	66
<i>Figure 6-8 Comparison of the velocity and SSC profiles for turbidity current generated by plumes released at the same height (H=1m) but containing different initial SSC (20 g/l, 10g/l, and 5g/l). Exp. on a horizontal bed.....</i>	<i>68</i>
<i>Figure 6-9 Comparison of the velocity and SSC profiles for turbidity current generated by plumes released at the same height (H=1m) but containing different initial SSC (20 g/l and 5g/l). Impingement on 10o sloped bed.....</i>	<i>68</i>
Figure 6-10 Comparison of the velocity and SSC profiles for turbidity current generated by a source of plumes with similar SSC <sub>0</sub> = 20g/l but released at different height H = 1m, 0.5m and 0.25m from an a flatbed.....	69
Figure 6-11. Comparison of the velocity and SSC profiles for turbidity current generated by a source of plumes with similar SSC <sub>0</sub> = 20g/l but released at different height H = 1m, 0.5m and 0.25m from a 10 degrees sloping bed.....	70
Figure 6-12 Effects of 10 degrees sloping bed during the experiment: H=0.5m, SSC=20g/l compared to results with a flat table.....	71
Figure 6-13 Effects of 10 degrees sloping bed. Experiment with H=0.5.m, SSC=5g/l compared to results with a flat table.....	71
Figure 6-14 Effects of uniform current (uc=0.014m/s ). Experiment/Run Flatbed H=0.5m and SSC <sub>0</sub> =20 g/l.....	72
Figure 6-15 Two dimensional (x,y) top views of CFD resulted horizontal velocity and and cumulative sediment deposition at the bed after 360s. Simulation of experiment with a flatbed, H=0.5m, SSC <sub>0</sub> =20g/l and uniform ambient current u <sub>c</sub> =0.014m/s. ....	72
Figure 6-16 LES simulation results in comparison to different input parameters. Center slices images of 360s plumes spreading (H=0.5 m and SSC <sub>0</sub> =20 g/l). Flatbed without ambient current(top), flatbed and ambient current (middle) and 10° sloped bed without ambient current(bottom). It is reminded to the reader that the effects of ambient current were not included in the laboratory experiments.....	73
Figure 0-1 Average and SSC profiles for experimrnt serie A (Flatbed, slope=0°).....	82
Figure 0-2 Average and SSC profiles for experimrnt serie B (slope=10°).....	87
Figure B-0-1 Average signal-to-noise ratio profiles measured at x=0.1m, x=1m, and 3m for Experiment S=10 degrees, H=0.25m and SSC <sub>0</sub> =20g/l.....	88
Figure B-0-2. Steady state measurement at z=0.015m to check the steady state of the plume spreading before the start of the flow velocity and SSC profile.....	89

Figure B-0-3 Calibration measurement at $z=0.015\text{m}$ to check the background flow velocity and SSC. ....	89
Figure B 0-4. Flow velocity and SNR time series measured at the distance $x$ from the impingement point at elevation $z=0.060\text{m}$ .....	90
Figure B 0-5. Flow velocity and SNR time series measured at the distance $x$ from the impingement point at elevation $z=0.050\text{m}$ .....	90
Figure B 0-6. Flow velocity and SNR time series measured at the distance $x$ from the impingement point at elevation $z=0.040\text{m}$ .....	91
Figure B 0-7. Flow velocity and SNR time series measured at the distance $x$ from the impingement point at elevation $z=0.035\text{m}$ .....	91
FigureB 0-8. Flow velocity and SNR time series measured at the distance $x$ from the impingement point at elevation $z=0.015\text{m}$ .....	92
Figure B 0-9. Flow velocity and SNR time series measured at the distance $x$ from the impingement point at elevation $z=0.010\text{m}$ .....	92
Figure B 0-10. Flow velocity and SNR time series measured at the distance $x$ from the impingement point at elevation $z=0.005\text{m}$ .....	93
Figure B 0-11. Flow velocity and SNR time series measured at the distance $x$ from the impingement point at elevation $z=0.003\text{m}$ .....	93

# List of tables

Table 2-1 Expected turbulent flow in Deep-sea Mining Operations.....10

Table 2-2 Near-field zones of downward buoyant plumes and impingement .....15

Table 3-1. Experiment Froude scaling (1:50).....28

Table 3-2 Experiments scenarios.....31

Table 3-3 Experiments characteristics, parameter, and conditions.....31

Table 3-4 Measurement coordinates and locations from the impingement point (IP) .....33

Table 4-1 LES model input parameters .....44

# Abbreviations

2D	two-dimensional
3D	three-dimensional
ADV	Acoustic Doppler Velocimeter
CDS2	Second-order central difference scheme
DNS	direct numerical simulation
DSM	Deep-Sea Mining
IMARES	Institute for Marine Resources & Ecosystem Studies
IP	Impingement point
NIOZ	Netherlands Institute for Sea Research
NTU	Nephelometric turbidity unit
PDC	Particle distribution curve
SNR	Signal-to-noise ratio
SSC	Suspended sediment concentration
SSC <sub>0</sub>	Initial suspended sediments concentrations
SWOE	sediment waste and other effluents
TNO	Netherlands Organisation for Applied Scientific Research
TU Delft	Technical University of Delft
UK	United Kingdom
WUR	Wageningen University & Research
WALE	wall adapting local eddy viscosity sub-grid scale model

# List of symbols

## Roman symbols

Symbols	Description	units
$b$	plume half-width	[m]
$B$	width, jet/plume buoyancy flux/ specific buoyancy flux	[m][m <sup>4</sup> /s <sup>3</sup> ][m <sup>4</sup> /s <sup>3</sup> ]
$B_{j0}$	initial buoyancy flux buoyant jet	[m <sup>4</sup> /s <sup>3</sup> ]
$C$	concentration	[% v]
$C_l$	volume concentration of fraction l	[% v]
$C_{max}$	maximum jet volume concentration	[% v]
$D_j$	jet diameter	[m]
$D_{10}$	10 <sup>th</sup> percentile sediment particle diameter	[m]
$D_{50}$	50 <sup>th</sup> percentile sediment particle diameter	[m]
$D_{90}$	90 <sup>th</sup> percentile sediment particle diameter	[m]
dB	Decibel	[dB]
$D_{epI}$	deposition flux of fraction l	[kg/s/m <sup>2</sup> ]
$E_{roI}$	erosion flux of fraction	[kg/s/m <sup>2</sup> ]
$f$	frequency	[1/s]
$H$	sediment waste release height	[m]
$H$	Plume release elevation from the bed	[m]
$H^*$	JETPLUME output elevation	[-]
Ga,Cd,Ge,Ir,As	Gallium, Cadmium, Germanium, Iridium, Arsenic	m]
$L_{b,plume}$	jet/plume transition scale	[m]
$L_M$	momentum length scale	[m]
$L_Q$	source length scale	[m]
$L_s$	momentum length scale	[m]
$M$	momentum flux/ specific momentum flux	[m <sup>3</sup> /s <sup>2</sup> ]
$F_{re}$	densimetric Froude number	[-]
$P$	pressure	[N/m <sup>2</sup> ]
$Q$	volume flux, specific volume flux	[m <sup>3</sup> /s]
$Q_{j0}$	initial volume flux	[m <sup>3</sup> /s]
$R$	radius	[m]
$r_j/r_i$	turbidity current spreading radius	[-]
$R_e$	Reynolds number	[-]
$S$	dilution, salinity	[-]
$SSC$	suspended sediment concentration	[kg/m <sup>3</sup> ]
$SSC_0$	Initial suspended sediment concentration	[kg/m <sup>3</sup> ]
$St$	Strouhal number	[-]
$T/t$	Time	[s]
$u_c$	ambient current velocity Entrainment velocity	[m/s]
$u_e$	entrainment velocity	[m/s]
$u,v,w$	velocity components	[m/s]
$u', v', w'$	velocity fluctuation	[m/s]
$U_f$	front velocity	[m/s]
$w_j$	jet velocity	[m/s]
$w_{j0}$	Initial jet velocity	[m/s]
$w$	velocity of top-hat profile	[m/s]
$V$	volume	[m <sup>3</sup> ]
$x,y,z$	Cartesian co-ordinate	[-]

$z^*$	CFD model input elevation	[m]
$z$	distance from the bed	[m]

### Greek symbols

$\Gamma$	discharge source parameter,	[-]
$\alpha$	entrainment coefficient/Bed slope	[-]/[degree]
$\beta$	spreading rate	[-]
$S_{ct}$	turbulent Schmidt number	[-]
$\Delta x$	grid size in $x$ direction	[m]
$\Delta y$	grid size in $y$ direction	[m]
$\Delta z$	grid size in $z$ direction	[m]
$\Delta z^+$	grid size in $z$ direction in wall units	[-]
$\nu$	viscosity	[m <sup>2</sup> /s]
$\nu_e$	eddy viscosity	[m <sup>2</sup> /s]
$\nu_{mol}$	molecular viscosity	[m <sup>2</sup> /s]
$\rho$	density	[kg/m <sup>3</sup> ]
$\rho_c$	density carrier fluid	[kg/m <sup>3</sup> ]
$\rho_l$	density of fraction $l$	[kg/m <sup>3</sup> ]
$\rho_s$	sediment density	[kg/m <sup>3</sup> ]
$\rho_{mix}$	mixture density	[kg/m <sup>3</sup> ]
$\rho_w$	water density	[kg/m <sup>3</sup> ]
$\tau$	shear stress	[N/m <sup>2</sup> ]

### Subscript/Superscripts

$a$	Ambient
$m$	centerline
$e$	excess, entrainment,
$c$	current

# CHAPTER 1

## Introduction

---

The first chapter describes the Deep-Sea Mining (DSM) operation and background of the potential environmental impacts due to dense plumes created by the mining activities. The research questions and the goals of the work that has been carried out are detailed in this chapter. Furthermore, the writer provides a short description of the research concept design and context used to answer the research questions.

### 1.1. General background

For many decades, humans have been exploiting marine natural resources to meet economic needs. Since then, the deep and large seas have become interesting for the international, national and private corporates (Browning, 1968). Since World War II, the consumption of most raw materials has increased steadily. The demands are expected to continue to grow in response to the burgeoning global population and economic growth (Krausmann et al., 2009). In the recent years, new technologies such as examples in Figure 1-1, the use of solar panels, wind turbines, and electric cars give promises of a future world of green technologies with clean and renewable energy at low-carbon emissions. Furthermore, modern machines and tools, communication technology, computers and global energy production require considerable quantities of raw materials such as copper, manganese, cobalt, silver, gold, zinc, etc. In recent years, emerging economies especially the BRIC (Brazil, Russia, India, and China), proclaimed to be using greater varieties of metals than they ever used before (Wu et al., 2017). This means that the global demands of raw minerals are high and are expected to increase in the near future. In the light of these trends, there is an increasing global concern over the long-term availability of secured and adequate supplies of the minerals and metals needed by society. The modern world is enthusiastic about the importance and essential contribution of developments towards green technologies, yet these have a high risk of a supply shortage of raw materials.



Figure 1-1. Examples of the future world green technologies with clean renewable and low-carbon energy. (Solar Pane(left), wind turbines(middle), and electric cars(right). Source: MarineE-tech).

In the 1960s, the prospect of mining minerals under the deep-sea was brought up and considered as great opportunities for minerals exploitations. However, the first attempt to exploit deep-sea manganese nodules ended in failure as a result of the collapse of global metal prices (Glasby, 2000). Over the past few years, the market seems to have changed due to the increase in demand. DSM is considered to be a possible alternative to produce raw materials which are running out on land (Schriever & Thiel, 2013). Targeted minerals contain silver, gold, copper, cobalt, and zinc. It is expected that the first DSM project in national waters may begin in 2018 into the coast of Papua New Guinea (Petersen, 2014). The deep-sea mining industry has the technology in place and mining systems have been proposed, built and tested (Welling, 1981). However, there are still major technological and environmental challenges as the locations where mining activities will take place are environmentally sensitive and little is still known about the ecosystem in these areas. Some deposits are found in areas that are known to have high ecological values. Sometimes they are found in the oceans or seas with no historical background, and even without any nearby shoreline developments. As a consequence, the environmental impacts of deep-sea mining are considered to be uncertain especially because little is known about deep-sea organisms. The deep-sea organisms' distributions are barely known and expected to be very sensitive to disturbance (Corliss, 1985). There is still a lack of knowledge to predict impacts to the ecosystem components as negative effects caused by the extraction of minerals from the seabed. The biggest concern of scientists is the possibility that DSM activities could cause the unique benthic communities to become extinct. There is a high chance of significant impacts on mobile marine species such as fishes, mammals, and reptiles due to the increase in suspended sediment concentration in plumes containing contaminants that will eventually deposit on the seabed.

The International Seabed Authority (ISA) is an international organization based in Kingston, Jamaica. ISA is commissioned by the United Nations to regulate DSM in international waters. Before the start of the exploitation of offshore minerals, it is a critical and obligatory task for the ISA to first understand the deep-sea environment and possible impacts. Thereafter, standards, regulations, and laws will be produced to be applied in the seabed mining industry. Over the years, there has been a lot of progress towards the development of exploitation regulations for the DSM industry. A framework for governing activities, regulations, monitoring and extraction methods has been proposed (Halfar, 2007). Yet, still more research is required to accurately predict the potential environmental effects and mitigation options which are crucial and have to be developed before DSM becomes into practice (Durdan, 2017). There is mainly a research gap in the technological development towards the reduction of the environmental impacts. This research aims to improve existing mitigation techniques, by improving our knowledge regarding the return discharge of sediment waste and other effluents (SWOE) and its interaction with the seabed.

## **1.2. Deep-sea mining**

### **1.2.1. Valuable and targeted mineral deposits**

In the guardian of March 2013, the Former British Prime Minister David Cameron stated that DSM could be worth 40bn pounds just for the UK in the period of the following 30 years (the Guardian, March 2013). Since then, deep-sea mining is already considered relevant on the economic scale. Deposits found in the deep-sea contain a range of different minerals that occur by nature in three main types. Each is associated with a distinct geology and ecosystem. Some examples of seafloor mineral deposits are depicted in Figure 1-2 and their global distribution can be observed in Figure 1-6. The three main types of deposits are:

- Seafloor Massive Sulphides (SMS) located in 1,400 – 3,700 m deep; rich in copper, lead, and zinc. They sometimes contain some gold and silver.

- Polymetallic Nodules which are rich in Nickel, copper, cobalt, and manganese. They are found in 4,000 – 6,000 m water depth.
- Manganese crusts which are found in the relatively shallower water of about 800 to 2,400 m. They contain mainly cobalt, some vanadium, molybdenum, and platinum.

Other deposits found in the deep-sea and oceans which are considered for extraction include phosphate deposits and metalliferous muds enriched in Rare Earth Elements (REEs) such as Cd, Ga, Ge, In, As, among others. Some countries have mineral reserves in their national waters while other nations (for instance the EU including the UK) with fewer mineral resources have been increasingly depending on imports of raw materials, with 49 % of raw materials being resourced from China and a dominant import of cobalt from the Democratic Republic of Congo (Goldstein, 2006). In this respect, the focus of the EU is mining into international waters.



Figure 1-2. Examples of deep-sea minerals (Massive Sulphides(left), Manganese nodules(center) and Black smoker Sulphides(right) (Source: Schriever & Thiel, 2013).

### 1.2.2. Deep Sea Mining systems

Currently, there already exist technologically feasible mining proposals. The development of mining systems varies depending on the type of mineral deposits to be mined and water depth they are found in. A typical offshore mining system as depicted in Figure 1-3 and consists of the following 3 main parts:

1. The seafloor production tools,
2. A riser and lifting system and
3. A surface support vessel

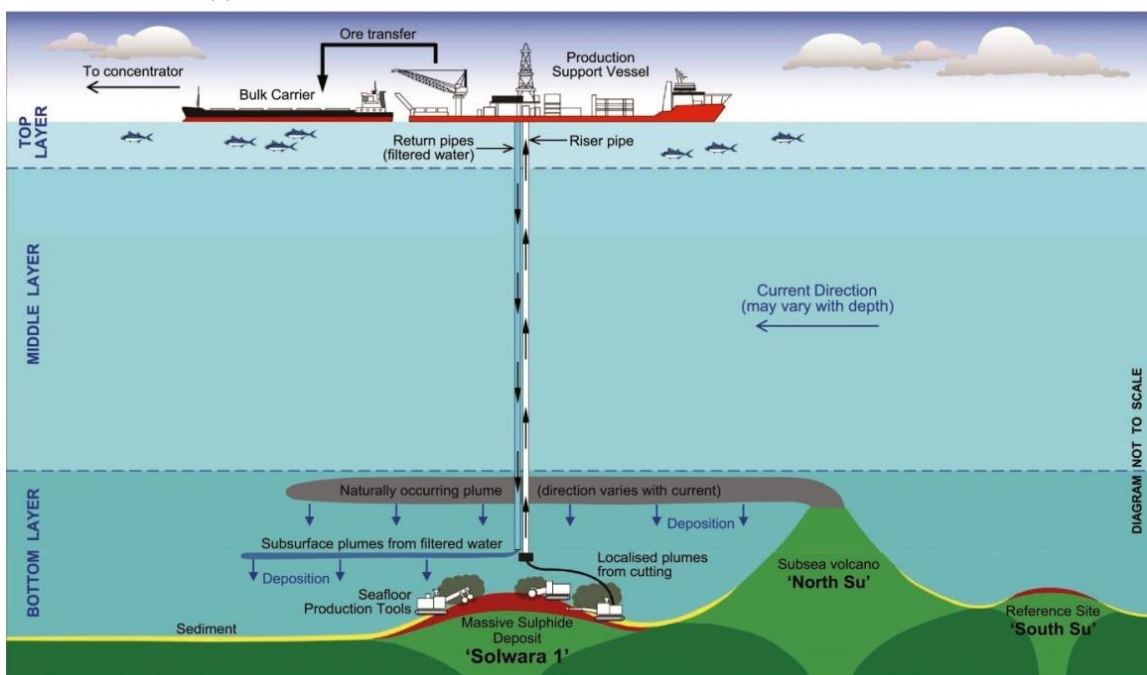


Figure 1-3. Impression of a deep-sea mining system and processes involved. The proposed system for a project off the coast of Papua New Guinea, underway by early 2019 (Source: Nautilus Minerals Inc.).

As impressively shown in Figure 1-3, the seafloor production tools use hydraulic pumps or buckets to cut and collect crusts, sulphides or nodules. A mixture of ore and water will be transported vertically via the riser (vertical pipes) up to the support vessel at the sea surface. Once the mixture is in the support vessel, water is removed from the ore. The ore can be transported to a processing facility on land. The wastewater can be released into the water column at a certain water depth or pumped back down to the site of ore collection. The latter option is considered to be the most environmentally friendly. In the report of The ISA of the year 1999 and the year 2002, it was confirmed that deep disposal of tailings is the only solution for the best environmental practice to avoid or minimize the impacts (Wood, 1999). However, the return flow will create turbidity plumes hence are proposed to be discharged preferably close to the seafloor in order to minimize the impact on the ecosystem. The return wastewater to the sea contains very fine sediment and potentially metallic particles; hence are a danger to the ecosystems.

### 1.2.3. Environmental aspects of deep-sea mining

The deep-sea environment is sensitive and contains large ecosystem components (Locket, 1977). There are concerns about long-lasting or even permanent damage to the deep-sea ecosystem which could be inflicted by mining activities. The activities might create various pressures on the wide variety of ecosystem components. These pressures will cause effects of which the intensity is depending on the ecosystem sensitivity and the pressure intensities. Expectations are that the amount of food for flora and fauna such as fish and other marine animals like examples in Figure 1-4 will decrease. This could lead to a modification of the food chain for these species, thereby reducing the number of species that live there.



Figure 1-4. Examples of deep-sea animals. Sea cucumber roaming on mineral-rich manganese nodules(left). Sulphide vent with tube worms (center) and sponges discovered in the Pacific Ocean where deep-sea hydrothermal vents have been discovered and on mineral-rich manganese nodules(center). Source: NIOZ.

TU Delft and its Partners: IMARES, NIOZ, TNO, Royal Boskalis Westminster NV and IHC Merwede; in their collaborative project “Towards Zero Impact of Deep Sea Mining Projects (TZI)”, which was a project aiming to provide an assessment framework for future environmental studies of deep-sea, has developed the basic relations between mining activities, pressures, and the marine ecosystem. The outcomes of the research proclaimed that the most relevant pressures and expected effects anticipated due to mining activities are as follow:

- Abrasion of the sea floor due to movement of the Seafloor Mining Tool (SMT) or if the end of the tailings discharge pipe lies on the seabed and is moved by the currents.
- There will be barriers to species movement due to the excavation of the mining pit itself as well as due to sediment wastes disposal.
- Deepest parts of most world oceans and seas have a background level of suspended sediments in the order of 1-10 mg/l. Due to spills of the mining tool and the return discharged sediments plumes, there will be changes in siltation enhancing the levels of suspended matters. Although there is still lack of knowledge on ecosystem responses, due to the increased suspended sediments level, the light intensity will reduce in the upper layers of the seawater column which in response will negatively affecting animals that need light for survival.

- Return plumes will contain a high level of metal contents which might cause the pH changes influencing marine animals and organisms.
- Excavation work itself and the deposition of small particles returned as waste will cause smothering of the seafloor. Some groups of animals such as the Benthic and Octocoral groups are sensitive to the high level of smothering and hence they will be negatively affected.
- Sea mammal and other groups of fishes exposed to risks as they are sensitive to loud or high-frequency underwater sound.

### **1.3. Research outcomes and relevancy**

Based on the environmental aspect of DSM already discussed above; DSM is a challenging activity which needs careful consideration and impacts mitigation measures. An appropriate environmental impact assessment must be carried out before the start of mining activities. Until today, it is still difficult to quantify the impacts and trustable mitigation methods are still questionable. Hence offshore mining technology is not yet considered a proven technology and no company managed to obtain an environmental license for mining in international waters.

Work done in this research as an MSc thesis focussed on laboratory experiments and Computational Fluid Dynamics (CFD) simulations involved the analysis of interactions of the plume with the ambient clear water and its behavior after the impact at the bed. The research focused on capturing the behavior of negatively buoyant sediment plumes released in an ambient water column.

The outcomes of the research provide a unique set of validation data for numerical models and a Large Eddy Simulation CFD model was successfully tested and approved for its capability to accurately predict the near-field spreading of DSM plumes. Additional findings from this research contribute to a better understanding of the near-field dispersion of turbidity plumes and effects of co-flow currents, and their interactions between the seafloor topography. Results from experiments will specifically be used to validate a CFD code that is still under development in OpenFOAM by Ir. F. van Grunsven, currently a Ph.D. researcher at the TU Delft. This wider research project is responsible for “Modelling offshore mining turbidity plume sources”. The project is part of the TREASURE research programme, developing knowledge and technology towards a responsible offshore mining industry. The research is in cooperation with several engineering companies, research institutes and universities: Royal Boskalis, Royal IHC, Van Oord, TNO, NWO, Wageningen University/IMARES and the TU Delft.

### **1.4. Problem identification**

#### **1.4.1. Problem definition**

Environmental advocacy groups such as Greenpeace and the Deep- Sea Mining Campaign, have argued that seabed mining should not be permitted in most of the world's oceans because of its potential to damage the deep-sea ecosystems and the possible pollution by heavy metal-laden plumes (Rosenbaum, 2011). For environmental impacts prediction, it is hence vital to accurately and reliably determine the mixing rate, pathway, and erosion of the seabed by these plumes. However, there is still little known about the impingement of particle-laden plumes on the seafloor under deep water conditions. Besides possible erosion caused by these plumes, in sloped sections of the seabed, there is a risk of initiating avalanches due to turbidity currents. To prevent unwanted scenarios to happen, the ISA wants to improve existing regulations from 1994 and ensure that the future development of seabed minerals extraction will

not cause serious and permanent damage to the marine environment. To support the decision making during the licensing process, accurate numerical predictions of the environmental impact are needed (van Grunsven et al., 2016b).

Numerical simulations of impinging jets have been done in the past (Papanicolaou and List (1988), Cooper and Hunt (2007), Van Den Bremer and Hunt (2010), van Grunsven et al. (2016a)). Authors considered the development of an impinging (dense) jet over time by a passive scalar, however without effects of settling particles in their research. As shown in Figure 1-5(right image) from the numerical simulations by van Grunsven et al. (2016a), the plume is expected to be steered in different directions, unless the flow is affected by topographic features or slopes defining the local seabed. After the plume or jet spreads on the seafloor, it may re-suspend sediments by erosion from the seafloor. As illustrated in Figure 1-5 (left image), if the seafloor below the discharge orifice is sloped, the dense plume will follow the slope in a downward direction as a turbidity current with high a probability to increase in weight and velocity. If the erosion is larger than the deposition, the turbidity current can become unstable due to a continuous increase in its weight and accelerate behaving as an avalanche. Although these models gave meaningful results and insights, they are based on rough assumptions and hence they need to be enhanced and validated with experiments and field measurements.

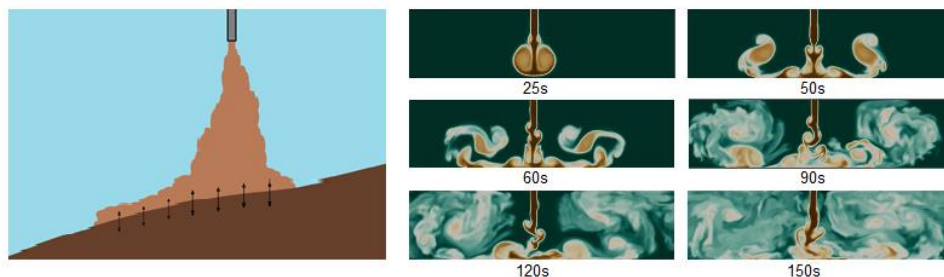


Figure 1-5. Impression of the studied physical processes in this research. submerged dense jet impinges on a sloped bed and with erosion-deposition processes, it interacts with the bed (left). CFD simulation of a development of an impinging jet over time visualized by a passive scalar(right). van Grunsven et al., (2016).

#### 1.4.2. Research questions

The main research question that evolves out of the problem definition in section 1.4.1 is:

**“Is it possible to study and measure the near-field behaviour of submerged negatively buoyant particle-laden impinging jets in a scaled laboratory environment? If so, can they be accurately simulated with a 3D CFD LES model?”**

To answer this question, sub-questions need to be answered:

- What are the flow characteristics of the released plume before impingement?
- What are the types of impingement regimes?
- After impingement of the plumes on the seafloor, what is the plume-mixing rate with the ambient clear water?
- What are the pathways of the plumes after it hits the seabed (flat or inclined)?
- What are the effects of changing the plume release height relative to the seabed?
- What are the effects due to changes in initial suspended sediment concentration at the source?
- What are the effects of a steady ambient water current?
- What are the erosion and deposition interactions by these plumes at the seabed?
- Can a CFD drift-flux model with an LES-turbulence model predict the spreading behaviour of DSM plumes in the near-field region?
- Is it required to include seabed morphological changes in the modelling process?

## 1.5. Objectives

The aim of this research is to provide on a laboratory scale, a validation data set for numerical models predicting the turbidity current flow velocity and suspended sediment concentration in the near field deep-sea mining area. In this research, an area of a 125m radius of around the impingement point is considered. Two seabed slopes were considered, a horizontal and  $10^\circ$  sloped bed. In addition, the researcher had an additional objective to simulate the experiments with a three-dimensional CFD numerical model.

In order to produce an accurate numerical model, experimental scale tests were designed to validate the model. Tasks in this research included creating negatively buoyant plumes in the laboratory and measure their flow velocities along the pathways and the amount of local suspended sediment concentration in the water column downstream of the disposal point. The focus of the research lies in observing the processes happening after the impingement of turbulent plumes on the seabed, which entails the spreading rates and pathways of the density current created after the plume hits the seabed. The most significant deliverable from laboratory tests is the data set resulting from the measurements, to be used to compare and validate CFD models which can be used as tools for plume impact prediction, and finally, produce acceptance criteria for responsible deep-sea mining practices. As there is still no standardised or 'best practice' sensing technology in order to measure turbidity plumes close to a boundary in a laboratory environment; these experiments will further explore experimental methods depending on the choice in sensing technology for this application. Hence, the gained knowledge and experience can add value to future experiments.

## 1.6. Assumptions and limitations

In order to keep the experiments within the time and financial budget, several simplifications are required with regard to the expected field scenarios. Considerations and arguments for the required simplifications are based on the choices between cost and deliverable experimental data. The same assumptions were made in the CFD model except for an implementation of an ambient current flow in one of the CFD simulation. Also, the  $D_{50}$  of the laboratory sediment was used in the model. The main simplifications are:

1. The discharged flow rate at the plume release source was assumed to be constant over time, which will not always be the case during mining operations in the field.
2. The water temperature deeper into the seas is approximately  $4^\circ\text{C}$ . The high salinity is around 35 ppt and the ambient currents can value between 0-0.3 m/s. In this research, mixtures of quartz powder with tap water without salt were created in a mixing tank and discharged into a tank filled with still and clear water from the tap. Hence, the effects of salt and ambient current present in seawater are not included in this research.
3. The seabed consists of materials of particles of different type and sizes. However, for simplicity reasons, during tests, one type of sand is chosen with particle sizes ranging from 20-63  $\mu\text{m}$  with a median  $d_{50} = 36 \mu\text{m}$  (see Figure 3-4). Also, the seabed was represented with a clean artificial table (Figure 3-1) without pre-existing seabed sediment. This means that roughness features present in the deep ocean floor are simplified.

## 1.7. Research methodology

In correspondence to the research question in section 1.4.2, the research methodology is characterized by two methods:

1. Laboratory experiments
2. CFD simulations

Experiments were carried out in the Dredging laboratory of the TU Delft, while the CFD computations were done at a computer cluster of Svašek Hydraulics based in Rotterdam. As explained in the previous section, the aim of this research was to experimentally investigate the processes of underflow generated after the impinging of dense buoyant plumes on the seafloor. The experimental procedure was to discharge a sediment mixture at a constant volume flow rate through a submerged vertical pipe into a body of water. The plume flows downwards onto an artificial seabed represented by a table as shown in Figure 3-1.

Both experiments and CFD simulations involved a wide range of the following initial setups:

- Steady flow rate out of the discharge pipe at a rate of 3.3l/min equals the flow velocity of 0.707 m/s for a pipe diameter  $D=10\text{mm}$ .
- Three different discharge elevations relative to the bed.  $H = 1\text{m}$ ,  $H = 0.5\text{m}$ , and  $H = 0.25\text{m}$ .
- Three different initial SSC in the discharged plume were considered: 20g/l, 10g/l, 5g/l.
- Variable bed slopes. A flatbed and an inclined bed with an angle of 10 degrees (Tests not reported in this document).

## 1.8. Outline

The two main components of this thesis are the development of laboratory experiments and numerical simulations studies on DSM sediment waste disposal. These two methodologies are strongly related because the same conditions as in the laboratory were produced in the CFD model. The theory of the near-field plume dispersion, entrainment, mixing and underwater density current is used to interpret experimental data. These topics are extensively covered in the following chapter. The goals, setup, and procedure of the laboratory experiments are discussed in CHAPTER 3. Detailed information about the governing equations, numerical schemes and the boundary conditions of the CFD code used to simulate the laboratory tests are described in CHAPTER 4. Results obtained from both experiments and CFD simulations and their comparisons, as well as the detailed discussions, are found in CHAPTER 5 and 6 respectively. Finally, the conclusions and recommendations for mitigating the environmental impacts caused by the DSM return plumes are given in CHAPTER 7.

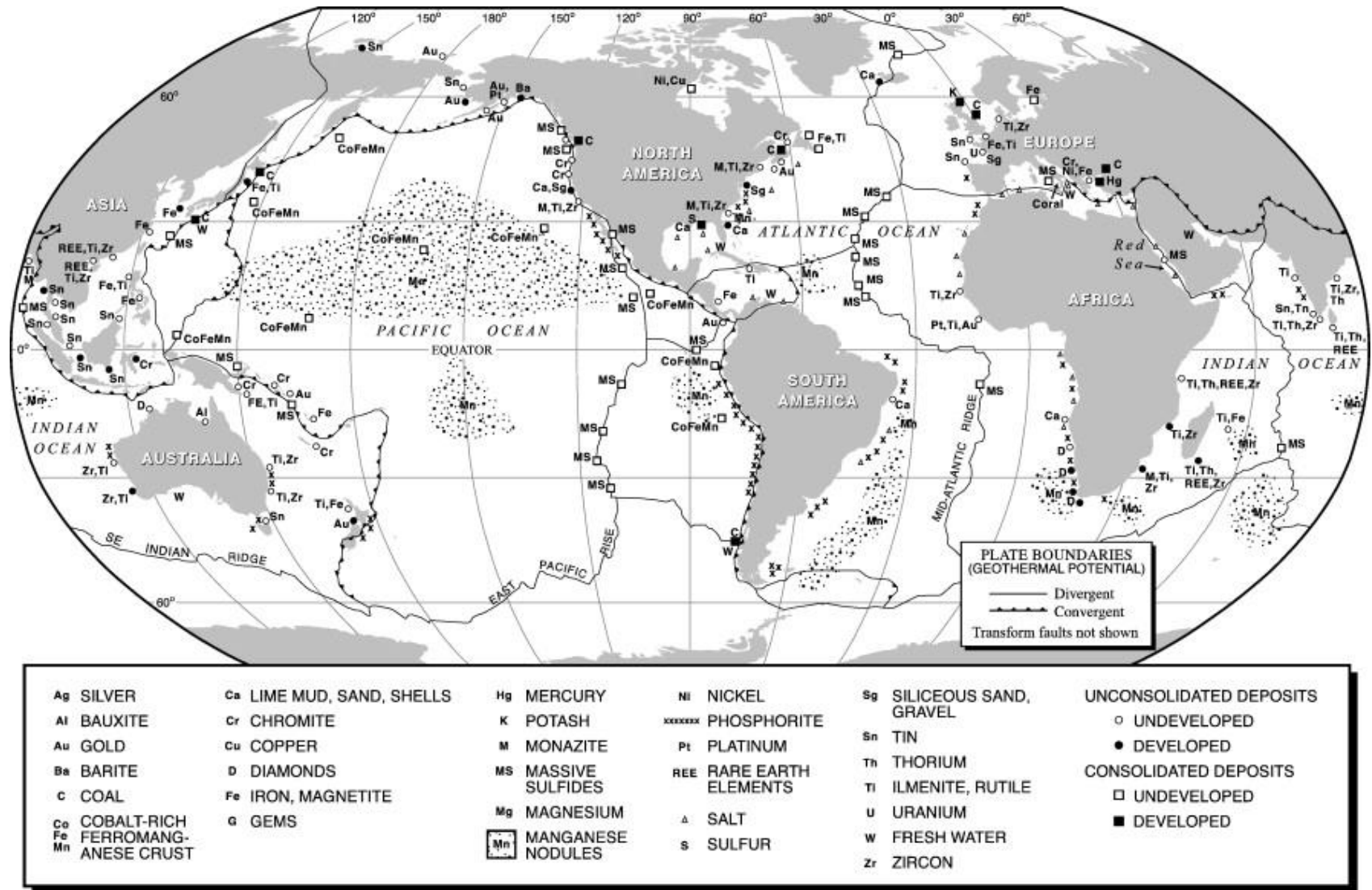


Figure 1-6. Global distribution of known sites of discovered seafloor minerals ( Phosphorites, Massive sulfides, and Polymetallic nodules). X, MS by the squares and the polymetallic nodules by the small dots represents phosphorite fields in the figure: Source: United States Environmental Protection Agency (UAPA).

# CHAPTER 2

## Literature study on deep-sea mining plume dispersion and turbidity current flows in the near-field region

---

This chapter contains the background knowledge required to understand the used research methodology, the analysis of the results obtained from the laboratory experiments and CFD simulations. Within this chapter, the state of knowledge, including existing theory and studies related to the two methodologies, is discussed.

### 2.1. Description of a deep-sea mining plume

#### 2.1.1. Classification of turbulent jets and plumes

The literature describes the deep-sea mining plume as ‘submerged tailings disposal in a form of jets or plumes’ (Schriever, 2013). In most cases, the discharged fluids will be denser than the ambient seawater, hence they can be referred to as jets or plumes with negative buoyancy, or negative buoyant jets or plumes. In contrast, a pure jet is defined as a continuous discharge of only momentum and neutral buoyancy. When the mixtures are discharged as a continuous source of only buoyancy, they are called pure plumes. A pure plume can consist of a mixture of dissolved matter like salt, or even due to a difference in temperature. Examples in Figure 2-1 show: The left, a high Reynolds number turbulent jet produced by the test of a rocket in the hills of Redland in California, where the right image shows plumes created by the continuous source of buoyancy during the fire event at a theatre in Barcelona on February 1994.

However, in this study, the extra buoyancy is due to suspended solids in the fluid mixture. The appearance and water quality of the return discharge from dDSMoperations are much affected by the presence of high contents of clay, silt, and very fine sand content. For that reason, they are also called “Turbidity Plumes”. During an entire mining operation, there will be multiple sources of turbidity plumes.

Table 2-1 Expected turbulent flow in Deep-sea Mining Operations

Flows	Continuous source	Intermittent source
Momentum only	Jet	Puff
Buoyancy only	Plume	Thermal
Momentum + Buoyancy	Buoyant Jet	Buoyant Puff

Primary production of turbidity plumes will be directly due to mining operations and the return of tailings discharged, preferably near the seabed, after minerals separation. Secondary plumes will be produced indirectly by resuspension of previously deposited material, formed by erosion in areas of high-velocity. Examples of types of expected turbulent plumes in deep-sea mining operations are reported in Table 2-1,

adapted from Lee and Chu (2003). In this research, the focus is limited to the turbidity plume, created by the return flow of tailings as it is discharged via a vertical round pipe.

Fernando (2013) classified turbidity plumes dispersion into three major regimes. This classification is based on the source conditions at the pipe outlet, in comparison with the local conditions at a certain distance from the disposal location. In an open sea, the three zones are:

- **The Near-Field Zone (NFZ):** Close to the source outflow. According to the discharge conditions, this zone is defined as a zone where mixing is dominated by the initial discharge velocity, and/or density differences. On a field scale, the NFZ ends within some hundreds of meters from the source location.
- **The Far-field Zone (FFZ):** Farther outside the NFZ, the plume evolution is mainly governed by the settling of solids or in combination with the environmental conditions such as the ambient seawater currents or Coriolis effects. On a field scale, the FFZ can cover several kilometers around the disposal location. The plumes dispersion time scale can be hours or days.
- **Intermediate Zone (IZ):** Typically, after a few hours of mixing from the source, the flow is between the NFZ and FFZ. Within the Intermediate Zone (IZ) there still is the influence of density differences, but ambient currents or even Coriolis might become relevant. On the field scale, this zone covers a few hundreds of meters or even kilometers in the presence of currents.

The focus of this study is DSM plumes mixing inside the Near-Field Zone. This was chosen based on the limited size of the experimental facilities, as well as the fact that the NFZ determines the amount and distribution of suspended sediment used for the FFZ calculations as an input.

As introduced earlier, DSM tailings will be released as a plume with both an initial momentum and buoyancy flux; hence, the plumes are classified as buoyant jets. For that reason, the focus of this chapter is limited to the continuous source of both buoyancy and momentum. For readers who are interested in detailed topics related to jets and plumes, it is recommended to look in the book "TURBULENT JETS AND PLUMES- a LAGRANGIAN APPROACH" written by Lee and Chu (2003). In their book, authors base detailed descriptions of not only pure jets and plumes but also other flow types such as plane jets, round puffs, round line thermal among others on the size and shapes of the orifice and initial discharge conditions. The book also contains empirical and semi-empirical formulas to estimate the source strength, dimensions, and the volume fluxes at any local point along the path of the plume.

In the present work, attention is made mainly on similar types buoyant jet and plume depicted in Figure 2-1 from available literature. These types of turbulent flows are the most expected type of turbulent flows to be present during DSM tailings disposal. Note that the flow shown in Figure 2-1 are positively buoyant flows in air while. This research will focus on negatively buoyant turbulent flow under water. As the study in this research concerns turbulent flows, this phenomenon is first treated in the following section.

## 2.2. Turbulence

### 2.2.1. General

The majority of the flows encountered in nature are turbulent. More examples of turbulent flows, apart from the ones shown in Figure 2-1, turbulent flows are also observed at the boundary layer of the earth's

atmosphere, the flows in rivers and channels, oil and gas in pipelines, among others. Generally, laminar flows can be considered as the exceptions in fluid mechanics. To ensure that forces are correctly scaled in experiments (with turbulence) and that there is dynamic similarity; the Reynolds number (ref: Equation (2-1)) should be sufficiently above 2000 to ensure a turbulent flow regime (Darbyshire & Mullin, 1995). Furthermore, in order to explain the fundamentals of the numerical technique (CFD) which were used to simulate the experiments, some basic concepts of turbulence are introduced in this section.

The occurrence of turbulence can be predicted by use of the dimensionless Reynolds number Equation (2-1). For small Reynolds numbers, fluid viscosity will dominate and the flow will be laminar. For large Reynolds numbers, flows become turbulent and instabilities in the flow are no longer suppressed by viscous forces and the inertial forces prevail.

$$Re = \frac{D \cdot w_{j0}}{\nu} \quad (2-1)$$

Where  $\nu$  [ $m^2/s$ ] is the kinematic viscosity of the plume mixture,  $D$  [ $m$ ] is the pipe exit diameter and  $w_{j0}$  [ $m/s$ ] is the pipe exit flow velocity.

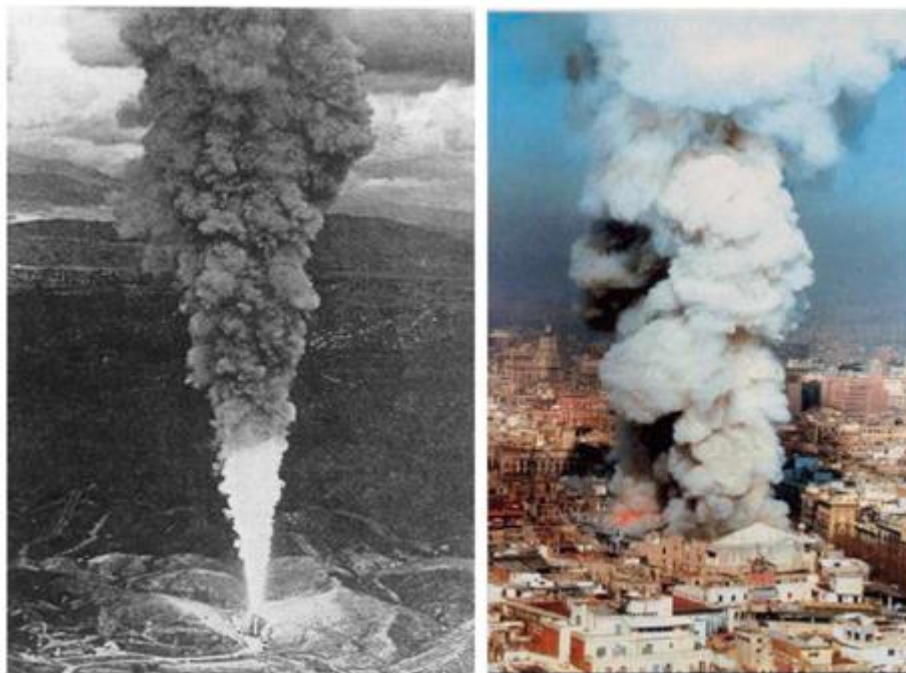


*Figure 2-1 Examples of turbulent flows. (left): A high Reynolds number turbulent jet produced by the test of a rocket in the hills of Redland in California. (right): A thermal plume generated by fire in Barcelona in Feb 1994(Gamma-Imaginechina). Source: Lee and Chu (2003).*

Richard Feynman, a great Nobel Prize-winning physicist, called turbulence “the most important unsolved problem of classical physics.” This means that a precise definition of turbulence does not exist. However, Tennekes and Lumely (1972) mentioned some essential descriptions of the turbulence nature. According to Tennekes and Lumely, turbulent flows are highly irregular and highly diffusive for high Reynolds numbers and contain large three-dimensional vorticity fluctuations. Hence, there is a high energy dissipation caused by molecular viscosity. For turbulent flows, eddies present in the flow cause additional energy decay. These can be captured in a numerical model by increasing the viscous shear stress on the fluid by an eddy viscosity, in which the eddy viscosity is larger than the molecular viscosity. It has been

shown by researchers that for larger Reynolds numbers, the relative importance of the eddy viscosity increases (Kraichnan, 1976).

Natural turbulent flows are irregular and random. These variations are due to a superposition of turbulent structures with different scales passing from an observation point. Because of this, it is impossible to apply a deterministic approach to quantify the flow variables. Instead, researchers rely on statistical methods, for instance, the Reynolds Decomposition, where time-averaged values of the three velocity components and concentration  $u$ ,  $v$ ,  $w$ , and  $C$  are separated from fluctuations  $u'$ ,  $v'$ ,  $w'$  and  $c'$  as follows:

$$\begin{aligned} u &= \bar{u} + u' \\ v &= \bar{v} + v' \\ w &= \bar{w} + w' \\ c &= \bar{C} + c' \end{aligned} \quad (2-2)$$

Another turbulent flow characteristic is the diffusivity, which is responsible for a large part of the transport of momentum and mass. This has consequences for the flow resistance, the mixing, and spreading of discharged plumes in still water. Turbulent jet flows are rotational and hence they contain three-dimensional vorticity fluctuations. If the velocity fluctuations were two-dimensional, random vorticity fluctuations could not maintain themselves since the vorticity is driven by vortex stretching which is a three-dimensional mechanism.

Inside a turbulent flow, the size of the velocity fluctuations relative to the mean is called the turbulence intensity (Equation (2-3)).

$$I_u = \frac{u'_{rms}}{\bar{u}} \quad I_v = \frac{v'_{rms}}{\bar{v}} \quad I_w = \frac{w'_{rms}}{\bar{w}} \quad (2-3)$$

In which,  $(I_u, I_v, I_w)$  [-] are the turbulence intensity components,  $u'_{rms}$ ,  $v'_{rms}$ ,  $w'_{rms}$  [m/s] are the components of the root-mean-square values of the velocity fluctuations. The turbulent kinetic energy,  $k$  [J/kg], present in the velocity fluctuations can be determined as in Equation (2-4):

$$k = \frac{1}{2} \left( \overline{(u')^2} + \overline{(v')^2} + \overline{(w')^2} \right) \quad (2-4)$$

It is important to note that not all turbulent flows are the same. For example, the turbulent jet flows in the present research are different from what is observed in open channel flows, smoke above the chimney or other types of flow. The relative size of the turbulent fluctuations may differ, and hence the shape of the turbulent eddies can also differ. However, the general characteristics of turbulent flows explained above will always hold. The turbulence model used for the numerical simulations will be discussed in CHAPTER 5.

## 2.2.2. Turbulent buoyant jets in a still environment

When jets are released in a still environment, the radial profile of the time-averaged axial velocity is a Gaussian shape with the maximum values of the flow variables at the jet axis. The contrary was found for a radial profile of velocity fluctuations. It was observed by both Panchapakesan and Lumley (1993) and Dai et al. (1995) that the velocity- and suspended particle fluctuation profiles have double peaks away from the jet axis. These double peaks, as shown in Figure 2-2, are created by the shear associated with the radial velocity gradients. This figure shows experimental observations of the root-mean-squared

concentration fluctuations of the vertical centreline profile and horizontal profile, at the level of the center of mass, measured during an advected line puff test.

Another important observation based on experimental data is that incompressible turbulent round jets have the property that the time-averaged velocity gradient goes to zero at the axis, leading to a dip in turbulent intensity (Lipari & Stansby, 2011). Moreover, it has been observed that the radial profile of the Reynolds stresses shows opposite signs on either side of the plume. These observations are explained by the concept that the turbulent transport of streamwise momentum is always directed towards the edge of the jet. At the axis of the jet, this transport comes to a standstill and the time-averaged Reynolds stresses go to zero.

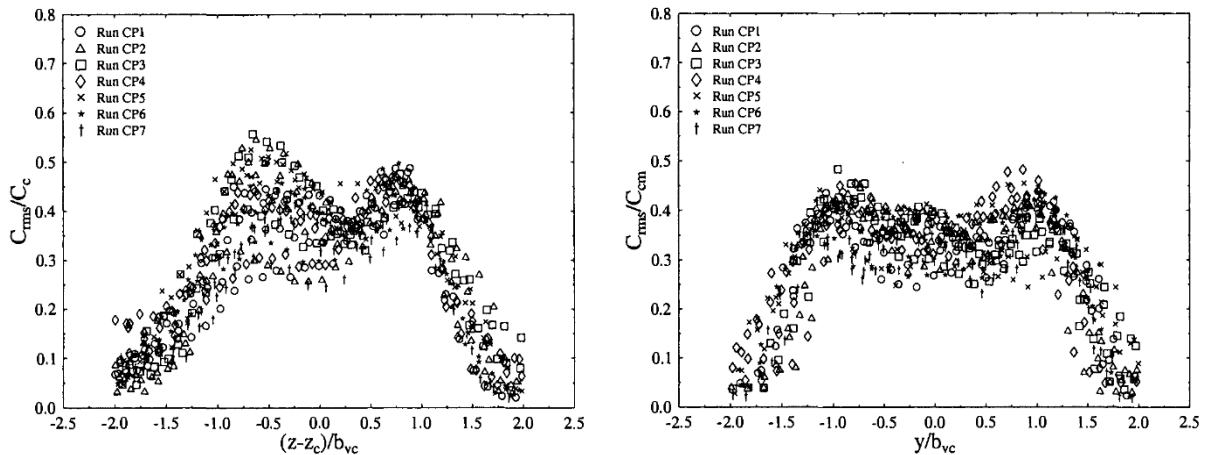


Figure 2-2 RMS concentration fluctuations of an advected line puff. Vertical centerline profile (left) and horizontal profile at the level of the center of mass (right). Experimental data from Lee and Chu (2003).

### 2.2.3. Turbulent negatively buoyant jets in a still environment

The problem under consideration in this research is the time-dependent propagation of an underflow, generated by the vertically downward impingement of a buoyant jet of dense Newtonian fluid on a horizontal bottom boundary.

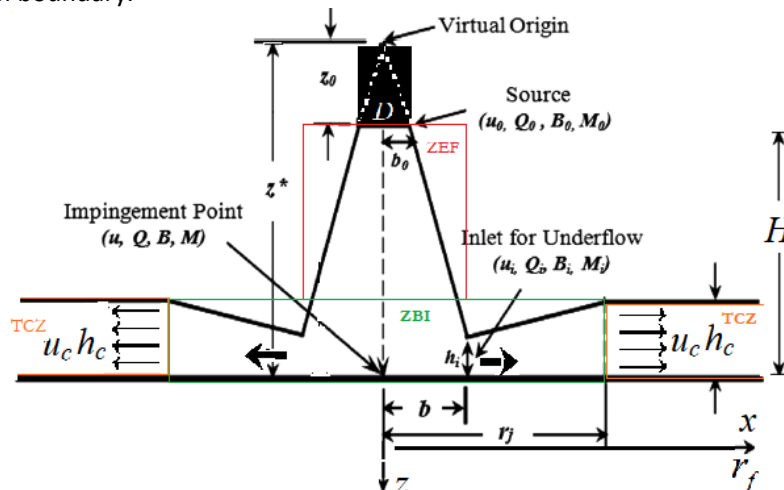


Figure 2-3 Schematic of the underflow generated from a dense buoyant jet impinging on a horizontal bed. Figure adapted from Chowdhury(2014).

As shown schematically in Figure 2-3, a dense fluid with density  $\rho_0$  [kg/m<sup>3</sup>] is discharged with a velocity  $w_{j0}$  from the discharge port with radius  $b_0$ , in ambient water with density  $\rho_a$ . The buoyant jet impinges on the bottom at a distance  $H$  from the discharge port and eventually, an underflow spreads in all directions with

a front radius,  $r_f$  (Chowdhury, 2014). In the presence of a sloped bottom, the dense plume will follow the slope in a downward direction (Fernandez & Imberger, 2008).

Table 2-2 Near-field zones of downward buoyant plumes and impingement

Zones	Description
ZBI	Zone of boundary influence (impingement region)
TCZ	Zone of Established Flow (vertical jet)
ZEF	Turbidity Current Zone (radially horizontal wall jet)

In order to have a good picture of the processes taking place inside the Near-Field Zone, different zones inside the NFZ are defined in Table 2-2 and Figure 2-3. Throughout the following sections, flow patterns in each region will be discussed.

#### 2.2.4. Negatively buoyant jet and plumes

As introduced earlier, a pure jet or plume is only forced by an initial momentum flux or the mass density difference, respectively. However, the studied flow, up to a certain distance from the source of release, is a vertically buoyant jet governed by both the initial momentum and buoyancy flux. Hence they are also called forced plumes (Morton et al., 1956). In the case of a round buoyant jet source, which is the case in this research, top-hat approaches Equations (2-5) to (2-8) are usually used to estimate the initial velocity profile  $w_{j0}$ , the initial volume flux  $Q_0$ , the momentum flux  $M_0$ , the buoyancy flux  $B_0$  and the densimetric Froude number  $F_{r0}$ . The initial variables ( $Q_0$ ,  $M_0$ , and  $B_0$ ) are considered to be the primary variables in the study of forced turbulent jets and plumes. They can be calculated by the following set of equations:

$$Q_0 = \frac{1}{4} \pi D^2 w_{j0}; \quad (2-5)$$

$$M_0 = \frac{1}{4} \pi D^2 w_{j0}^2 = Q_0 w_{j0}; \quad (2-6)$$

$$B_0 = g_0 \frac{\pi}{4} D^2 w_{j0} = g_0' Q_0; \quad (2-7)$$

$$F_{r0} = \frac{w_{j0}}{\sqrt{g_0' D}}; \quad (2-8)$$

In which  $g_0'$  ( $= g[\rho_0 - \rho_a]/\rho_a$ ) [ $m/s^2$ ] is the reduced gravity of the mixture being discharged in ambient water. In this research, the plume extra buoyancy forces are caused by fine particles, which are suspended in the mixture. Tap water was used for both the ambient fluid and in the plume mixture ( $\rho_0 = \rho_w$ ). Hence  $g_0'$  will then be:

$$g_0' = g C_0 \left( \frac{\rho_s - \rho_w}{\rho_w} \right) \quad (2-9)$$

In which  $C_0$  [-] is the initial particle volumetric concentration,  $\rho_s$  the mass density of the solid particles and  $\rho_w$  the mass density of the ambient water (tap water). The conditions at the discharge source can be characterized by a single source balance parameter  $\Gamma_0$ . Morton (1959) defined the following relation for the balance parameter:

$$\Gamma_0 = \frac{5B_0 Q_0^2}{8\alpha \sqrt{\pi} M_0^{5/2}} \quad (2-10)$$

Where  $\alpha$  is the entrainment coefficient obtained from laboratory experiments. A value of  $\alpha = 0.1296$  is applicable to plumes (Hunt & Kaye, 2001). The buoyant jet at the discharge source can be regarded as a forced plume when  $0 < \Gamma_0 < 1$ , a pure plume if  $\Gamma_0 = 1$  or a lazy plume if  $\Gamma_0 > 1$ . Cooper and Hunt (2007) defined three important length scales to determine if the flow is characterized as a buoyant jet or plume:

The source length scale  $L_Q$  and the momentum jet length scale  $L_M$ , defining a length scale for the jet to plume transition. In case of an impinging plume, Cooper and Hunt defined a (virtual) source origin-to-bottom separation distance  $z^*$  as is shown in Figure 2-3.

$$L_M = \frac{(Q_0 w_{j0})^{3/4}}{\sqrt{B_0}} \quad (2-11)$$

$$L_Q = \frac{Q_0}{\sqrt{M_0}} \quad (2-12)$$

### 2.2.5. Negatively buoyant jet spreading

For a single round jet source, the momentum flux  $M(z)$  after distance  $z$  is preserved along the radial cross-section of the jet. Similarly, the mass flux  $Mass(z)$  of a tracer across the jet is constant. Integrating the momentum equation from the jet axis to the radius (see Figure 2-4), Equations 2-13 and 2-15 are obtained for a cross-section at a distance  $z$  from the source.  $V(z)$  is the cross-section volume flux. This approach was also used to calculate the CFD model inputs. Model inputs and boundary conditions can be read in Chapter 4.

$$\begin{aligned} M(z) &= \frac{d}{dz} \int_0^\infty \rho w^2 2\pi r dr = 0 \\ &= \frac{\pi}{2} (w_m^2 b_w^2) = w_{j0}^2 \frac{\pi D^2}{4} = w_{j0} Q_{j0} \end{aligned} \quad (2-13)$$

$$\begin{aligned} Mass(z) &= \frac{d}{dz} \int_0^\infty 2wc\pi r dr = 0 \\ &= \frac{\pi}{2} (w_m^2 b_c^2) = w_{j0} c_0 \frac{\pi D^2}{4} = c_0 Q_{j0} \end{aligned} \quad (2-14)$$

$$V(z) = \frac{\pi b_w^2 w_m}{4} \quad (2-15)$$

### 2.2.6. The entrainment hypothesis

When the plume exits the discharge pipe in still water, the flow develops shear layer vortices as visible in Figure 2-4. These vortices are responsible for entrainment of ambient water into the plume. The most popular closure model is the spreading hypothesis based on experimental observations from Morton et al. (1956). The jet width grows linearly with the distance  $z$  from the source. To describe the complex mechanics of the turbulent behavior observed in many problems with buoyant jets or plumes, the turbulent closure can be solved by the spreading hypothesis:

$$\frac{db}{dz} = const \quad (2-16)$$

Another example of a closure model is based on the entrainment hypothesis, which gives the same solution as the spreading hypothesis for a simple jet. This model has a more physical approach and explains the reason for spreading. In the entrainment model, the entrainment velocity  $u_e$  is assumed to depend on the turbulent intensity which scales with the centreline velocity  $w_m$ , resulting in the following relationship:

$$\frac{u_e}{w_m} = \alpha \quad (2-17)$$

The entrainment hypothesis has been proven to be more robust on the experimental scale (Jirka, 2004). It is important to note that the entrainment hypothesis is a turbulence model; it is appropriate for turbulent jets and plumes (Reynolds number > 2000).

By substituting the expression in equation (2-17) into the continuity equations of the integral model, it leads to the formulation of the following equations for the volume and momentum fluxes over the cross-section (Kundu and Cohen, 2008):

$$\frac{dQ}{dz} = 2\pi u_e \quad (2-18)$$

$$\frac{dM}{dz} = 0 \quad (2-19)$$

Hence, as observed in Equation (2-18), the momentum is preserved for a pure jet experiencing no ambient forcing or boundary interactions.

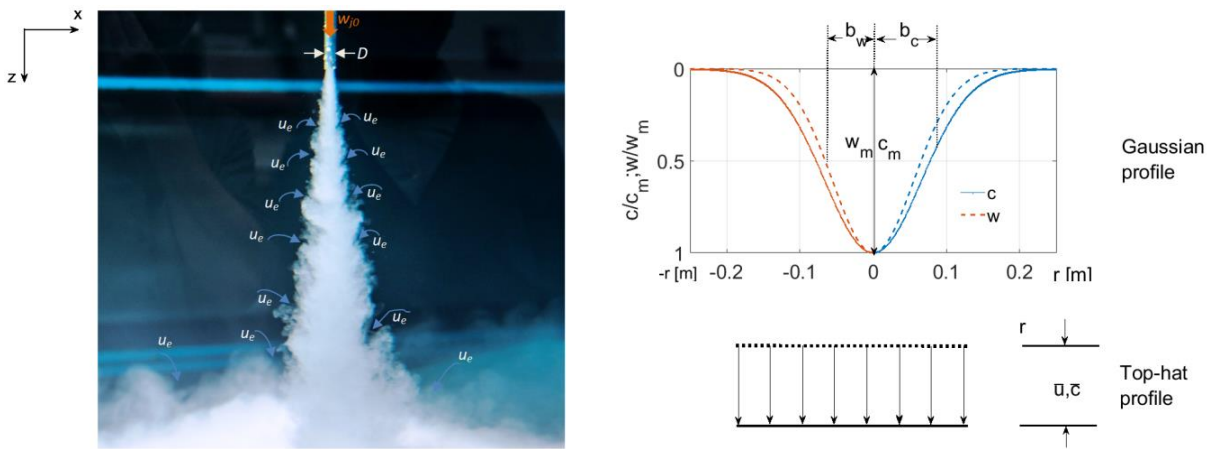


Figure 2-4. Radial velocity, concentration, and top-hat profile. Bottom-right figure reproduced after Chu and Lee (2003). Figure on the right is for an experiment in this research ( $H=1m$ ;  $SSC0=20g/l$ ). Initial  $w_{j0}=0.7m/s$  and the Gaussian profile are obtained at a falling distance  $H^*=1m$  from the source. Photography: Ivar Pel.

### 2.2.7. Negatively buoyant jet profile

The entrainment of ambient water by the jet results in a Gaussian profile for both the vertical velocity and suspended particles concentration. The entrainment of ambient water causes the jet momentum and buoyancy in the jet to approach ambient values far from the plume released point. For axisymmetric plumes, Chu and Lee (2003) defined the jet potential core ( $z < 6.2D$ ) close to the release point as a zone of flow establishment (ZFE). In this zone, the axial velocity and suspended particle concentration is uniform:

$$\left. \begin{aligned} w(z, r) &= w_{j0} \\ c(z) &= c_0 \end{aligned} \right\} \quad \text{for } r < R \quad (2-20)$$

$$\left. \begin{aligned} w(z, r) &= w_{j0} \exp\left(-\frac{(r-R)^2}{b_w^2}\right) \\ c(z, r) &= c_0 \exp\left(-\frac{(r-R)^2}{\lambda^2 b_c^2}\right) \end{aligned} \right\} \quad \text{for } r \geq R \quad (2-21)$$

Where  $r$  is the jet or plume radius [m] and  $R$  is the orifice radius.

Past the ZFE ( $z > 6.2D$ ) comes a zone of established flow (ZEF), where the axial velocity and suspended particle concentration profiles are self-similar and Gaussian with the following expressions:

$$w(z, r) = w_m(z) \exp\left[-\left(\frac{r}{b_w}\right)^2\right] \quad (2-22)$$

$$c(z, r) = c_m(z) \exp\left[-\left(\frac{r}{\lambda b_c}\right)^2\right] \quad (2-23)$$

Where ( $z, r$ ) are the streamwise and radial coordinates, and  $w_m(z)$  and  $c_m(z)$  are the centreline maximum velocity and concentration, respectively. A turbulent round jet is assumed to spread linearly with half-width  $b_w = \beta z$  and  $b_c = \lambda z$ , where  $\beta$  and  $\lambda$  are the plume spreading and dilution coefficients, respectively. These coefficients are determined from experiments by many investigators. Papanicolaou and List (1988) and Dai et al. (1994) found similar values of  $\beta$  equal to 0.108 and 0.104 in their laboratory tests. The work of Papanicolaou and List (1988) suggested  $\lambda = 1.2$ . For this research, values of  $\beta = 0.112$  and  $\lambda = 1.2$  are assumed as suggested by Chu and Lee (2003). These values are also close to camera image analysis from laboratory tests within this research (see chapter 5).

The coefficient  $\beta$  and  $\lambda$  stand for the fact that in buoyant jets, the half-width  $b_w$  and  $b_c$  are proportional to the vertical distance  $z$  from the source. It is important to notice that the experimental results of, for instance, Papanicolaou and List (1988) show that the concentration half-width  $b_c$  is slightly higher than  $b_w$  (see on the right part of Figure 2-4).

### 2.2.8. Top-hat approximation

The governing equations of a steady round jet in the radial-coordinate system are the continuity equation, the  $z$ -momentum equation, and the tracer-mass conservation (Equation 2-14 and 2-16). The key physical variable controlling the jet mixing is the jet momentum flux and can be written in terms of integral fluxes (Equation (2-18)). In fact, based on physical insight, all characteristic properties of a round jet can also be related to a single constant by dimensional reasoning. It is then very useful to represent the mass- and momentum fluxes by a top-hat profile as shown in Figure 2-4. This also explains why the momentum and mass flux integral can be evaluated by assuming a simple velocity profile.

$$w = \begin{cases} W & \text{if } r \leq B \\ 0 & \text{otherwise} \end{cases} \quad (2-24)$$

Where  $W$  and  $B$  are the velocity and half-width of an equivalent jet with a sharp boundary and uniform velocity that is carrying the same mass flow and momentum flux as the actual jet. By equivalence of mass and momentum fluxes, the following relations between the two profiles explained above can be obtained (See also Figure 2-4):

$$\begin{aligned} \pi WB^2 &= \pi w_m b_m^2 \\ \pi U^2 B^2 &= \pi w_m^2 b_m^2 \end{aligned} \quad (2-25)$$

Thus, the link between a top-hat and Gaussian formulation are obtained by calculating the mean values of the velocity ( $w_m$ ) and particle concentrations ( $c_m$ ) from the Gaussian profiles (see Equations (2-26)). The

average concentration or dilution can be deduced from the sediment tracer mass conservation (Chu et al., 1999).

$$W = \frac{w_m}{2}$$

$$B = \sqrt{2} b_m \tag{2-26}$$

$$C = \frac{c_m}{2}$$

The top-hat profile assumes a uniform velocity and concentration distribution across the jet. The velocity and concentration of the top-hat profile are the average velocity and concentration of the dominant eddies (large eddies) occupying the jet cross-section. They are responsible for the overall transport of mass and momentum. Small eddies that are present in the flow circulate within the dominant eddies and they are assumed to have no net effects on the overall transport. Hence, it is practical to calculate the mass and momentum fluxes based on the top-hat profiles (Lee & Chu, 2003). This statement justifies the usage of the top-hat profile for the dominant-eddy hypothesis, especially if quick estimations are needed, for instance when using an integral model for jets and plumes (Jirka, 2004). The dominant-eddy hypothesis and the connection between the top-hat and Gaussian profile are discussed in detail in Chu and Lee (2003).

## 2.3. Turbidity Currents

### 2.3.1. Introduction

it was introduced that a negatively buoyant jet impinges on a horizontal bed and spreads radially as shown in Figure 2-3, an underwater flow called in this research “turbidity current”. In the field of marine geology and oceanography, turbidity currents are classified as members of the “dense bottom flows”, which includes debris flows and thermohaline bottom flows. The presence of a dilute suspension of sediment in the water renders a turbidity current slightly heavier than the ambient water. A submarine debris flow consists of such a dense sediment-water slurry, that it can create its own sediment-water rheology. Sometimes it may behave as a non-Newtonian fluid in which suspended particles drag the flow with them as the current flows downstream.

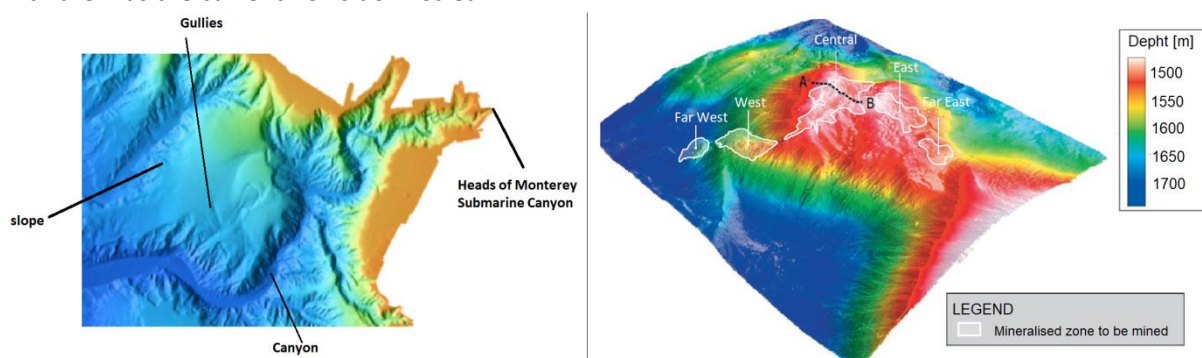


Figure 2-5 Example of seabed bathymetries. Monterey submarine canyon of about 1 km wide (source: D. Smith, USGS)(Left image). 3-dimensional topographic features of of proposed mining area at Salwara1project in Papua New Guinea (Source: Nautilus Minerals Niugini)(right image).

The seabed is not always flat; it has steep slopes, risers, gullies, canyons, among other features, sometimes with active margins as shown in Figure 2-5. In this figure, steep underwater canyon can be observed, they are formed by the underwater erosion process known as turbidity current erosion. The current is created by a local disturbance such as an earthquake and then flows downslope under the

influence of gravity as shown in Figure 2-5. The current erodes the bed which in turn increases the density of the current. Seabed bathymetry such as in Figure 2-5 is complex to be studied on a laboratory scale, hence simplification is made by using a uniform slope as shown in Figure 2-5.

Another important phenomenon to note is that turbidity currents differ from thermohaline underflows because they are free to exchange sediment with the bed. To keep their existence, turbidity currents keep the sediment in suspension to sustain themselves or otherwise die out. This is different for river flows, as the river flows at an air-interface, while a turbidity current is a sediment-laden current flowing at a water-interface. Because of that, rivers usually form sharp interfaces with the air above, while turbidity currents form more diffuse interfaces with the water above. The flow patterns and characteristics of turbidity currents (underflows) from an impinging buoyant jet in still water are divided into two regions. The region close to the impingement point is defined as a zone of boundary influence (ZBI), and a turbidity current zone (TCZ) away from the impingement point where the turbidity current is fully developed.

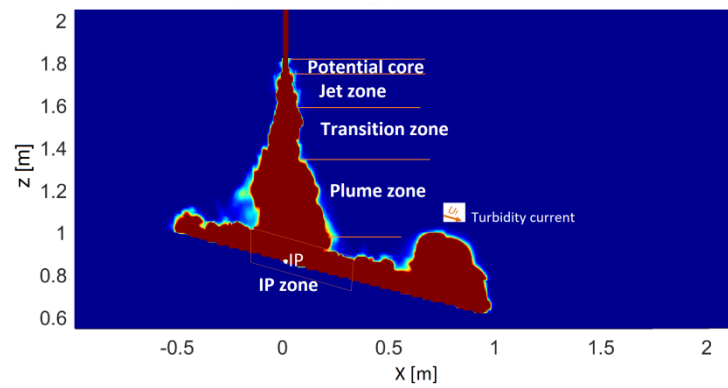


Figure 2-6 Centre slices of a turbidity current resulted from a CFD simulation with the plume released from a height  $H=1m$  containing  $SSC_0=20g/l$  impinging on a sloped bed. The current front position plotted by tracking 10% of initial  $SSC_0$  released from the source.

### 2.3.2. Sediment fall velocity in still water

In all three zones (ZEF, ZBI, and TCZ) of impinging buoyant plumes (Table 2-2), under the influence of gravity, sediment particles are settling. The terminal settling velocity is reached when buoyancy and drag forces reach equilibrium. For fine sediment particles, the terminal settling velocity can be estimated by Stokes' law Equation (2-27) obeying to a laminar regime and is applicable for  $1 < D_p \leq 100\mu m$ . For courser particles with  $100 < D_p \leq 1000\mu m$ , the formula of Ruby and Zanke Equation (2-28) can be used:

$$w_{op} = \frac{(\rho_s - \rho_w)gD_p^2}{18\rho_w\nu} \quad (2-27)$$

$$w_{op} = \frac{10\nu}{D_p} \left[ \sqrt{\frac{(\rho_s - \rho_w)gD_p^3}{100\rho_w\nu^2}} - 1 \right] \quad (2-28)$$

Where  $w_{op}$  is the particle settling velocity,  $\rho_s$  and  $\rho_w$  are the density of sand and water, respectively.  $D_p$  represents the particle diameter and  $\nu$  = kinematic viscosity [ $m^2/s$ ].

When SSC is high, particles settle in a confined space and sediment particle-particle interactions are no longer negligible. In that situation, the settling velocity of the individual particles reduces. The influence of the volume concentration on the settling velocity of a mixture with uniform particle sizes is written in

Equation (2-29) (Richardson, 1954). Hindered settling is caused by the return flow, which is created by the settling particles and the increase in particle-particle collisions.

$$w_s = w_0 (1 - C_t)^n \quad (2-29)$$

$$C_t = \sum_{l=1}^{n \text{ frac}} C_l \quad (2-30)$$

Where  $w_0$  is the settling velocity of an individual particle and  $C_t$  total volume concentration Equation (2-30) in which  $C_l$  is the volume concentration of fraction  $l$  in case the sediments material contains many sediment fractions.

According to Richardson and Zaki (1954), the coefficient  $n$  in (2-30) varies between 2.39 for coarse particles and 4.65 for fine particles. According to Van Wijk et. al (2012), for coarse gravel this equation still holds and a value of  $n = 2.4$  as was found with fluidization experiments. A more convenient way to compute the value of  $n$  is the method of Rowe (1987) using equation (2-32) which is a smooth representation of the original relations of Richardson and Zaki (1954). Based on the expression in equation (2-32),  $n$  is a function of the particle Reynolds number (Equation (2-31)). The reduction in the settling velocity will be less for a group of coarse particles compared to fine particles because of the lower value of the exponent.

$$Re_p = \frac{w_{0,p} D_p}{\nu} \quad (2-31)$$

$$n = \frac{4.7 + 0.41 Re_p^{0.75}}{1 + 0.175 Re_p^{0.75}} \quad (2-32)$$

Based on experience in the field of dredging, finer sediment settles slower in a hopper compared to coarser sediments, hence an overflow plume generally contains more mud ( $D_p < 63\mu\text{m}$ ) and fine sand than other dredged material (Van Rhee, 2002). The same can be expected for DSM plumes released in the ocean. Once plumes are created in deep water, the sediment in turbidity currents will be mainly in the form of mud, which is a good driver to get both sand and gravel suspended from the bed. Under the influence of turbulence, mud particles can cluster together to form flocs, with typical sizes of 0.01-1 mm. The density of mud flocs is less than the density of individual mud particles, but the settling velocity is larger, hence flocculation is important especially when the mud concentration will be large. Within this research, flocculation is not taken into account. The used sediment consists of grinded, non-cohesive quarts powder and hence, because of its particle shape and neutral electric charge, no floc formation is possible during laboratory tests (see Figure 3-4). Detailed research on the dynamics of high-concentrated mud suspensions and flocs can be found in Winterwerp (1999).

### 2.3.3. Zone of boundary influence (ZBI)

When a buoyant jet is discharged in an ambient fluid of less density and finite depth, the jet descends as a vertical buoyant jet until it impinges on the bottom. Inside the ZBI, after the jet impinges, it flows in a radial direction from the impingement point (Chowdhury & Testik, 2014). Depending on the initial jet conditions and the conditions of the ambient water, as well as the ratio  $Z^* / L_m$ ; the jet impingement parameters are of "jet-like impingement" when  $Z^*/L_m < 1$ . Otherwise, it is a "plume-like impingement" when  $Z^*/L_m > 5$ . Between the two conditions, the jet is considered to be in a transitional regime before the impingement. As shown in Figure 2-3,  $Z^*$  is the height of the virtual origin of the jet orifice measured

from the impingement point at the bottom. Length  $L_m$  was introduced earlier in Equation (2-11) and represents the jet-to-plume length scale.

Figure 2-3 shows how after the impingement, the underflow exhibits two propagation phases. The first is an initial adjustment propagation phase which is located near the impingement point and where the fluid flow is radially driven by momentum. As the underflow continues to flow away from the impingement point, buoyancy becomes dominant over the momentum, transforming the underflow to eventually behave as a fully developed gravity current (Kaye & Hunt, 2007). In the case where buoyant jets impinge on a flat plate as momentum dominated jets, investigations confirmed that the transition from initial adjustment phase to gravity current phase also scales by the characteristic jet length scale  $L_M$  and the discharge source-bottom separation distance  $Z^*$ .

Recent research (Chowdhury & Testik, 2014) determined empirical relations in order to estimate the flow variables ( $Q_i$ ,  $M_i$ ,  $B_i$ , and  $F_i$ ) at the point of transition from a vertical buoyant flow to an underflow, which eventually becomes an Inertial Gravity Current (IGC). However, these formulas are not universal; they are applicable only for underflows from the impingement of buoyant jets containing cohesive particle-laden mixtures. For non-cohesive particles, there is experimental data available of particle-laden underflows in rectangular tanks, representing two-dimensional underflows using sand particles (Hogg et al., 2005, García, 1993 and Garcia, 1994).

The most recent related research is from Christodoulou et al. (2016), regarding the near-field dilution of salt-water mixtures from a vertical dense jet impinging on a solid boundary. Authors in the paper proposed dimensionless empirical equations, which are in terms of geometrical parameters and the densimetric Froude number. Their results can be used to estimate the dilution at the impingement point and along the pathway of the density current that flows near the bed.

At the impingement point (see Figure 2-3), the local specific fluxes (per unit density) for the local momentum, buoyancy, volume flux, and apparent gravitational acceleration are referred to as local impingement parameters. Thereafter buoyancy is conserved. An important parameter of interest is the distance  $r_j$  marking the end of the ZBI over which the underflow transforms into gravity currents. Experimental investigations by Kaye and Hunt (2007) show that for a plume-like impingement, the radius  $r_j$  is primarily governed by the length scale  $Z^*$ .

#### **2.3.4. Gravity Currents**

Near the impingement point, the flow propagation is an initial flow adjustment and the flow can be defined as a supercritical flow. However, after a certain distance of radial spreading, the velocity decreases so that in some cases, an internal hydraulic jump can occur (Wilkinson & Wood, 1971). In general, experimental observations show that at a radial position of  $r_f \gg 10D$ , the current thickness starts to increase rapidly, indicating an internal hydraulic jump (Wilkinson & Wood, 1971). In Figure 2-3, the internal hydraulic jump occurs at a radius  $r_j$  from the impingement point. After this distance, the flow becomes a regular density current driven by the excess buoyancy of the plume. Measurements show that the current height  $h_c$  is typically double across the jump and  $u_c$  is nearly halved. As the jump is traversed, the point in a vertical profile where the maximum flow velocity is attained rises remarkably, which indicates that there is rather a sudden decrease in bed shear stress on the subcritical (downstream) side of the jump (Garcia, 1989).

When the spreading radius of the front position  $r_f > r_j$ , the underflow is considered as a constant-flux release of the inertial-gravity current which is fully developed. Both experimental and theoretical

investigations agree that the radial front position  $r_f$  of the inertial gravity current follows a functional dependency on propagation time with  $r_f \sim t^{0.8}$ . Figure 2-7 shows a typical velocity- and concentration profile of an underwater density current including the interface between the current and the quiescent water. Both the velocity and sediment concentration go to zero beyond the theoretical interface.

### 2.3.5. Sediment transport in turbidity currents

To be able to estimate the amount of sediment deposited or eroded due to the interactions between the density current and the seabed; the transport of sediment must be understood. Therefore, the theory of sediment transport within turbidity currents is treated in this section. Turbidity currents obtain their driving force from the submerged weight added by the presence of sediment, generally mud and/or fine sand in suspension, i.e. dispersed in the water column away from the bed. This suspension is necessary to drive the flow. Turbidity currents can also transport sand, and sometimes gravel as bedload. However, in this research, only non-cohesive particles were studied using quartz powder with  $D_{10}= 15 \mu\text{m}$ ,  $D_{50}= 36 \mu\text{m}$ , and  $D_{90}= 70 \mu\text{m}$  (see Figure 3-4). There was no clay present in the experiments, therefore particles behaved as non-cohesive sediment. For that reason, attention will be made to only the transport of fine sand particles.

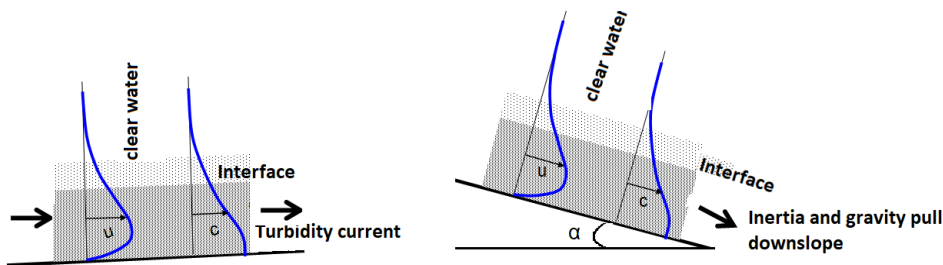


Figure 2-7 Turbidity current flow velocity and suspended sediment concentration profiles.

Sediment transport is divided into three groups: wash load, suspended load, and bed load ( Figure 2-8 ). Based on the origin of sediments, there are bed material loads and wash-loads. Based on the various transport mechanisms, there is a distinction between the bed load and suspended load, see on right side of Figure 2-8. Suspended sediment is necessary for turbidity currents to exist as they are the drivers of the flow. Because suspended sediment in turbidity currents is composed of mud (Silt and clay) or finer sand ( $d < 62.5 \mu\text{m}$ ), they are often approximated as wash load.

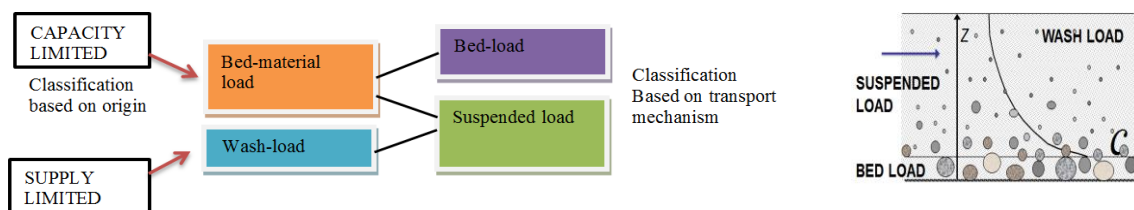


Figure 2-8. Classification of sediment transport mode in a river (Crosato lecture notes, 2012, UNESCO-IHE).

The bed material load is the part of sediment load that exchanges particles with the bed and thus contributes to the morphodynamics of the bed. The suspended load is transported in suspension and feels the direct dispersive effects of eddies and is hence wafted high into the flow. Depending on the intensity of turbulence and fall velocity of the grains, sediment remains in suspension for some time and can cover some distance without exchange with the bed.

### 2.3.6. Sediment concentration in turbidity currents

Bodies of water such as rivers, flow downslope under the influence of gravity. The gravity which acts on the water mass, causing the water to drag sediment with it. Suspended sediment carried by the water adds only slightly to the driving force, as long as the volume concentration of suspended sediment  $C \ll 1$ .

However, turbidity currents flow downslope under the influence of gravity, which is acting on the sediment, and then the sediments drag water with it (Morris, 2000). It is important to note that turbidity currents die out as the sediment concentration dilutes to background values. The reason for the concentration to drop to zero is due to the settling of the suspended sediments, in which case the turbidity current has lost the capacity to keep them in suspension. The reduction of suspension capacity is due to a significant friction associated with the turbidity current interfaces, with clean water on the top and the bed friction below, as well as friction losses due to fluid viscosity.

In a homogeneous and well-mixed turbid fluid, the suspended sediment concentration can be calculated by equation (2-33). In a homogeneous turbid flow, there must be a balance between settling of sediments and turbulent diffusion. However, for higher sediment concentrations in the fluid, settling can dominate in which case a higher concentration is found closer to the bed.

$$C = 10^{-6} \frac{SSC}{\rho_s} \quad (2-33)$$

A current with a homogeneous and low sediment concentration experiences less hindered settling effect, thus a higher settling velocity for the particles. For deep-sea mining plumes, inside the flow, the vertical SSC-profile is given by the Rouse profile:

$$\frac{C}{C_a} = \left( \frac{z_a}{h - z_a} \frac{h - z}{h} \right)^{SP} \quad (2-34)$$

In which  $SP$  is the Rouse suspension parameter. Given by:

$$SP = \frac{w_s}{bku^*} \quad (2-35)$$

Where  $b = 1$  and  $C_a$  is the reference concentration (near bed concentration) at a vertical level,  $z_a$  is its reference distance to the bed and  $u^*$  is the bed shear velocity. The Rouse number reflects sediment properties in  $w_s$  and flow properties in  $u^*$ . Note that the critical shear stress decreases for larger particles and high concentration  $C_a$  for high velocities and small particles.

### 2.3.7. Interaction of the turbidity current with the bed

In turbidity currents, suspended sediment close to the bed can deposit. The deposition flux of sediment fraction  $l$  is given by:

$$Dep_l = c_l \rho_l w_l \quad (2-36)$$

Where  $Dep_l$  is the deposition flux of sand or mud fraction  $l$  in  $[\text{kg/s per m}^2]$  and  $c_l$  the volume concentration of fraction  $l$ . In CFD, this is the volume concentration in the first computational cell above the bed and  $w_l$  the drift velocity of sediment fraction  $l$  (De Wit, 2010). The calculation of fine sediment erosion at the bed can be done by using the classical description of the Partheniades formulation for the erosion flux as in equation (2-37):

$$Ero_l = \begin{cases} M_l \left( \frac{\tau - \tau_c}{\tau_c} \right) & \text{for } \tau > \tau_c \\ 0 & \text{for } \tau < \tau_c \end{cases} \quad (2-37)$$

With  $E_{r0}$  the erosion flux of sand or mud fraction  $l$  in  $[\text{kg/s per m}^2]$ . For cohesive sediments, Van Rijn (1993) proposed  $[10^{-5} - 10^{-4}] \text{ kg/s per m}^2$  as erosion rate  $M_l$  and  $[0.15 < \tau_c < 0.5 \text{ N/m}^2]$  for  $\tau_c$ , which is the critical bed shear stress for erosion. If the value of  $M_l$  is equal to zero, erosion is ignored. This can be applied predominantly to the sand phase, as the error made by neglecting erosion of sand phases is small, as sand will deposit on the bed quickly.

## CHAPTER 3

# Experimental facilities

---

**This chapter explains the experiments carried out in the dredging laboratory of TU-Delft. The details of the laboratory facilities, the experimental size, and the setup and tests scenarios will be systematically described. Also, the used measurement techniques will be explained in this chapter.**

### 3.1. Introduction

As was introduced in the problem statement in Chapter 1, there is a growing need in the offshore mining industry for better predictive tools for turbidity plumes generated from DSM activities. In order to minimize the environmental impacts thereof, DSM from the early stages of planning until the project execution, dedicated and accurate predictive tools must be developed to allow for predictions of the impact in advance and for mitigation measures to be proposed. These tools include a numerical model, which is probably the most effective tool to predict the physical of these dense plumes which will be discharged back near the seabed. However, predictions from a numerical model need to be validated with laboratory experiments and field data. In this research, the near-field length of 5 m in the experiments was scaled down 1:50 to represent a near-field length of 250 m. This scale was chosen based on the available space within the experimental facility and to stay safely above the Reynolds number of 2000 to assure a turbulent discharge.

The aim of this research is to predict the flow velocity and concentration of the turbidity current inside the near-field area of a 125 m radius around the impingement point. To this end, laboratory experiments first aim to improve understanding of the physical processes involved concerning the impingement of a turbulent dense jet or plume on the sea floor. The secondary aim was to analyse and quantify the plume-spreading rate, its pathway and mixing with the ambient water. Furthermore, it was necessary to experimentally study interactions between the turbidity current and the seabed topography (sedimentation and erosion). The experimental setup was designed with the ability to change the bottom surface slope, in order to analyze the effect of the slope and the conditions in which turbidity currents are formed. Experimental procedures include the creation of plume mixtures (tap water + suspended sediment). Millisil silica flour (or quartz powder) with a particle size distribution shown in Figure 3-4 was used to this end. To ensure a well-mixed and homogeneous plume mixture, a submerged pump kept particles in suspension by circulating the flow in the reservoir. A second pump “jet pump” was used to pump the fluid mixture from the reservoir via a flexible hose, to a vertical pipe submerged into a modular tank filled with still ambient water, mimicking the deep sea. An artificial seabed was represented by a table as shown in Figure 3-2. Experiments involved a wide range of initial parameters: a constant and fully developed flow rate equal to 3.3 l/min, three different heights of the discharge pipe relative to the bottom, three different initial suspended sediment concentrations of the plume and two different bed slopes; flat sea-bed conditions and a 10-degree slope. More details of the experimental design and choice of parameters will be described separately in this chapter.

## 3.2. Experimental setup

### 3.2.1. The modular tank

Studied turbidity plumes and currents were under deep-sea water conditions in terms of sediment-laden, with the fine sediment particles that move in the flow as suspended load. To mimic the deep-sea, a modular tank of 5 m long, 2.25 m wide and 2 m height was designed and built to represent underwater conditions for a field length of 250 m long on a scale of 1:50. The comparison between the field parameters and experiments are reported in Table 3-1.



Figure 3-1 Experimental setup. A tank full of 23 m<sup>3</sup> tap water. (Picture was taken by Ivar Pel (© NWO)).

A setup of the modular tank is shown in Figure 3-2. It built with metal frames and several transparent glass windows for visual observations, see Figure 3-1. The transparent glass windows gave the possibility to see the physical processes during the tests, to record videos and take pictures for further analysis. At the top of the modular tank, horizontal beams with sliders were installed to support the measuring instruments, giving them a possibility to move accurately from one location to another and fix them.

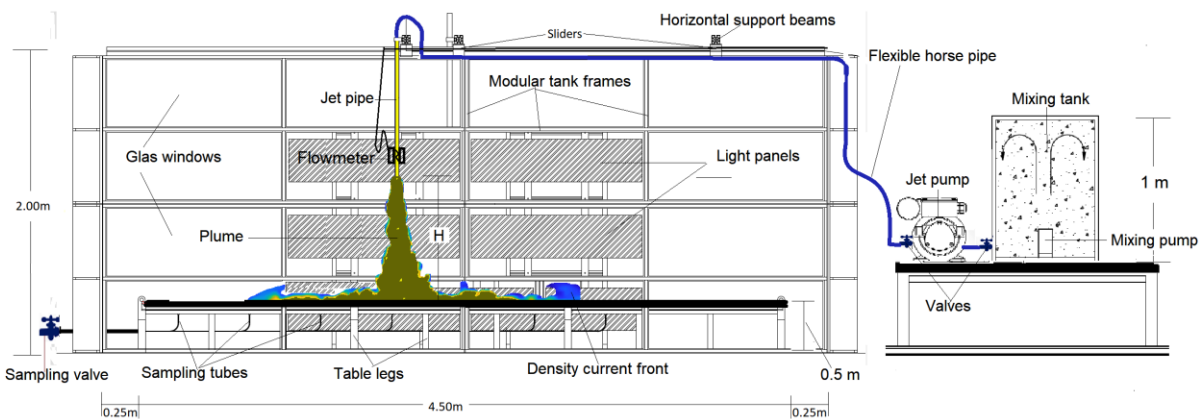


Figure 3-2. Main parts of the experimental setup: Front view of the modular tank, mixing tank and table inside the modular tank.

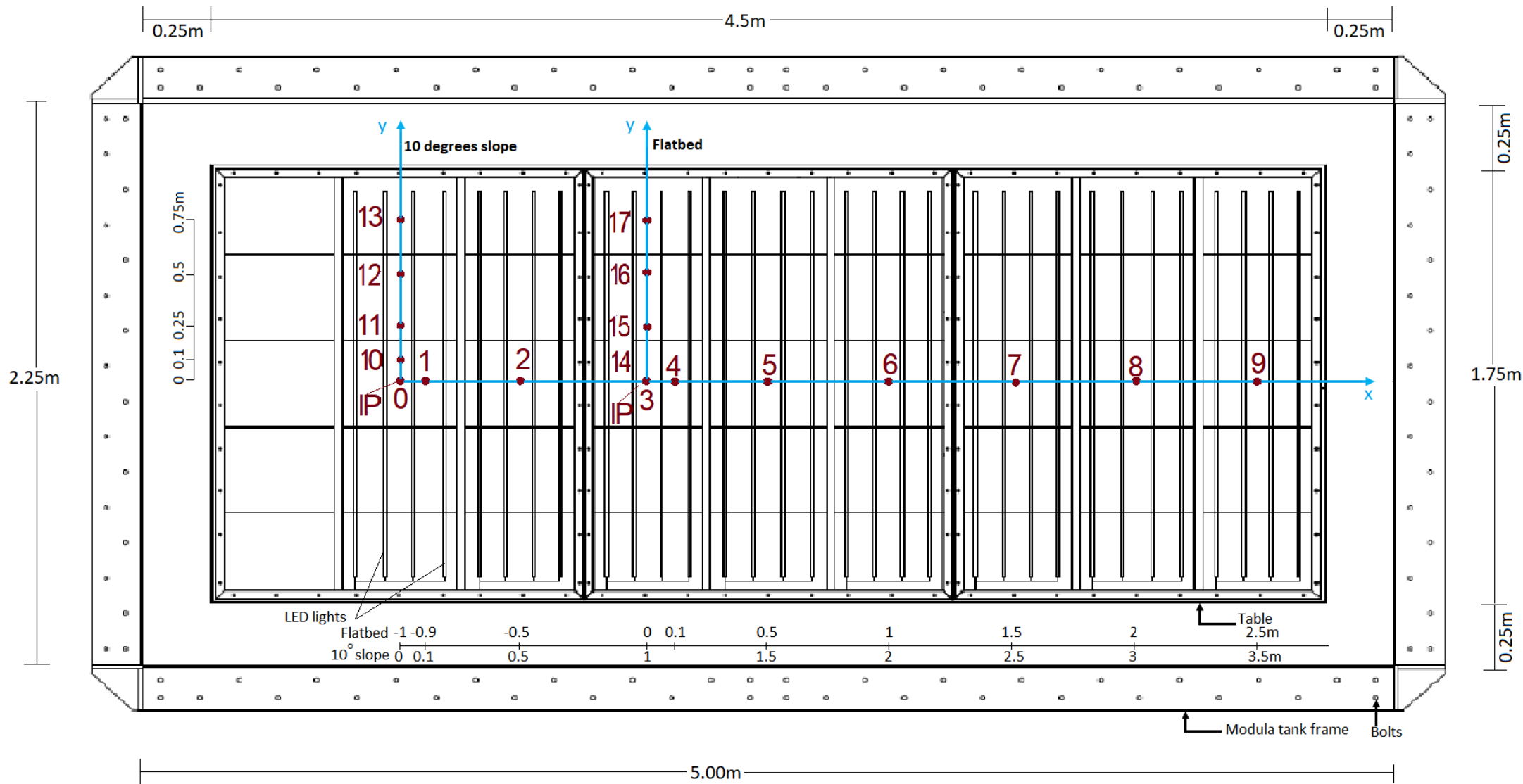


Figure 3-3 Experimental measurements map: Top view of the modular tank and table with Plexiglas surface with installed underwater lights.

### 3.2.2. The artificial seabed table

As depicted in the front view of the experimental setup shown in Figure 3-2, a table was positioned in the centre of the tank to represent an artificial seabed. The table is made of (non-corrosive) aluminum frames to support the artificial seabed surface made of smooth PMMA (acrylic glass panels, also called Plexiglas). The vertically descending flow impinges on the acrylic glass surface panels after which the density current flows radially away from the impingement point (IP) towards the edges of the table. The measurements of current velocity and SSC are also taken right above the table surface. The artificial seabed (the table) is 4.5 m long, 1.95 m wide and 1 m high, hence its horizontal dimensions are a smaller than the modular tank (5x2.55x2m); see the top view of the laboratory experimental set up in Figure 3-3. As the table is smaller than the modular tank, it allows the created turbidity current to fall over the table, thereby minimizing the wall influence on the studied process.

Table 3-1. Experiment Froude scaling (1:50)

	Laboratory	Field	Unit
<b>Jet Discharge</b>			
Pipe diameter	0.01	0.5	[m]
Jet velocity	0.7	5	[m/s]
Plume density	1003, 1006, 1012.5	1003, 1006, 1012.5	[kg/m <sup>3</sup> ]
SSC	5, 10, 20	5, 10, 20	[g/l]
Pipe orifice height (H)	0.25; 0.5; 1	12.5,25,50	[m]
<b>Tank</b>			
Length	5.00	255	[m]
Width	2.250	113	[m]
Height	2.00	105	[m]
Water temperature	8 – 20	2 – 6	[C°]
Water Density	998 - 1000	1030–1040	[kg/m <sup>3</sup> ]
<b>Table</b>			
Length	4.5	225	[m]
Width	1.75	98	[m]
Height	1.00	50	[m]

To increase the flow visibility, artificial underwater lights were installed under the horizontal Plexiglas slab (see Figure 3-3). The same was done for the vertical glass windows at the back of the modular tank where vertical light panels were positioned as shown in Figure 3-2. Through the horizontal table surface panel made of Plexiglas slab, several tubes represented by points  $P_i$  numbers in Figure 3-3, were connected along the longitudinal (x) symmetry-axis. At the other end of each tube (the modular tank wall), a ball valve, here called “Sampling valve”, was installed to take samples for the local Nephelometric Turbidity Unit (NTU) measurements. The dimensions and scale of the table can be found in Table 3-1 and The numbers in Figure 3-3 represent the velocity and SSC measured point’s locations and the sampling tubes connection points.

### 3.3. Sediment minerals

The sediment used is the commercially available Millisil M6 ( $\rho_s = 2650 \text{ kg/m}^3$ ) produced by Sibelco Benelux by iron-free grinding of silica sand containing 99% of  $\text{SiO}_2$  as raw material. Millisil sediment has a narrow particle size distribution (see Figure 3-4), which minimizes the differences between settling velocities, thus simplifying the interpretation of results. The presence of very fine particles would permanently blur the water after the experiments and increase the ambient sediment concentration of the tank water, requiring an exchange of water after each measurement. This had to be limited because of the waste of 25.000 l of tap water per experiment, and the tank takes about 15 hours to fill with the

available water supply sources in the laboratory. Hence, for this reason, very fine particles were removed from the raw material.

Using Equation (2-29), the settling velocity of the unwanted finer particles was calculated. With a mixing tank and the mixing pump shown in Figure 3-4, the sand was mixed with water and for the required particle sizes with  $D > 20 \mu\text{m}$ , it was found that 60 min was required for the sediments to settle down at the bottom of the mixing tank while the fines were still in suspension. The fines were then removed by emptying the turbid water from the mixing tank. The process was repeated 6 times. As can be seen in the particle size distribution curve, the new filtered sediment sand was produced with a  $D_{10} = 15 \mu\text{m}$ ,  $D_{50} = 36 \mu\text{m}$ , and  $D_{90} = 70 \mu\text{m}$ .

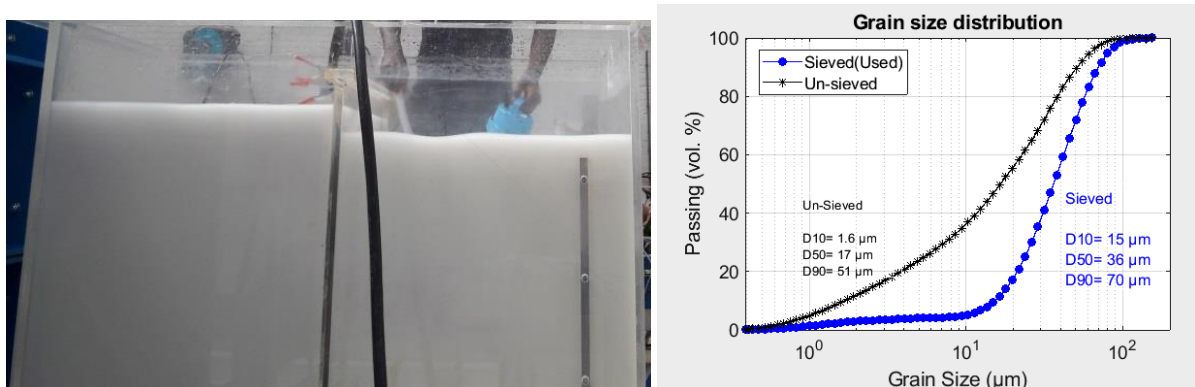


Figure 3-4 0.8 m<sup>3</sup> Mixing tank/reservoir (left) and grain size distribution (right).

Based on the particle size distribution in Figure 3-4, the obtained sediment after the filtration still had a small percentage of fine particles smaller than 20  $\mu\text{m}$ . Quartz powder eases the production of homogeneous mixtures and does not cluster together to form flocs due to its neutral electrical charge. Due to this property, the material was considered in the experiments. Its particle size distribution is comparable to mud, which is expected to dominate in the deep sea mining plumes. Although there are no consistent predictions for an expected particle size distribution for DSM plumes, the return plumes will most likely contain small particles. The sediment in this research was chosen as the best fit between sediment available on the market and the laboratory research requirements.

### 3.4. Sediment mixing tank

To ensure a statistically steady and homogeneously mixed plume over time, the sediment-water plume mixture was release via a flexible hose from a 0.8 m<sup>3</sup> rectangular shape mixing tank positioned next to the modular tank as shown Figure 3-2. To achieve the homogeneity of the plume leaving the discharge pipe, a 100 l/h submersible pump was placed on the bottom of the mixing tank. The mixing tank (see Figure 3-4) has two compartments with the same sizes, each large enough to keep the sediments in suspension within the mixture, while providing sufficient mixture for the entire test of 40 minutes.

The jet pump was installed between the mixing tank and the modular tank and pumped the mixture at a required steady flow velocity. Between the mixing tank and the jet pump, a valve was installed to close off the flow until a homogenous mixture was achieved before the start of any test. The homogeneity of the suspended sediment in the mixing tank could have been monitored by taking mixture samples from the mixing tank (before, during and at the end) of each test. To save time, however, random samples were taken and measured by an NTU meter, which indicated an acceptable maximum deviation of 10% from the desired SSC. For a description of the NTU measurement, please refer to section 3.8.

### 3.5. The discharge Jet pipe

To produce a turbulent jet flow of 3.3 l/min ( $Re \sim 7200$ ), an impeller pump (010 Size Flexible Impeller AC Motor Pump Unit, 50010 Series) was used to pump the mixture from the reservoir to the tank via an aluminum pipe. To achieve a scale of 1:50, a 10 mm diameter and an initial jet velocity of  $W_{j0} = 0.707$  m/s (Pipe discharge  $Q_0 = 3.33$  l/min) was needed to experimentally represent a field scale of 0.5m pipe diameter discharging a negatively buoyant jet of  $w_{j0} = 5$  m/s. These values were chosen as averages resulting from consultation and recommendations given by industrial experts.

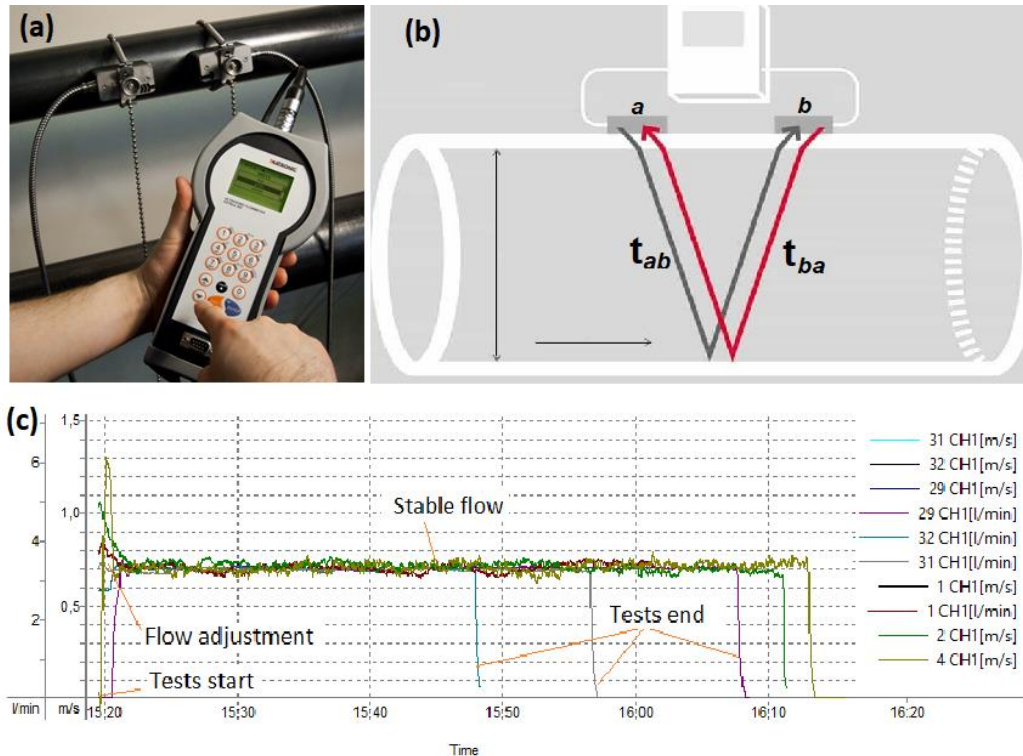


Figure 3-5 Katronic KATflow 200 in operation (A), Working principle (B) and Flow hydrograph.

Although it is obvious that during offshore mining activities the return flow will vary and different pipe diffusers are expected to be considered, for simplicity, this research was restricted to a single pipe diameter with a constant flow velocity. A constant discharge flow rate was regulated by the jet valve with the help of a flow meter (Katronic KATflow 200).

KATflow is a portable instrument with two transducers fixed on the pipe wall. As shown in Figure 3-5, the key working principle of the instrument is that sound waves traveling with the flow will move faster than those traveling against it. Hence, the difference in the transit time of these signals is proportional to the flow velocity of the liquid and consequently the flow rate. Before the use, the instrument needs to be set and adjusted to the pipe and flow characteristics. For the instrument calibration, a known volume of the mixture was pumped over a fixed time and compared with the instrument output registered flow volume.

It was advantageous to use the KATflow, as the instrument displays the instantaneous flow velocity or flow rate, which gave a possibility to set the flow before the start of the tests (see Figure 3-5). Also, in case for any reason the flow rate changes, it was possible to quickly stabilize the flow to the required jet discharge of 3.33 l/min by turning the ball valve between the pump and the jet pipe. In Figure 3-5, several KATflow recordings time series of the velocity profiles are shown (velocity in m/s and flow rate in l/min). As can be seen in this plot, the flow rate is zero at the beginning of the tests. Within the first minute of the tests, the flow was regulated and kept close to 3.33 l/min until the end of the test when the discharge pumps were switched off to bring the flow rate to zero.

### 3.6. Experiment scenarios

Two series of nine experiments were carried out. For each experimental series; three different initial suspended sediments concentrations ( $SSC_0$ ) were considered, 5 g/l, 10 g/l, and 20 g/l. Also, for all series, three different jet heights  $H$  equal to 0.25 m, 0.5 m and 1 m from the bottom were repeated for all ( $SSC_0$ ), hence in a total of 18 experimental scenarios were designed and reported as in Table 3-2. Details of how experiments were designed can be seen in Table 3-3. For simplicity reasons, experiments with a flat bottom surface ( $0^\circ$ ) and  $10^\circ$  slope is named experimental Series A and Series B respectively.

Table 3-2 Experiments scenarios

Exp #	Exp Serie A	Exp #	Exp Serie B	$\Delta H$ [m]	SSC [g/l]	H/D [-]
1	$0^\circ$	10	$10^\circ$	0.25	5	25
2	$0^\circ$	11	$10^\circ$	0.50	5	50
3	$0^\circ$	12	$10^\circ$	1.00	5	100
4	$0^\circ$	13	$10^\circ$	0.25	10	25
5	$0^\circ$	14	$10^\circ$	0.50	10	50
6	$0^\circ$	15	$10^\circ$	1.00	10	100
7	$0^\circ$	16	$10^\circ$	0.25	20	25
8	$0^\circ$	17	$10^\circ$	0.50	20	50
9	$0^\circ$	18	$10^\circ$	1.00	20	100

Based on experimental scenarios shown in Table 3-2, in the following chapters experiments will be named based on the slope  $S$  [degrees], the discharge height  $H$  in [cm] and the initial suspended concentration  $SSC_0$  in [g/l]. As an example, also in Table 3-3 Exp10 100 20 was named as an experiment with a slope of 10 degrees, 100 cm pipe discharge height and an initial suspended sediment concentration of 20 g/l. Exp 00 050 10 stands for an experiment with a slope of 0 degrees, 50cm pipe discharge height and an initial suspended sediment concentration of 10g/l. Note that the same experimental conditions for flatbed were repeated for 10 degrees slope.

### 3.7. Experiments conditions

A total of eighteen experiments were planned to be conducted with scenarios given in Table 3-2. When turbulent negatively buoyant plumes are discharged into a still ambient water of relatively lower density, the plume in the zone of established flow depends on the initial orifice densimetric Froude number  $F_{r0}$  (Equation (2-8), and the momentum jet length scale  $L_M$  (see Equation (2-11)).

Table 3-3 Experiments characteristics, parameter, and conditions

Experiment Exp. Slope,H,SSC <sub>0</sub>	H [m]	SSC <sub>0</sub> [g/l]	$\rho_0$ [-]	$g'_0$ [-]	$Q_{j0}$ [l/min]	$B_{j0}$ [m <sup>4</sup> /s <sup>3</sup> ]	$F_{rj0}$ [-]	$Re_{j0}$ [-]	$L_M$ [m]	$z^*/L_M$ [-]	Imp. regime
Exp 00 025 05	0.3	5	1003	0.0	5.6E-05	1.7E-06	40	7093	0.4	0.7	Jet-like
Exp 00 050 05	0.5	5	1003	0.0	5.6E-05	1.7E-06	40	7093	0.4	1.3	transitional
Exp 00 100 05	1.0	5	1003	0.0	5.6E-05	1.7E-06	40	7093	0.4	2.6	transitional
Exp 00 025 10	0.3	10	1006	0.1	5.6E-05	3.4E-06	29	7115	0.3	0.9	Jet-like
Exp 00 050 10	0.5	10	1006	0.1	5.6E-05	3.4E-06	29	7115	0.3	1.9	transitional
Exp 00 100 10	1.0	10	1006	0.1	5.6E-05	3.4E-06	29	7115	0.3	3.7	transitional
Exp 00 025 20	0.3	20	1012	0.1	5.6E-05	6.8E-06	20	7159	0.2	1.3	transitional
Exp 00 050 20	0.5	20	1012	0.1	5.6E-05	6.8E-06	20	7159	0.2	2.6	transitional
Exp 00 100 20	1.0	20	1012	0.1	5.6E-05	6.8E-06	20	7159	0.2	5.3	Plume-like

\* Experimental scenarios (characteristics, parameters, and conditions) were repeated on the 10 degrees sloped bed

When the plume enters the zone of boundary influence, the impingement conditions depend on the height of the orifice and the initial jet conditions, as well as the ambient water conditions. If the orifice

height is smaller than the momentum length scale, the impingement is characterized as jet-like impingement ( $z^*/L_M < 1$ ) otherwise as plume-like impingement when ( $z^*/L_M > 5$ ). Between the two limits, the impingement is in the transitional region. Based on the initial flow parameters in the proposed scenarios, the experimental conditions were calculated and reported in Table 3-3.

### 3.8. Measurement techniques

As explained earlier, a series of experiments have been performed to analyze the spreading of an impinging dense mixture, discharged as a jet at height  $H$  from the bottom. The bottom is represented by a table, above which measurements of SSC and vertical velocity profiles of the density current were measured. To measure the concentration of suspended particles in the plume, a FOSLIM optical silt measuring instrument was used, while the velocity profiles were measured with the use of a single point Acoustic Doppler velocimetry: Nortek 10 MHz Velocimeter. The measurement map is shown in the experimental setup in Figure 3-2. This figure shows several tubes which are installed from under the table to the surface. They were used to take fluid samples at each measurement location. At the end of the tubes outside the tank, they were connected to a valve where samples were taken and further analyzed with a high accuracy laboratory Turbidity meter (AL450T-IR).

On the table surface, a measurement map was made by dividing it into two sections. A longitudinal and central to the table axis was named x-axis. On this table, measurements were taken at locations shown on the map in Figure 3-3 from points  $P_1$  to  $P_9$ . During experiment series A, the discharge pipe was positioned above  $P_3$  which was considered as the impingement point. This point was chosen, as for the tests with a flat surface, the plume spreads radially; hence an IP at Point 3 gave enough space for the plume to spread with minimum reflection on the vertical walls. At the same time, enough distance of 2.5 m was provided to take measurements along the plume path.

It seemed interesting and necessary to compare measurements taken along the x-axis with lateral measurements along a perpendicular axis, y-axis which crosses the x-axis at the IP ( $P_3$  for tests with a flat bottom). As the plume was expected to flow downslope during Serie B (sloped bottom surface  $10^\circ$ ), the IP was moved from  $P_3$  to  $P_0$ . This means that the y-axis changed from crossing the longitudinal x-axis at  $P_3$  but at  $P_0$ . Y-axis measurement was renamed  $P_{10}$ ,  $P_{11}$ ,  $P_{12}$ , and  $P_{13}$ . This setup gave the opportunity to take a measurement for a long distance of 3.5m from  $P_0$  to  $P_9$  as well as along y-axis from  $P_0$  to  $P_{13}$  for a distance of 0.75 m from IP.

Not only in-situ measurement technics of the plumes spreading was used, but also images were taken by two cameras positions in front of the reservoir. Images taken were used to visualize the plumes spreading and its behavior by including the analysis of the density current front velocity and its position in time. The original idea was to add a fluorescent ink into the plume mixture and ultraviolet light to intensify the visibility of the plume and finally extract values of the SSC by extracting time-lapse images from the background image taken before the experiment. However, these technics did not work as the background ink concentration in the tank stacked after each experiment that influenced the following test. It would require emptying the tank for each test if we wanted to record videos for further analysis. In the following subsections, step by step, the techniques, and instrument working principals will be treated separately for each instrument.

#### 3.8.1. Flow velocity measurements

Acoustic Doppler velocimetry (ADV) method is an instrument designed and sold by Nortek Company to record instantaneous velocity components at a single-point with a relatively high frequency. Measurements are performed by measuring the velocity of particles in a remote sampling volume based upon the Doppler shift effect. Before the instrument is sold to a client, it is first tested and calibrated at the factory. Different parts of the ADV Components can be seen in Figure 3-6, for more details for working procedure, it is referred to read the ADV Nortek Velocimeter operations manual (Nortek, 2000). Due to its relatively high sampling rate (25-100 Hz) and the presence of fine sand particles acting as seeding make

the ADV one of the preferred equipment for measurements of turbulent flow, the case of the laboratory experiments in this research.

The vertical velocity profiles were measured in both x-axis ( $P_1, P_2, P_4, P_5, P_6, P_7$  and  $P_8$ ) and y-axis ( $P_{10}, P_{11}, P_{12}, P_{14}, P_{15}$ , and  $P_{16}$ ); points can be seen on the measurement map in Figure 3-3 and their coordinates x and y from IP are reported in Table 3-4.

Table 3-4 Measurement coordinates and locations from the impingement point (IP)

<b>Measured Points <math>P_i</math> on x-axis</b>	0	$P_1$	$P_2$	$P_3$	$P_4$	$P_5$	$P_6$	$P_7$	$P_8$	$P_9$
x- distance [m] from IP( slope= $0^0$ )	0	-0.90	-0.50	0(IP)	0.10	0.50	1.00	1.50	2.00	2.50
x- distance [m] from IP slope= $10^0$	0(IP)	0.10	0.50	0.90	1.20	1.50	2.00	2.50	3.00	3.50
<b>Measured Points <math>P_i</math> y-axis</b>				$P_3$ (IP)	$P_{14}$	$P_{15}$	$P_{16}$	$P_{17}$		
y- distance [m] from IP( slope= $0^0$ )				0	0.10	0.25	0.50	0.75		
<b>Measured Points <math>P_i</math> y-axis</b>	0(IP)	$P_{10}$	$P_{11}$	$P_{12}$	$P_{13}$					
y- distance [m] from IP( slope= $10^0$ )	0	0.10	0.25	0.50	0.75					
<b>Measured z-axis [mm]</b>	1; 3; 5; 7; 9; 10 ;15; 20; 25;30 ;35 ; 40; 50; 60 ( same for all Point $P_i$ )									

The velocity at Points  $P_9$  and  $P_{17}$  were not measured because their locations were too close to the wall and hence the wall influenced the measurements due to the reflection of the current at the vertical wall. Also, at location  $P_9$  which was far from the IP, the sensor was not accurate enough due to a lack of enough scattering strength as the concentration of the particles suspended in the water was too low and also the flow velocity was very low, close to zero.

To produce a vertical velocity profile at each point with a single point ADV, a total of 13 to 20 elevations heights ( $z=2,3,4,5,6,7,8,9,10,15,20,25,30,35,40,50,60$  mm) were taken by moving the probe height with a precision in the order of 1 mm.

The measurement of all z combined into one velocity profile at location P and was marked as 1 test that took 30-40 min to complete. Afterward; the experiment was restarted again by first cleaning the sediment that was deposited on the table with an underwater vacuum cleaner. The instrument was moved to another location for the next test. It was required to wait for 1 hour for the water in the reservoir to stabilize before the next test.

The velocity profile measurement (1 test of 40min) procedure started by positioning the probe in a known height on the vertical axis above the required measurement point. Before the start of the jet pump, for each velocity profile, the ADV sensor was used to check the clarity and stability of still water in the reservoir by measuring if there were no background motions of the ambient water. This was named "background measurement". The background measurement was taken at height  $z=15$  mm from the bottom and took 70 seconds. Height  $z=15$ mm was chosen because the peak velocity of the density current was noticed to be located in this vicinity most of the time.

After the background measurement, the jet pump was started and at the same time starting a new measurement was started; this was named "steady state measurement". The purpose of the steady-state measurement was to monitor the density current development and detect when and if a steady state was reached before the start of the actual measurement. This steady state measurement took 5 minutes, and during this measurement, it was possible to monitor the flow profile at the probe location.

For an output, for example, ADV profile Figure 3-7 for Exp 00 100 20, such profile could be seen on a computer screen during the experiments. In this figure, it clear how during the background measurement, the velocity profile was noisy with 0 cm/s as an average (no motion and still water) and due to a low signal to noise ratio, indicating no suspended particles for scattering. The same is observed during the steady state measurement until the density current reaches the position of the NDV probe. For this example, it took 142 seconds for the plume to reach  $P_6$  that was 1m from the impingement point. During the first 142

seconds, the signal to noise ratio was low (<5 dB) and increased as the plumes arrived and stayed stable. The time a steady state was reached depends on how far the measurement was located from the IP. To obtain a vertical velocity profile at each point P, each elevation of z was measured for 60 seconds at 15 Hz (~1000 samples) during which a profile as in the example in Figure 3-7(c) was obtained and then averaged to obtain the time-averaged velocity at an elevation z. The 60s time period was chosen as it was observed to be accurate enough and was in a good balance with the time available for 1 test in comparison with 30 s, 90s and 120s.

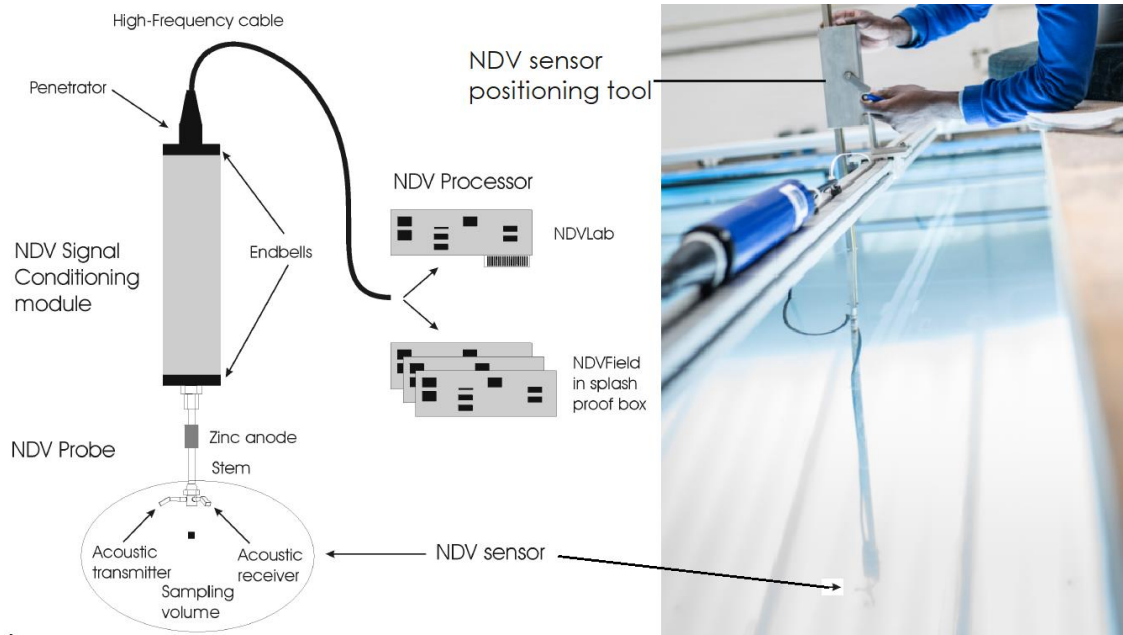


Figure 3-6 Different ADV component (left) and positioning of the probe during measurement (right).

The turbidity current flow velocity was measured with Acoustic Doppler velocimetry single point. Three Cartesian velocity components ( $u_x$ ;  $u_y$ ;  $u_z$ ) were measured above the table at locations shown in Figure 3-3 and coordinates reported in Table 3-4. For all point  $P_i$  in Figure 3-3, velocity components were measured for all  $z$  elevations to produce a velocity profiles results shown in Figure 6-11 .

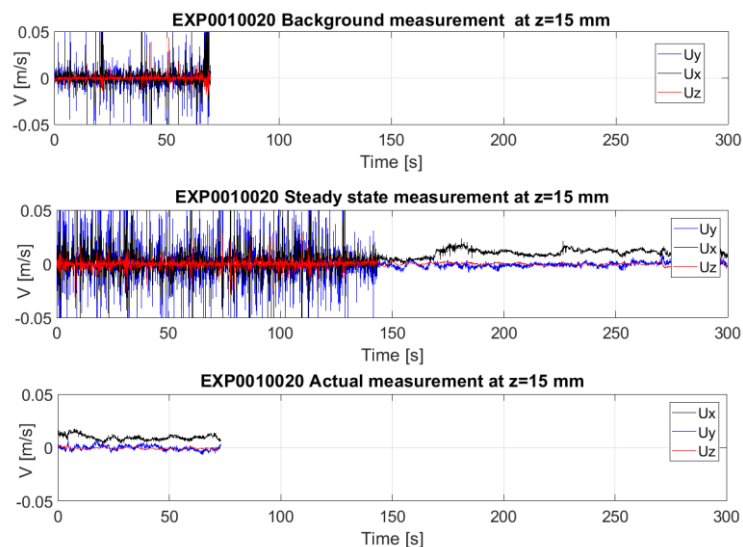


Figure 3-7 Exp 00 100 20: location  $P_6$  background (top), steady state (middle) and actual (bottom) measurements at elevation  $z=15$  mm.

ADV allows a maximum sampling frequency of 25 Hz. During the laboratory velocity measurement, at least 60 seconds sampling at a frequency of 25 Hz was done for all single points measured. A nominal

velocity range must be determined by the user of ADV. Nortek ADV has different velocity ranges that can be set by the operator before sampling in the "Main Menu" of the NDV data acquisition software. Choices are either +/- 3, 10, 30, 100 or 250 cm/s. During data acquisition, accurate measurements were achieved by setting the range closer to expected +/--maximum velocity. The accuracy on ADV velocity measurements taken by the ADV instruments is reported by Nortek to be equal to 0.5% +/- 1 mm/s and the sampling volume is always cylindrical, with a diameter of 6 mm. Also, it is recommended that when collecting raw data at 25Hz an SNR should be consistently above 15 dB. The SNR depends on the scattering strength and is determined by the concentration and size of the particles suspended in the water, hence, it was advantageous to use ADV during the laboratory experiments due to the use of sand powder to create the plume.

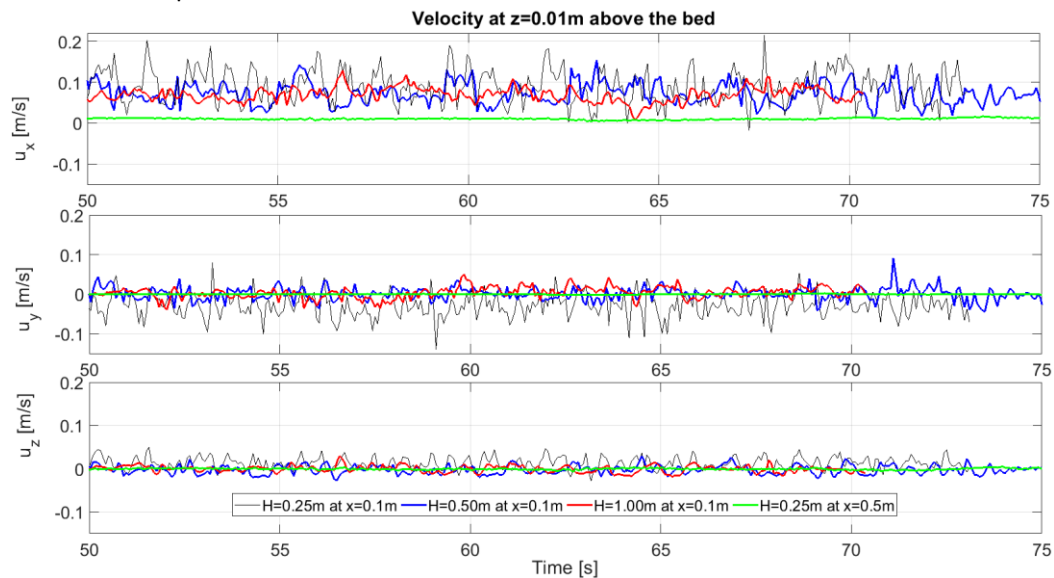


Figure 3-8. velocity time series measurement at  $z=0.01$  m above a flatbed.

### 3.8.2. Suspended sediment concentration measurement

To measure the concentration of suspended particles in the plume, two methods were considered. The first method measured the turbidity as local SSC by taking samples via tubes installed in the table that represent the seabed, with a high accuracy laboratory Turbidity meter AL450T-IR by which turbidity values were obtained as NTU value. The second method was a direct single point turbidity measurement with optical silt measuring instrument called "TurbiDirect FOSLIM". It was possible with the use of the FOSLIM to produce vertical SSC profile in the same manner as it was done for the flow velocity measurement with the ADV at points P and elevations z.

#### A. Direct turbidity measurement of local near bed SSC with turbidity meter AL450T-IR

The turbidity meter AL450T-IR is an optical portable turbidity meter designed with the requirements of ISO 7027, for the determination of turbidity for water Quality with a measurement auto ranging over the range of 0.01 to 1100 NTU. The operating principles are based on positioning a transparent vial filled with the sample inside the instrument sample chamber. When the measuring button is pressed, an infrared LED (light emitting diode) with a wavelength of 860 nm is emitted immediately. The emitted light is reflected by turbidity in the sample. The scattered light will be detected at an angle of  $90^\circ$  by a photodiode. As an output, the sensor will show on the screen the NTU value. In order to minimize errors, the vials and caps should be cleaned inside thoroughly after each test to avoid interferences. The same goes for the outside. The outside of the vial must be clean, dry and wiped with a smooth cloth to remove fingerprints, dust or water drops. Details of the working principle of Turbidimeter AL450T-IR can be found on the manufacturer website "[www.aqualytic.com](http://www.aqualytic.com)".

Before the use of AL450T-IR it must be calibrated. The calibration procedure started by inverting, one at the time, the vials with T-CAL standards NTU (samples from the AL450T-IR manufacturer) <0.1 NTU, 20 NTU, 200 NTU and 800 NTU. After the instrument is calibrated, the next step is to convert the NTU into SSC in g/l. This was done by making laboratory samples (sediment-water mixture) starting with low and known concentration to higher concentration a calibration curve and conversion equation as shown in Figure 3-9 was obtained.

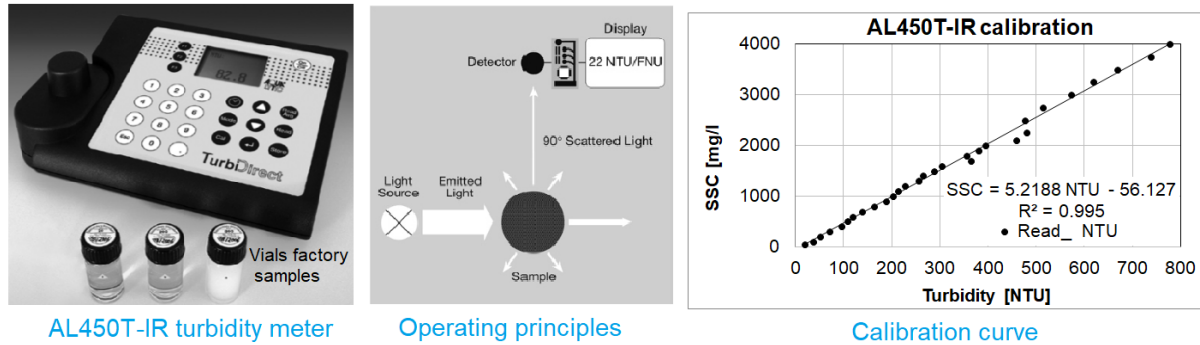


Figure 3-9 Turbidimeter AL450T-IR components, working principle, and a calibration curve.

To perform the local near bed suspended sediments concentration measurement, a separate test was done for only this purpose. After an experiment was started and a steady state is reached; one by one, the tube's end valve was open for 30 second in order to flush the tube clean. When the tube was cleaned, samples were taken for each point on the measurement map shown in Figure 3-3, starting by the tubes at the impingement point ( $x=0m$  distance from IP) towards the furthest Point P9.

The sample was kept in a 100 ml cup for each point until the experiment is ended. The samples for each cup were stirred to suspend the particles and put in 3 different vials that were measured with AL450T-IR 3 times each. This means that a measurement of point P was an average of nine measurements from three vials out of one 100 ml cup sampled at a single point.

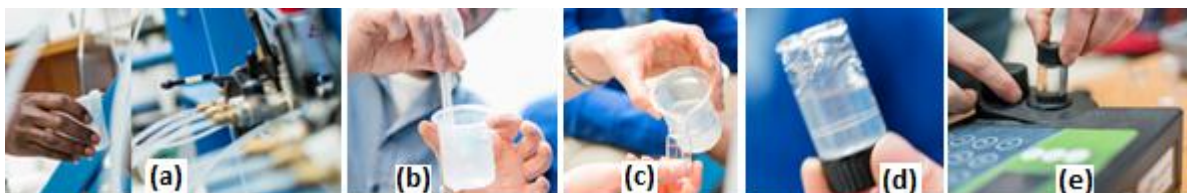


Figure 3-10 Steps for Turbidimeter AL450T-IR. (a): Sampling, (b): Mixing, (c): 3 vials sampling, (d): vial mixing and (e): NTU measurement.

Turbidity measurements were called local and near-bed SSC measurement because it was noticed that not only the water at the table surface was tapped via the tubes. Rather, when a valve was opened, turbid water from a column of about 20 mm above the bed was sucked into the tubes, this was confirmed by opening the tube P4 at the same time an ADV measurement above point P4 above was done and a vertical velocity profile as in Figure 3-11 was observed. For this reason, measurement taken by AL450T-IR sensor can only give the indications of a local averaged concentration rather than the near-bed SSC.

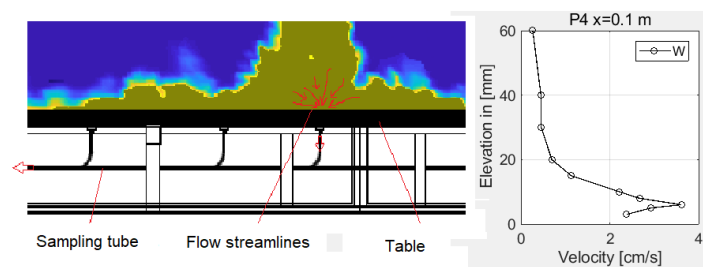


Figure 3-11. Flow streamlines and vertical velocity profile during turbid water sampling at P<sub>4</sub>.

## B. Foslím optical suspended sediment concentration measurement method

The FOSLIM is an optical measuring system to measure the suspended particles concentration in water with a measuring principle based on the attenuation of IR-light passing through the measuring volume. The light is absorbed and scattered on suspended silt particles. The FOSLIM system comprises a probe connected to a computer via fiber pair and with a computer program, the output is presented as an analog voltage.



Figure 3-12. FOSLIM components and a calibration curve.

The use of FOSLIM needs a re-calibration. The calibration procedure started by preparing a known volume of tap water placed in a bucket. The Foslím probes were submerged underwater inside the bucket and then via the control unit, it is possible to set the output voltage to zero volt which equals zero g/l for the initial SSC as minimum output. The next step is to mix the water with sediment to with highest expected SSC in g/l. Dilute the mixture to obtain values of SSC between zero volt and 10 volts. The procedure produces a calibration curve and conversion equation as shown in Figure 3-12.

The suspended sediment concentration measurements were taken at the same time and in the same manner as the velocity but at a different location. For example, the measurement of the SSC at  $P_3$  was done at the same time as the velocity at  $P_8$  and vice versa. The instrument was mounted on an elevation positioning tool that was also fixed on horizontal beams above the reservoir as shown in Figure 3-6. It is noted here that the SSC was measured at the same point P on the measuring map and elevations z as in the case of the density current flow velocity was taken for the SSC. During one test (one vertical profile), the background measurement of 70 seconds and steady state of 5 min were taken at the highest measured elevation  $z=60$  mm, followed by actual measurement for all height z to produce a single SSC profile. It is important to note that before each test, the FOSLIM probes needed to be cleaned with DEMI water to remove any turbid water on the probe surface. Otherwise, the emitted light would be attenuation and hence the output would be higher than expected.

### 3.8.3. Jet/plume and density current Video imaging

During the experiments, cameras were used to capture the negatively buoyant jet/plume impinging on the flatbed, and follow the development of the resulting turbidity density current over time. This part of the research was done with the help of an MSc student, S. Warringa for his Research Exercise as part of the master Offshore & Dredging Engineering. The goal was to analyze video recordings and extract time-averaged plume contour, dimensions, current front speed, and concentrations. To provide a homogeneous light source for the camera, particles in the flow should cause obscuration of the light.

To limit the daylight to get inside, the tank was fully darkened with a dark blanket as shown in Figure 3-13 in combination with a fluorescent ink and a UV-light technique to highlight the mixture. The ink was extracted from regular yellow STABILO highlighters which gave the best results with the use of the 100W LED UV spotlight. The UV light was mounted on the edge of the tank slightly to the left of the plume centreline, pointing downwards.

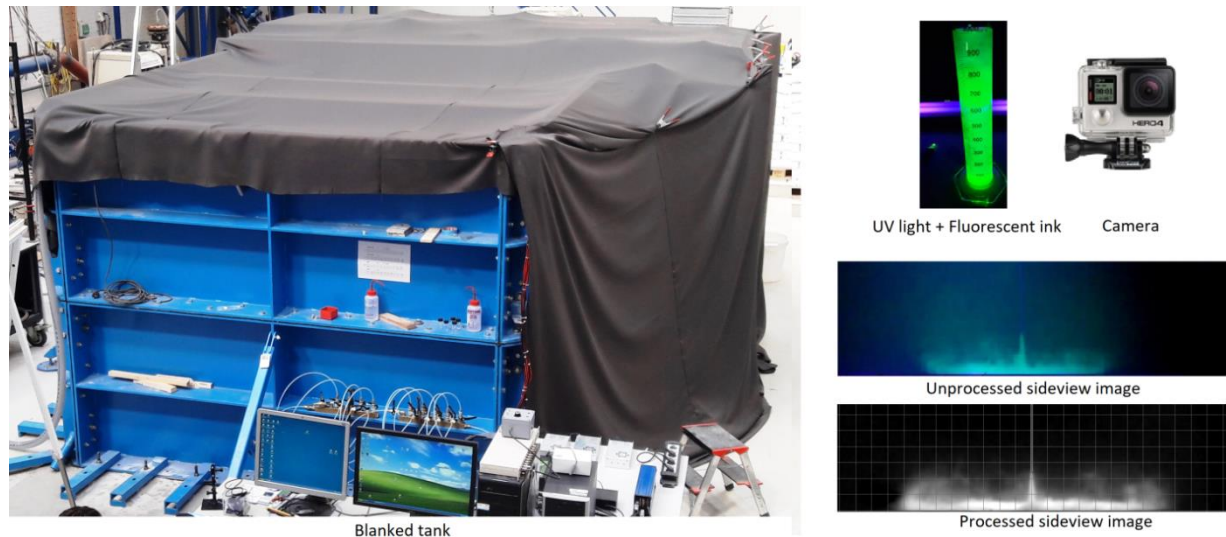


Figure 3-13. Darkened tank using curtains, fluorescent ink, camera and raw and its processed image.

Video recording was done using several cameras. A GoPro camera was mounted on top of the tank on a slider next to the jet pipe pointing downwards to create a top view. Furthermore, a regular household camera placed outside the tank filmed the side of the plume through a transparent tank window. The hope was that this could be a cheap and fast way to obtain the SSC from these images taken by a camera positioned outside the reservoir. This method worked fine for the first few tests. However, as more tests progressed, the fluoresce ink diffused and accumulated in the tank resulting in a bright background. As an effect, these techniques did not work to extract absolute values of the SSC due to the diffusion of the fluoresce ink that was used for visualization. Otherwise, the 23 m<sup>3</sup> tank reservoirs would need to be emptied after every single test which would be very time-consuming and a waste of water.

To separate the plume from its background, a straightforward method was used by taking an average image of 0.5 seconds from a video taken before the plume is visible. Videos were captured at 30 frames per second; therefore 15 frames were used to create this average image. The next steps followed by subtracting the time elapse imaging from the background image to obtain the averaged plume snapshot. The results from video analysis as reported in Chapter 5, included flow patterns, position and front velocity  $U_f$  of the density current and helped the researcher to compare the nine experiments conducted with a flatbed for various jet pipe heights and sediment concentrations.

### 3.9. Experimental method and procedure

The experimental scenarios proposed in section 3.6 were based on the initial bed slope for Serie A and Serie B with a bed slope of 0° and 10° respectively and were conducted in the same manner by changing the initial parameters. Each Experimental series was composed of nine experiments (3 different discharge orifice height  $H$  and three different initial SSC). To complete one experiment, several tests were conducted to produce all the velocity and SSC profiles at different locations on the measurement map shown in Figure 3-3. During one test two profiles (one for velocity and one for the SSC) are measured, at the same time, which took on an average 40 minutes to complete with single point ADV and single point Foslum instrument. Due to turbulent whorls structure and the entrainment of clean ambient water, a 60

seconds average was needed for accurate single point measurement. When one test was completed, the experiment was stopped and instruments were moved to different locations. The deposited sediment on the table was cleaned with a vacuum cleaner for the following test. After the modular tank was build and the bottom bed was put in place, activities of the laboratory experiments were systematically carried out following step by step as in the work plan below:

## Start

### Preparations

#### Step 1

- ✓ *Fill the modular tank (23 m<sup>3</sup>) of tap water. A fire hose present in the laboratory was used.*
- ✓ *Sediment preparation: Techniques explained in section **Error! Reference source not found.** ith the main activities to remove finer particles from the raw sediment, see Figure 3-4, dry filtered sediment in the oven for 8 hours and perform the sieve analysis to obtain a new PSD.*

#### Step 2

- ✓ *Prepare the water-sediment mixture in the reservoir of the required initial SSC.*

#### Step 3

- ✓ *Clean the bottom table with a submersible vacuum cleaner.*

#### Step 4

- ✓ *Cleaning, calibration, and positioning of the instruments.*

#### Step 5

- ✓ *Install the jet pipe at the required jet pipe elevation from the bottom table.*
- ✓ *Check the KATflow transducers alignment.*

### Video recording

#### Step 6

- ✓ *Adjust the camera settings to the required preferences.*
- ✓ *Fix the camera on the tripod.*
- ✓ *Install the UV-light.*
- ✓ *Cover the modular tank with the blackout curtains.*

#### Step 7

- ✓ *Start the mixing pump and wait until the water-sediment mixture is homogeneous.*

#### Step 8

- ✓ *Add fluorescent ink in the mixing tank.*

#### Step 9

- ✓ *Measure the temperature: modular tank (ambient water) and the plume mixture in the mixing tank.*

#### Step 10

- ✓ *Start the KATflow meter.*

#### Step 11

- ✓ *Start the camera recording.*

#### Step 12

- ✓ *Start the jet pump.*
- ✓ *Open carefully the jet valve and regulate the flow to uniform and constant flow rate with KATflow meter, in this experiment 3.3 l/min.*
- ✓ *Keep the plume mixture temperature constant (should be the same in the tank as in the reservoir): Add ice (and sediments) to cool down due to the mixing pump heat emission.*

#### Step 13

- ✓ *Record the Experiment until steady state is reached.*
- ✓ *Stop the camera recording.*

#### Step 14

- ✓ *Stop the jet pump.*
- ✓ *Close the jet valve.*
- ✓ *Stop the KATflow meter.*

- ✓ Stop the mixing pump.

#### **End of Video recording session**

#### **Local turbidity measurement**

##### **Step 15**

- ✓ Repeat step 2,
- ✓ Repeat step 3
- ✓ Repeat step 4
- ✓ Repeat step 5
- ✓ Repeat step 7
- ✓ Repeat step 9
- ✓ Repeat step 10
- ✓ Repeat step 12

##### **Step 16**

- ✓ Sample from the tubes 100 ml for each P locations on measurement map Figure 3-3 starting from points closer to IP (impingement point). Points of equal distance from IP in x-axis and y-axis should be sampled simultaneously.

##### **Step 17**

- ✓ Repeat step 14,

##### **Step 18**

- ✓ Resample three vials for each sample in step 16 above
- ✓ Follow the procedure in Figure 3-10 for the local turbidity measurements

#### **End of local turbidity measurements**

#### **Density current Velocity and SSC measurement**

##### **Step 19**

- ✓ Clean the instruments probes
- ✓ Position the instrument above the next measurement location ( $P_1$  points)
- ✓ Wait 60 minutes for the ambient water stabilization, no motion.

##### **Step 20**

- ✓ Repeat step 15.

##### **Step 21**

- ✓ Take the calibration measurements

##### **Step 22**

- ✓ Start the steady state measurement at  $z=15$  mm for the ADV and  $z=60$  for the Foslum
- ✓ Start single point measurement for elevations  $z$  from up ( $z=60$  mm from the bottom) towards the bottom table (1 mm from the bottom)
- ✓ End of Density current Velocity and SSC measurement.

**End**

## CHAPTER 4

# CFD LES simulations of the Near Field spreading of the deep-sea mining return plumes

---

In this chapter, the CFD LES model used to simulate Near Field spreading of the DSM return plume and mixing with the ambient water is introduced. The equations being solved are given with the associated boundary conditions. Other important details are also provided such on the numerical model type, discretization, and model setup and among others.

### 4.1. CFD model introduction

To predict the environmental impacts of deep-sea mining return discharge plumes disposed of as waste released as a negatively buoyant jet via a vertical pipe, a numerical model tool is needed. The model simulates the flow mixing with the ambient deep-sea water as well as the interactions with seabed topography. To validate such a numerical model, laboratory experiments are needed. At the end of experimental work reported in Chapter 4, a validated three-dimensional CFD LES model called TUDflow3D was used as a tool to simulate the same conditions as in the laboratory to be able to compare both results. TUDflow3d is a three-dimensional numerical model that uses the finite volume method and Large Eddy Simulation (LES) to solve the Navier-Stokes equations on a staggered grid shown as an example in Figure 4-3. Detailed description of TUDflow3D can be read in De Wit ( 2015).

### 4.2. Model description

The flow in a negatively buoyant jet as observed in the laboratory is highly turbulent and intermittent hence to capture the individual unsteady turbulent eddies in the discharged jet/plume, an LES model was chosen above DNS (Direct Numerical Simulation) and RANS (Reynolds Averaged Navier Stokes). In DNS, all turbulent scales from the largest ones to the smallest Kolmogorov scales are solved on the grid and no separate turbulence model is used hence in DNS fine grids are required which makes it not applicable for a practical problem such as in this case DSM plume disposed as jet with a high Reynolds number and a large computational domain. On the other hand, in RANS all turbulent scales are modeled by a turbulence model and individual unsteady turbulent eddies in a return discharge plume are filtered away. To realize the general objectives of this research especially the aim stated in section 1.5, TUDflow3D CFD LES numerical model was applied.

TUDflow3D model gives the possibility to be used as a tool to extend experimental results to natural cases to better understand in a better way the processes governing the spreading and mixing of DSM plumes providing insights and support for the acceptance criteria of the environmental impacts from DSM activities. In this research, necessary simulations with reasonable accuracy were done. However, according to available data and time allocation for MSc thesis, a full-scale 3D is more computationally times demanding, hence, no field scale simulations were done. Only the laboratory experiments were

reproduced in the model in addition to one simulation that included the effect of a near-bottom uniform current of 0.10 cm/s which have been observed as an average in the field.

TUDflow3D model was developed by De Wit, 2015 during his Ph.D. research carried out as part of the Building with Nature innovation program (2008-2012). Throughout this chapter, we shortly introduce equations being solved in the computation. The most relevant features of TUDflow3D model, the model setup, the boundary conditions and performed scenarios are given here. For more documentation on TUDflow3d model, it is recommended to the interested readers to read “3D CFD modeling of overflow dredging plumes” the Ph.D. report of De Wit, 2015.

### 4.3. TUDflow3D governing equations

The Near Field “TUDflow3d” CFD model is a three dimensional LES non-hydrostatic solver. The model solves Navier Stokes Equations (4-1) and (4-2), with variable density equation (4-4) which is derived from the contribution of all sediment volume fractions  $C_i$  in the mixture.

$$\frac{\partial p}{\partial t} + \nabla \cdot (\rho u) = 0, \quad (4-1)$$

$$\frac{\partial \rho u}{\partial t} + \nabla \cdot (\rho u u) + \nabla \cdot P - \nabla \cdot \tau = F, \quad (4-2)$$

Where  $\rho$  is the density,  $u$  is the flow velocity vector,  $t$  is time,  $p$  is the pressure,  $\tau$  is a shear stress tensor and  $F = [0, 0, (\rho - \rho_c)gz]$  is the body force caused by gravitation.

In TUDflow3d model, the pressure  $P$  is the excess pressure over hydrostatic pressure as it corrected for the hydrostatic pressure balance in the vertical direction, Equation (4-3). The variable density  $\rho$  is derived from the contribution of all volume fractions  $C_i$  in the mixture given by Equation (4-4)

$$\frac{\partial P}{\partial z} = \rho_c gz, \quad (4-3)$$

$$\rho = \rho_c + \sum_{i=1}^n C_i (\rho_i - \rho_c), \quad (4-4)$$

In which,  $\rho$  is the local mixture density at the grid.  $C_i$  and  $\rho_i$  are the volume concentration and density of each individual fraction while and  $\rho_c$  is the density of the carrier fluid, in this research case water  $\rho_c = 1000 \text{ kg} / \text{m}^3$ .  $n$  is the number of sediments fractions.

The hindered Settling velocity is incorporated in the model based on the particle diameter for non-cohesive sediment fractions following the approach introduced in section 2.5.1 as it was first proposed by Richardson-Zaki. The Sediment used in the laboratory experiments was poorly graded and no flocs formation was observed, hence it was not necessary to used different sediment fractions in the model which made the simulation time much shorter with good results.

### 4.4. Plume and density current interactions with the bed

It was observed in the laboratory experiments the plume interaction with the bed was dominated by deposition. This was mainly to that only settling particles were used and the flow velocities at the bed were too small and hence below critical erosion criteria. Also, bed was represented by a smooth table with no initial sediment available at the bed to be picked up. The application of the shear stress on the bed, which is a solid wall is treated in boundary conditions section 4.7. In TUDflow3D, the sediment deposition is calculated by Equation (2-36) in the first computational cell above the bed. The deposition

amount is added each time step in the lowest grid cell; hence the total cumulative amount of deposition in the bed is also tracked to be able to show deposition amounts and locations.

## 4.5. Modeling of turbulence in TUDflow3D

In order to include the influence of turbulence in the Navier Stokes equations above, the shear stress tensor is introduced as in Equation (4-5). The stress tensor contains the eddy viscosity, which is a contribution of the molecular viscosity  $\nu_{mol}$  and turbulent viscosity  $\nu_t$ .

$$\tau = \rho \nu_e \left\{ \nabla u + \nabla \cdot (u)^T - \frac{2}{3} \nabla \cdot u \right\}, \quad (4-5)$$

In which the eddy viscosity  $\nu_e = \nu_{mol} + \nu_t$ . TUDflow3d is an LES model; hence, the larger turbulent scales which possess the major part of the turbulent energy are solved on the grid while turbulent scales which are smaller than the grid size is modeled by a turbulence model. In this approach, a spatial filter equal to the grid size is applied to the flow field and the contribution from smaller than grid scales is determined by a sub-grid-scale model. In the present simulations, the Dynamic Smagorinsky sgs model was used.

$$\nu_t = \nu_{sgs} = (C_s \Delta l)^2 \sqrt{2 S_{ij} S_{ij}} \quad (4-6)$$

Where  $C_s$  is the constant in the subgrid-scale model,  $S$  is a function  $\nabla u$  resolved rate of strain tensor and  $\Delta l$  the width of the grid filter which is proportional to the smallest resolvable length scale of the discretization. The optimum value of  $C_s$  varies from flow to flow and its value should be reduced near solid walls to reduce the amount of dissipation introduced by the Smagorinsky sgs model. In this study the value  $C_s=0.325$  was adopted which corresponds to the often used value  $C_s=0.1$  for the often used Smagorinsky sub-grid-scale model equation (4-6) (De Wit, 2015).

An alternative to this approach is the WALE model, which has an advantage over Smagorinsky model, to be faster. However, although they were tedious simulations; in comparison to laboratory experiments, better results were obtained with DSmag turbulent model.

## 4.6. CFD model set-up

### 4.6.1. General setup

The numerical model setup was based on the experimental setup and each plume release scenario and locations Table 3-3 was duplicated in LES model. However, to implement a 2 m modular tank water depth domain as in the laboratory test, shown Figure 3-2, it is unfeasible as it would cost too large CPU demand to achieve a reasonable grid resolution. A solution was chosen to divide the model into two parts as shown in Figure 4-1. In this figure, the left image shows an overview of how the two model is linked, the center image shows a full domain simulated with TUDflow3D while the right image shows a simulation with TUDflow3D but receiving inputs values from JETPLUME at a distance  $H^*$  from the source.

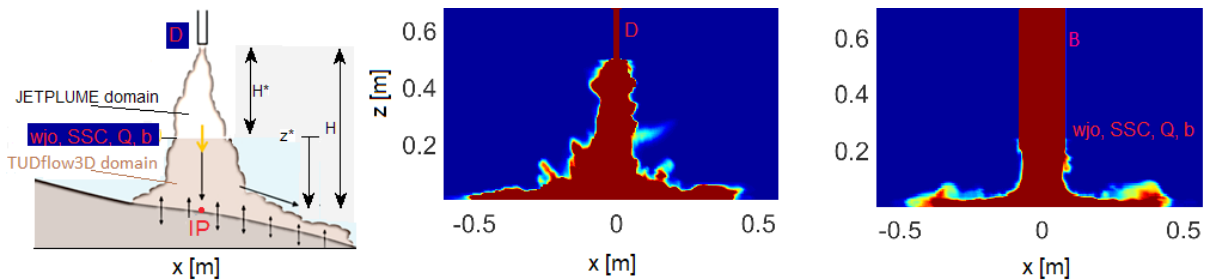


Figure 4-1 TUDflow3D domain and buoyant jet integral model JETPLUME domain ( Exp 00 050 20).

The first upper zone next to the release pipe is simulated by the jet integral model JETPLUME (Lee and Chu 2003). This application is relevant because in this zone jet/plume behavior are dominant and JETPLUME model is a quick and accurate way to model this. JETPLUME model simulations with input variables as in the laboratory tests generate top-hat profiles for the initial dilution; new plume diameter  $b$  new suspended sediment concentration  $SSC$ , new volume flux  $Q$  and new velocity  $w_j$ , which are at this end used as inputs in the detailed LES near bed model. The governing equations for top-hat approximations were introduced in Chapter 2. JETPLUME covered the zone  $z=0.25-1m$  for a release at  $1m$ ,  $z=0.15-0.5m$  for a release at  $0.5m$  and  $z=0.1-0.25m$  for a release at  $0.25m$ . As results LES model had a larger input diameter  $b$  which gave a possible to achieve the requirement of 10 grid cells over the jet diameter at the outflow. Figure 4-1 shows a comparison of 2D plots resulted from a full domain simulated entirely with LES with an input pipe diameter  $D=10mm$  (center image in Figure 4-1) and an LES simulation with large diameter  $B$  (left image in Figure 4-1) implemented in the model input as plume half-width  $b=42mm$  (value for Exp 00 050 20). The value of  $b$  is obtained from JETPLUME outputs. The division of the domain into two parts reduced the simulation by a factor of 10.

#### 4.6.2. JETPLUME

In this research, JETPLUME was used as a buoyant jet integral model to simulate the closer part of the jet release as shown in Figure 4-1. The JETPLUME inputs were considered to be exactly the same as in the laboratory experiment. JETPLUME model uses Lagrangian tracking of initial plume slices which move and dilute under influence of its initial momentum and buoyancy and ambient velocity. The model has been applied to both laboratory and field scale and it was found to be an accurate representation of mixing of plumes and jets (Lee and Chu, 2003). JETPLUME model does not account for the particle settling velocity. However, this was not a problem because within the distance  $z$  close to the release for which JETPLUME simulates inputs variables for TUDflow3D model, in this domain the settling velocity is negligible as pipe jet velocities are a magnitude larger than sediment settling velocity.

#### 4.7. LES model boundary conditions

To model the flow observed in the laboratory experiment in a three-dimensional domain similar to the laboratory experimental conditions shown in Figure 3-2, the LES model setup is shown in Figure 4-1 was build and different boundary conditions were treated as the following:

Table 4-1 LES model input parameters

Experiment	$H$ [m]	$SSC_0$ [g/l]	$H^*$ [m]	$z^*$ [m]	$b$ [m]	$w_j$ [m/s]	$S$ [-]	$Q_{in}$ [m <sup>3</sup> /s]	$C$ [v%]	$L_M$ [m]	$z^*/L_M$ [-]	Jet/plume regime
Exp002505	0.25	5	0.15	0.10	0.016	0.22	3	1.69E-04	6.21E-04	0.38	0.39	Pure jet
Exp005005	0.50	5	0.40	0.10	0.042	0.08	8	4.50E-04	2.33E-04	0.38	1.05	Transition
Exp010005	1.00	5	0.75	0.25	0.079	0.03	10	5.70E-04	1.84E-04	0.38	1.97	Transition
Exp002510	0.25	10	0.15	0.10	0.016	0.22	3	1.69E-04	1.20E-03	0.27	0.56	Pure jet
Exp005010	0.50	10	0.40	0.10	0.042	0.08	8	4.50E-04	4.66E-04	0.27	1.49	Transition
Exp0010010	1.00	10	0.75	0.25	0.079	0.04	13	7.21E-04	2.91E-04	0.27	2.78	Transition
Exp002520	0.25	20	0.15	0.10	0.016	0.22	3	1.69E-04	2.50E-03	0.19	0.79	Pure jet
Exp0005020	0.50	20	0.40	0.10	0.042	0.08	8	4.50E-04	9.32E-04	0.19	2.10	Transition
Exp0010020	1.00	20	0.75	0.25	0.079	0.05	17	9.56E-04	4.38E-04	0.19	3.94	Transition

$H^*$  is JETPLUME domain distance from release elevation.  $z^*$ = TUDflow3D release elevation from the bed

##### 4.7.1. Inflow and outflow

TUDflow3D simulations as shown Figure 4-1 (right image), the pipe inflow boundary comprises constant parameters and volume fractions as reported in Table 4-1 are obtained from top-hat approximation for buoyant jet inflow. First JETPLUME simulates Gaussian profile shown in Figure 4-2 and then the top-hat approximation is applied to obtain constants as average values using the technique shown in 2.2.8 in literature, see also Figure 2-4. Constant flow parameters in Table 4-1 depends on the initial plume releases conditions. At the release point, a constant pipe average velocity  $w_{j0}=0.7m/s$ . Due to the entrainment process of the ambient water, the jet thickness increases and spreads linearly hence varying

both jet momentum and buoyancy leading to different LES model input parameters in Table 4-1. For a Cartesian box simulation with horizontal grids as shown in Figure 4-3, both lateral wall boundaries are no inflow boundaries, they are treated as non-slip wall boundary condition. To have the mass balance in the TUDflow3D simulation domain correct, outflow boundary conditions are applied near the water surface where the same amount as the input of water volume flux is extracted out of the domain.

#### 4.7.2. The free surface

During the experiments, for all runs the pipe orifice was needed to be submerged deep enough so that the entrainment of the ambient water does not reach the free surface of the domain, hence deep water conditions promising no water surface gradients. In TUDflow3D, this was achieved with the approach of free-slip conditions apply by using a rigid lid on the free surface of the model domain.

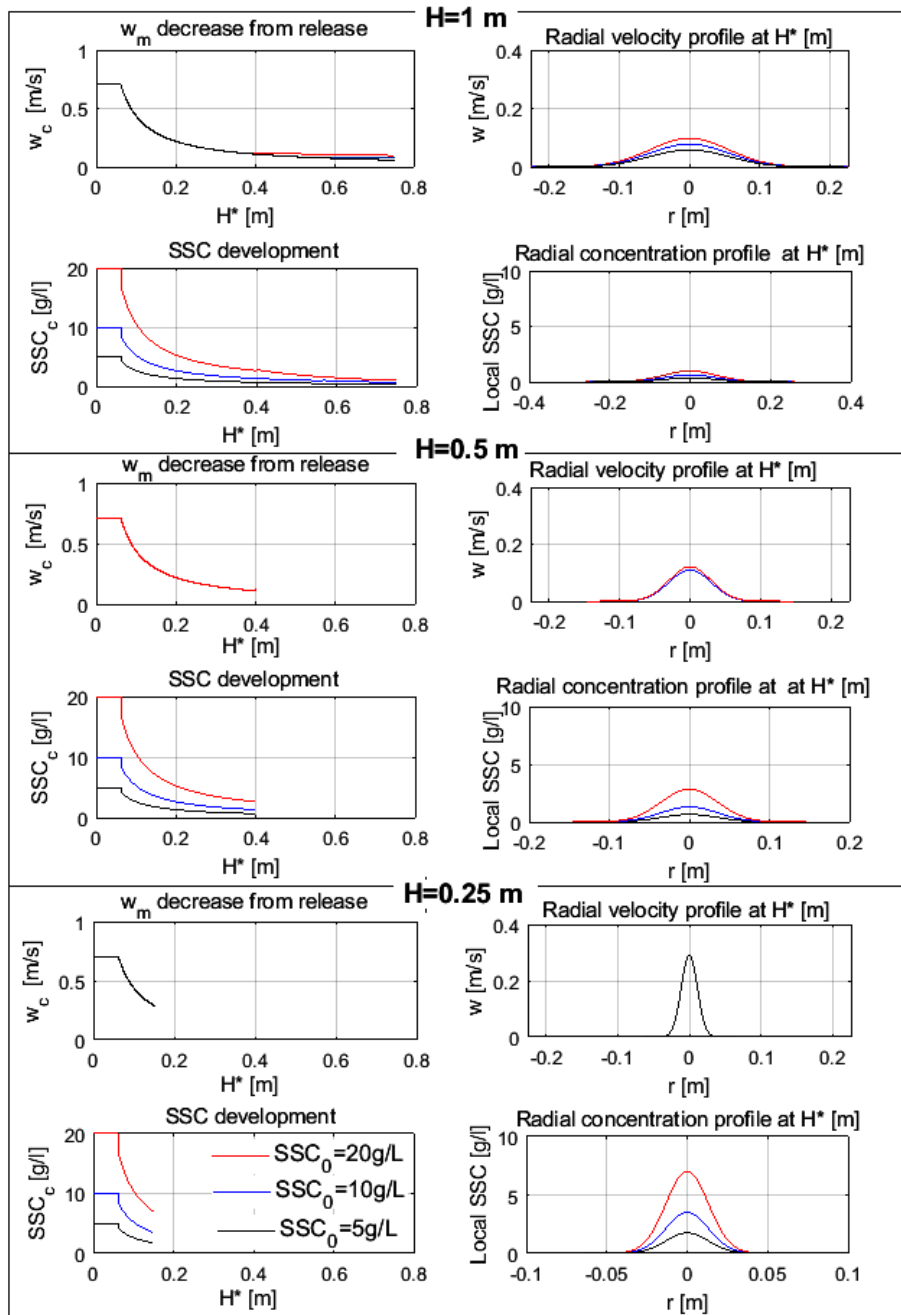


Figure 4-2 JETPLUME simulation for TUDflow3D boundary inputs.

### 4.7.3. Bottom solid wall

Both the bottom surface and sides of the modular tank used for the experiment are made of solid walls. At these boundaries, a wall function is used to apply the shear stress Equation (4-7).

$$\tau_n = \rho u_* u_n, \quad (4-7)$$

$$u_n = \sqrt{u^2 + v^2}, \quad (4-8)$$

Where  $u_*$  is friction velocity produced by the wall parallel velocity Equation

(4-8) in the first grid cell at a distance  $z_n = \Delta z/2$  from the wall. For hydraulic smooth walls which were the case in this research, the following standard laws of the wall with a logarithmic layer, the buffer layer, and viscous sub-layer were used:

$$\begin{aligned} u_n^+ &= z_n^+ \text{ for } z_n^+ \leq 5 \\ u_n^+ &= 5 \ln z_n^+ - 3.05 \text{ for } 5 \leq z_n^+ < 30 \\ u_n^+ &= 2.5 \ln z_n^+ + 5.5 \text{ for } z_n^+ \geq 30 \end{aligned} \quad (4-9)$$

Where  $u_n^+ = \frac{u_n}{u_*}$  and  $z_n^+ = \frac{u_* z_n}{\nu}$ .

## 4.8. Discretization schemes

One of the most important choices when using an LES model is the choice for the momentum advection scheme (De Wit, 2015). In TUDflow3D, there are several discretization schemes alternatives. For this study for LES simulations, a stable advection discretization was needed. The sixth-order hybrid difference scheme (HYB6) was used as it was found to be stable, energy consistent and effective to remove wiggles while at the same time little numerical dissipation was required to achieve stable turbulent results. For diffusion term, a second-order central difference scheme (CDS2) numerical scheme was used in the momentum equations. A different analysis of the advection and diffusion schemes as implemented in TUDflow3D can be found in and their modifications can be read in De Wit, 2015.

## 4.9. Grids construction

To replicate similarly the laboratory experiments with an LES model as much as possible, care for the model set-up is needed in order to comply with stringent demands of the three-dimensional features for turbulence phenomena present in the flow. To simulate DSM return plumes on the same scale as in the laboratory experiments, simulations are carried out on a Cartesian coordinate system  $x, y, z$  with rectangular-shaped grids as shown in Figure 4-3. The grid is equidistant in  $z$  direction and variable in  $x$  and  $y$  directions. This technique allows the use of structured solver that in general is faster than in the case of an unstructured grid.

To obtain accurate results using TUDflow3d LES model, a reasonably accurate LES of a buoyant jet requires that the base grid resolution must be at least of 10 grid cells over the jet diameter at the outflow. For this reason, in this research, at the plume outflow, the equidistant vertical grid size was chosen to be  $\Delta z = 0.1D = 1 \text{ mm}$ . The smallest horizontal grid size closer to the impingement point is  $\Delta x = 0.2D = 2 \text{ mm}$ . The lateral expansion of the grid in downstream direction follows the widening of the plume leading to an efficient distribution of the grid points. The effective lateral grid size  $\Delta y = 2 \text{ mm}$  at the outflow expands further downstream of the turbidity current.

The model grip setup in this research lead to *6–24 millions* of grid cells for a zone up to  $x \approx 5 \text{ m}$  long shown in Figure 4-3. The variability of the number of grids depends on the techniques explained in section 4.7.1 used to reduce the size of the computation domain. Figure 4-3 has the same dimensions of the table

used during the laboratory test to mimic the sea-bed and shows a 2D horizontal replication of table shown in Figure 3-3 and the LES results are presented in a Cartesian  $x, y, z$  coordinate.

### 4.10. Bathymetry

In both laboratory experiments and CFD, the bed bathymetry was simplified by using a table with a smooth surface by which the slope could be changed to 10 degrees for experiments Serie B. Two different bed slopes that have implemented can be seen in Figure 4-3. The left side shows the setup for a flat table and the grids used in CFD. At the end of experiments with a flat table, the slope was changed to 10 degrees. In LES model, a straightforward technique was used by using Matlab to change the bed slope to 10 degrees. In Figure 4-3, a deducted bathymetry for sloping bed and adapted grids are shown.

During experiments with a flat bottom, the release pipe was set above the table for all experiments; the pipe was located at 2 m from the left side of the modular tank, see Figure 4-3 (left). During experiments with 10 degrees sloped bed, in order to increase the measuring length from the impingement point, the pipe was mode 1 meter towards the left because the density current was expected to flow downslope, see Figure 4-3 (right). However, during experiments with 10 degrees slope and release height of 1 m, the water depth in the modular tank became insufficient to have pipe exit submerged enough preventing the entrainment of air from the free surface. In the numerical model, this was not necessary; the pipe position was kept the same for all Experimental serie B.

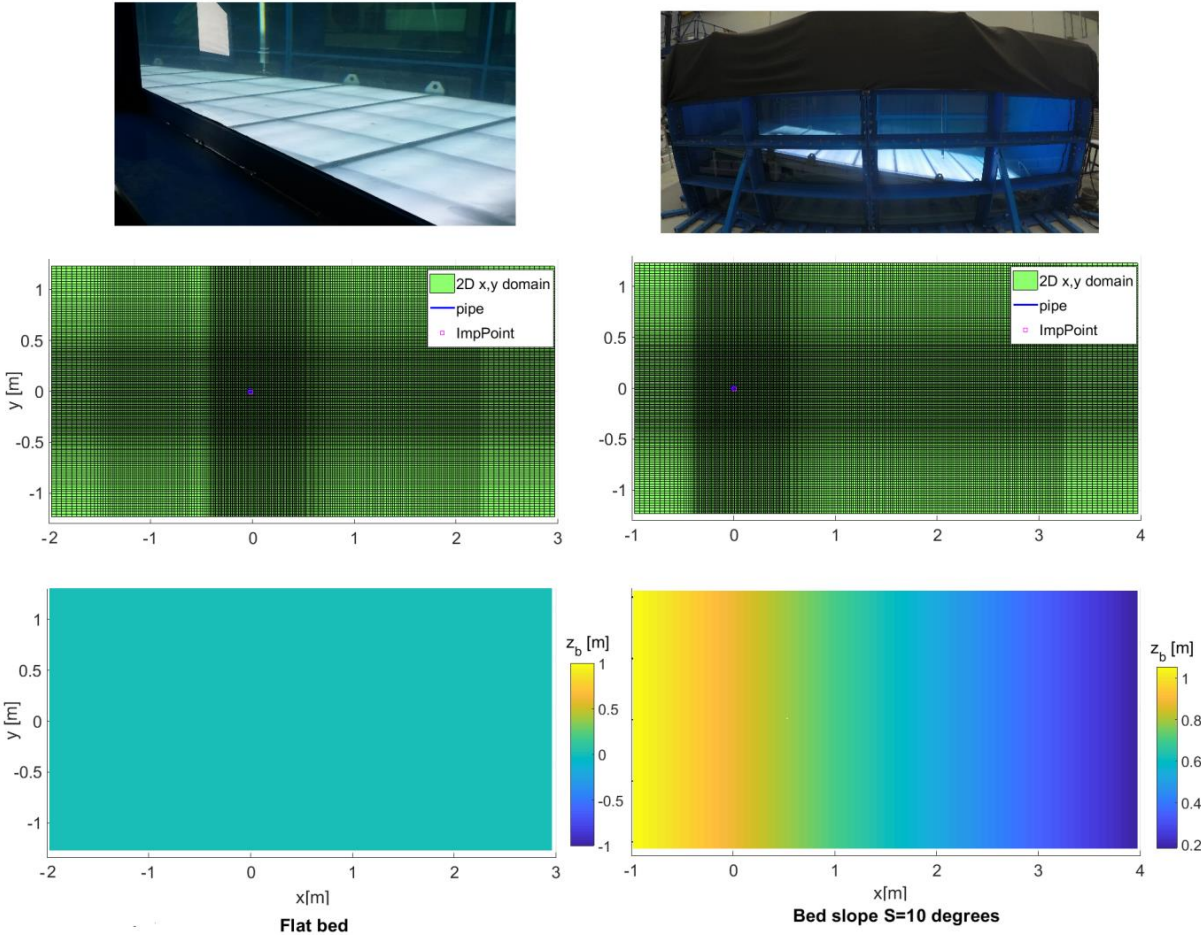


Figure 4-3 Used grid for simulating jet/plumes spreading and density current flows.

#### 4.11. Implemented of slope in TUDflow3D CFD model

The bed slope was implemented in TUDflow3Dflow with an Immersed Boundary Technique (IBT) with cut-cell method on staggered grid as the example shown in Figure 4-4. In this method, cells in the Cartesian grid that are cut by the IBT are identified and the intersection of the boundary with the sides of these cut-cells can be determined. In the following example shown in Figure 4-4, the zoomed in part on the right, the dark line which is inclined with an angle  $\theta$  with the horizontal, cut cells it crosses into two parts. Cells whose centers lie in the fluid (green cells Figure 4-4, bottom) in are considered as wet cells while cells whose centers lie in the solid are dry cells.

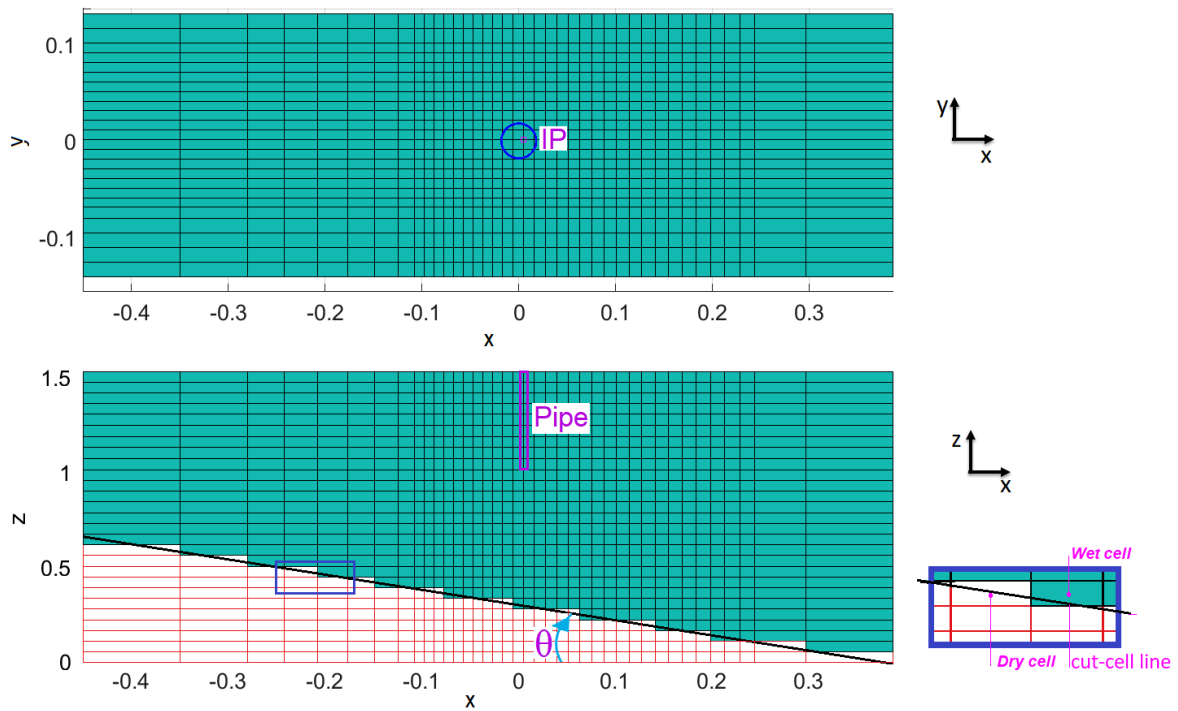


Figure 4-4 Used grid for simulating jet/plumes spreading and density current flows (Note that this is not the grids used during simulations done during this thesis. This is a zoomed to illustrate how a slope was implemented in TUDflow3D. The grid used is shown in Figure 4-3).

## CHAPTER 5

# Laboratory experiments results

---

One of the main goals of this research was to provide a dataset of flow velocities and SSC measured on an experimental scale of a negatively buoyant jet and plumes wastes returned back to the seabed. In this chapter, laboratory tests results are presented. Furthermore, some interesting observations about the impinging jet/plume are made.

### 5.1. Introduction

The flow velocities and the level of SSC measurements were carried out inside the turbidity current that is generated horizontally after the impingement of descending plumes. The experimental setup is a small scale and similar to what mining companies expect to happen in Near-Field region of 250 m long when DSM plumes wastes are returned back to the seabed. This distance was represented in the laboratory by 5 m long on a 1/50 scale compared to the field.

Previous chapters introduced the methodologies used in this research. In chapter 3, attention was made explaining the manner and conditions in which the laboratory experiments were carried out. Investigated processes included the turbid plumes spreading, their mixing and effects on several Near-Field processes such as the erosion and deposition of sediment particles raining out of offshore mining plumes. In Chapter 4, used CFD LES numerical model to simulate the laboratory experiments was introduced. In this chapter, observed important processes are given while the comparisons of the experimental measurements and LES simulation results will be given in Chapter 6.

In section 5.2, results obtained from the Video imaging technique are given. This technique has been used to qualitatively capture the flow patterns of the impinging negatively buoyant jets/plumes and the spreading of turbid currents flows. Laboratory Acoustic Flow velocity measurements of different jet source boundary conditions and their analysis will be given in section 5.3 while detailed analysis of Optical SSC measurements is treated in section 5.4.

The measurement data analysis included the effects on the turbid current due to changes in initial plume concentrations. Results obtained from the flow release from three different source heights relative to the bed are compared. Furthermore, the effects of a 10 degrees sloping bed are analyzed and compared with results obtained assuming the seabed to be flat. Throughout this chapter, systematically experimental results are given in the following sections. Figure 5-1 shows an overview of the experimental buoyant plume and turbid current after impingement on the bed. On flatbed, the plume spread radially while on a sloped bed, the plum is pulled in the downslope direction.

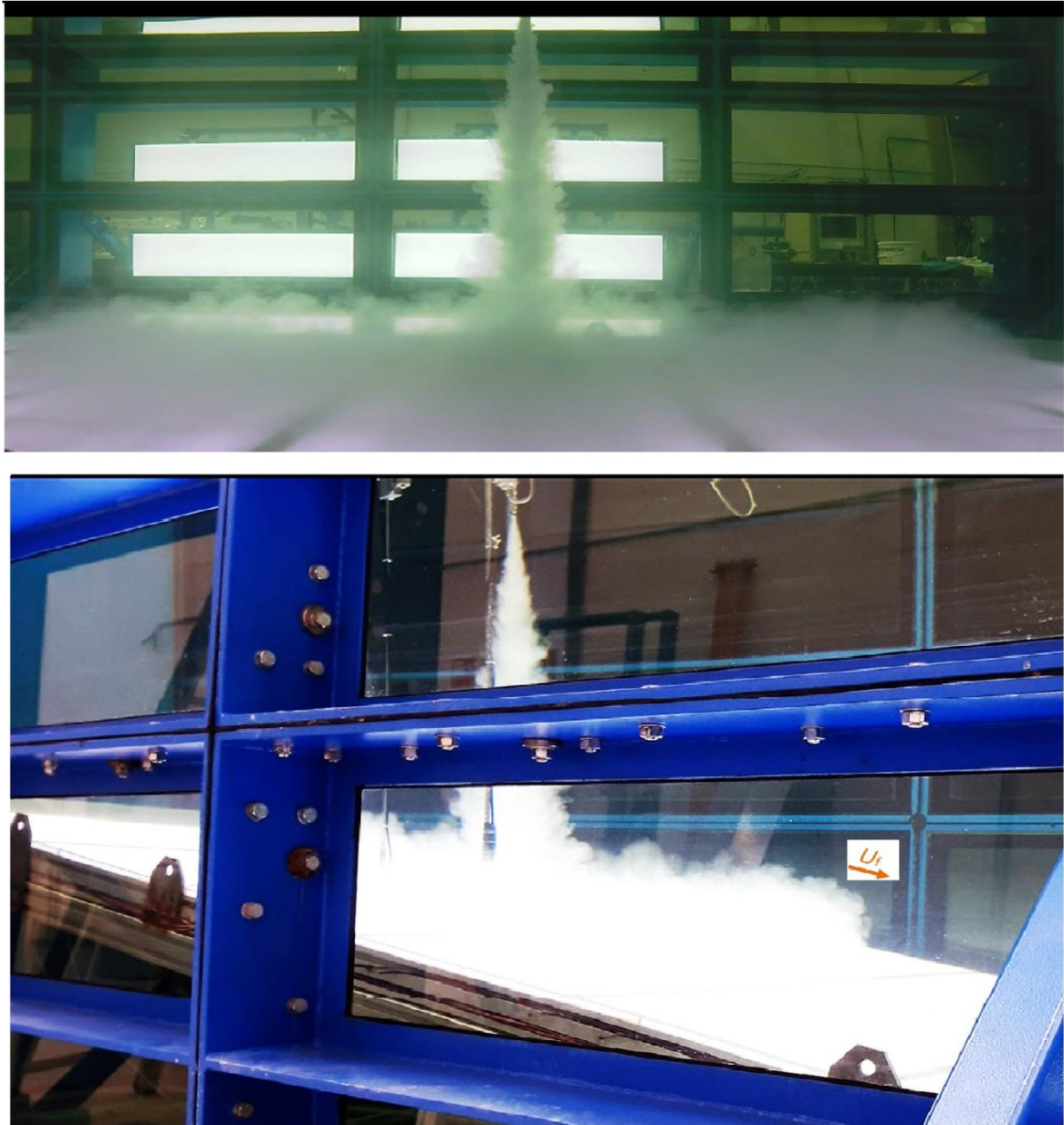


Figure 5-1 Images of the negatively buoyant jet and formed turbidity current after impingement. Flatbed (top) and 10 degrees inclined bed (Bottom. Images taken during experiment  $H=0.5$ ,  $SSCo=20\text{g/l}$ .

## 5.2. Image analysis

Videos images were taken during Experiments with a flatbed (Series A), a GoPro camera captured details of the descending part of the plume and the evolution of horizontal outflow turbid current. During this session, a total of nine experiments in Series A were conducted for various release jet pipe heights  $H=0.25$  m,  $0.5$  m and  $H=1$  m and initial sediment concentrations  $SSC=5$  g/l,  $10$  g/l and  $20$  g/l. An overview of conducted experiments is given in Figure 3-3.

Images were then used to visually analyze the plumes spreading rate and different experimental initial conditions were compared. Obtained results include the plume front velocities and positions in time. It was preliminary planned to extract from images the level of SSC during experimental. However, this plan did not work because the background ink used for the first tests influenced the following tests. This can be seen in Figure 5-3. In this figure, the top image shows a clear contrast between the plume location and

clean water while in the bottom image, due to the diffusion of the fluorescent ink, it is hard to see the plume boundaries compared to the ambient water. Also from the Figure 5-2, it can be seen that the UV light was placed left of the jet, giving a higher light intensity on the left side of the image; consequently images analysis is performed on the left side only.

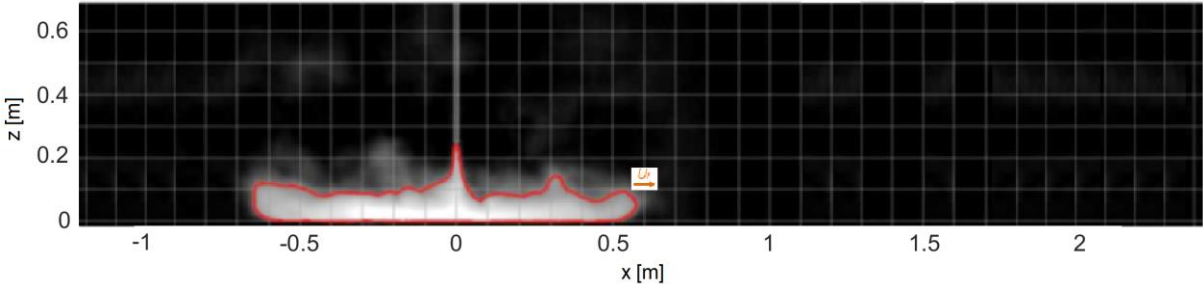


Figure 5-2 Grayscale intensity 80 contours. Processed image for Exp 00 025 20 ( $S=0$ ,  $H=0.25m$ ,  $SSC_0=20g/l$ ).

To solve the problem of the ink diffusion, it would otherwise require emptying the 23 m<sup>3</sup> tank for each test. This was obviously not a feasible option due to time restrictions and cost. In this section of the report, results obtained from videos images are presented.

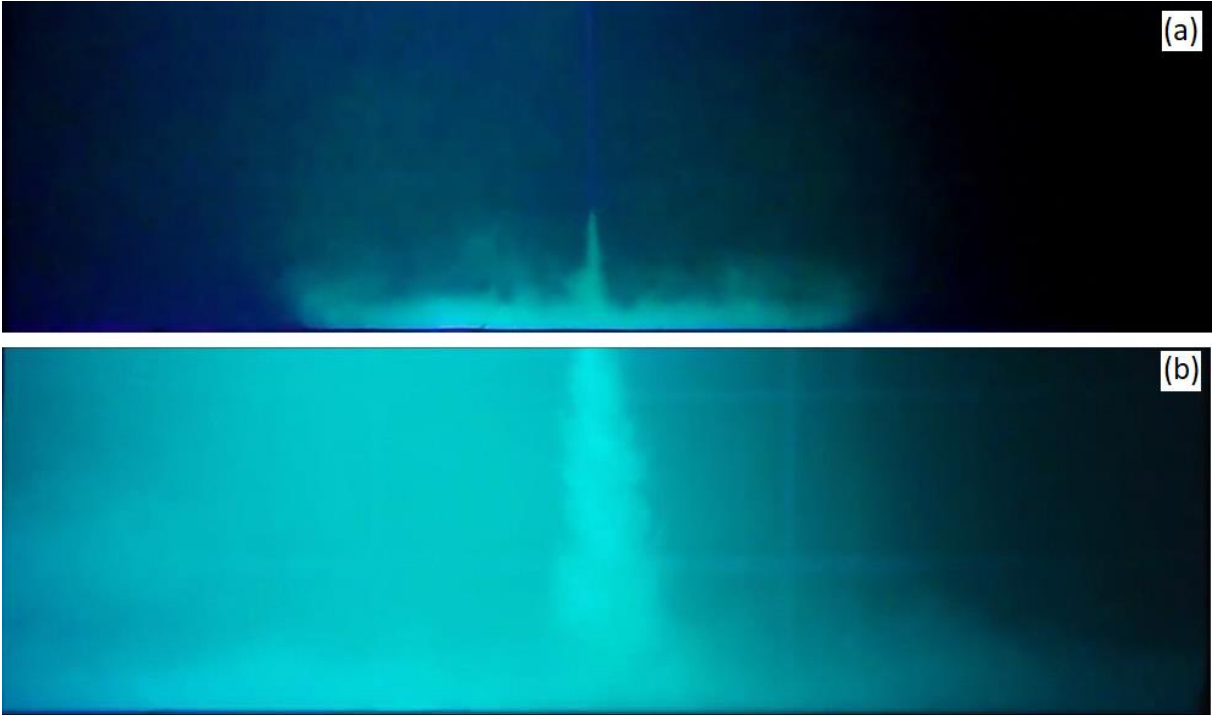


Figure 5-3 Sideview snapshots without video processing: (a) the first test and (b) during the last test. Both videos are taken during an experiment with initial  $SSC=20g/l$ .

This part of the work was done in corroboration with Sjoerd Warringa, an MSc student in Offshore and Dredging Engineering during his Research Exercise which is a requirement for his MSc study package.

**5.2.1. Flow time elapse turbidity current development**

Following the technic explained in Chapter 3, by video post-processing, the plume was separated from the background light, determining the vertically descending and the horizontal turbid current positions as time progress from the beginning of the experiment. Although experiments were carried out in the three-

dimensional domain, visualizations shown in Figure 5-3 are two dimensional (x,z) supported by a 0.01x0.01mm grid plotted in front of the camera frames. Top camera images above the bed were also taken similarly to Figure 5-4. However, all camera positions did not allow to construct visualizations of the flow pattern in all three direction x-, y- and z with the technic used in this research. Three-dimensional visualizations would have been possible with a Laser-Induced Fluorescence measurement system that gives flow slices for quantitative analysis. The last technique is expensive therefore was not used here.

The flow pattern for a jet released at height H can be observed in 2D from the side view images as shown in Figure 5-6, the jet impacts on the table and directed outwards. For release closer to the bed,  $H=0.25\text{m}$ , initially the outward spreading front remains close to the bed and after approximately 30 seconds the front curls upwards. Similar processes and flow patterns were observed for plume release higher from the bed,  $H=0.5\text{m}$  and  $H=1\text{m}$ . However, the upward curling of the front is not as clear as in the case of release closer to the bed. Also, it was observed that for the three different initial SSC, the curling effect is clearly present and stronger for  $SSC_0=20\text{ g/l}$  compared to more diluted initial concentration  $SSC_0=5\text{g/l}$  and  $10\text{g/l}$ . For the release  $H=1\text{m}$ , as it can be also seen in Figure 5-3, the plume source at the pipe exhaust is outside of the view of the camera, the time at which the jet enters the view is set at  $t=0$ . Another observation in Figure 5-3, is that the jet is already much wider once is impacted on the bed. This is due to the fact that from a height of 1m, the jet had more time and distance to entrain ambient water and grow in size compared to lower plumes release. For plumes released higher in the water column, namely  $H=1\text{m}$ , it was observed that the plume was transient compared to the other releases.

Experiments visual observations, also in the LES simulations, showed that the flow out of the pipe was turbulent which matched with expectations based on the preliminary design of the least turbulent tests ( $w_{JO}=0.7\text{m/s}$ ,  $SSC_0=5\text{g/s}$ ). Immediately after the jet exit the pipe; it enters the potential core region. Few seconds after the jet exits, outside the region of the potential core, the jet starts to develop an intermittent pattern which was observed in all experiments. Experimentally, Lee and Chu (2003) determined that the length of the potential core is about six times longer the source pipe diameter. Although in this research, it was not measured, the existence of a potential core was clearly observed, see Figure 2-6. Inside the potential core, small-scale turbulent motions were observed. Due to the turbulent phenomena, the jet/plume mixes entrained ambient water, thereby diluting its mixture leading to an increasing jet diameter while the flow descends towards the bottom.

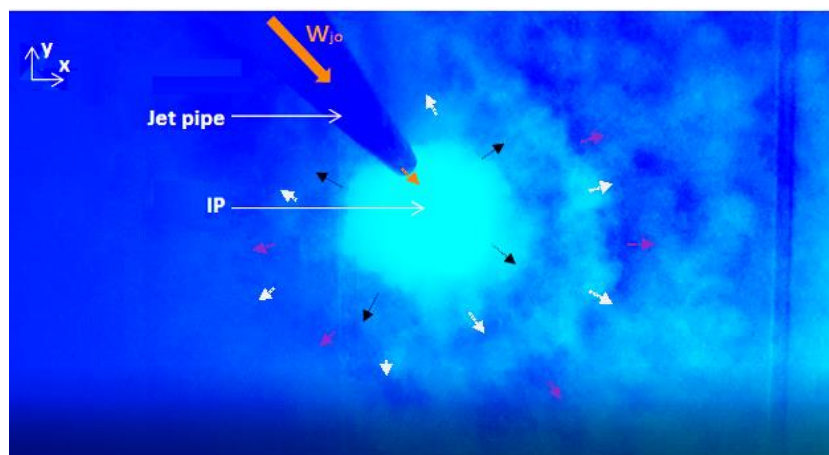


Figure 5-4 Top-view of radially spreading plume on a horizontal bed (Exp Slope=0,  $H=0.25\text{m}$ ,  $SSC_0=20\text{g/l}$ ).

When the plume reached a flat bottom, the vertically descending flow turned into a radially spreading turbid current “density current flow” which flowed horizontally as main flow direction above the flat bottom. In the presence of a sloped bed, the current followed the downslope direction. Because of the intermittent characteristics in the descending flow, when the flow hit the bottom, the flow radiate intermittently plume fluxes with high SSC waves followed by more diluted fluxes. The more diluted wavy

fluxes are caused by the entrainment of ambient clear water. These radial waves can be seen in Figure 5-4 which shows a top view of the development of the horizontal flows pattern after impingement that radially flows outwards from the impingement point. In this image light color spots are of higher SSC while darker spots are areas of diluted water.

The time flow development patterns are shown in Figure 5-6 while Figure 5-5 shows time averaged side view images of 60 seconds of a fully developed flow after 5 minutes of each experiment. Both images are plotted on a 100x100mm grid. In the steady-state images shown in Figure 5-6, it is clear that for plumes released closer to the bed, a higher cloud of sediments are observed and the plume stays closer to the bed compared to the case of larger discharge heights. Also, it is observed that for higher initial concentrations, the sediment clouds are higher than the case of low initial concentrations. Evidence to this will be revealed in the following sections where flow velocities measured and SSC are compared. Based on steady-state equilibrium images shown in Figure 5-5, there seems to be a relation between the horizontal underflow current height  $h_c$ , initially suspended concentrations  $SSC_0$  and the release height from the bed. Kaye and Hunt (2007) found experimentally that  $h_c$  is linearly proportional to  $H$  as  $h_c = 0.075 H$ . This seems to be true for only plume-like impingement because Figure 5-5 shows that the turbid current height created from a source  $h=0.2\text{m}$  is actually higher than the one observed for instance when  $H=1\text{m}$ .

In the present laboratory tests as can be seen in Figure 5-5 and Figure 5-6, experiments with  $H=0.25\text{m}$  and  $H=0.5\text{m}$ , there seems to be a cloud of sediment over a large height from the bed of approximately  $h_c=0.5\text{m}$  (for  $H=0.25$ ) from the bottom which is higher compared to the plume release height  $H$ . This is related to the fact that experimental conditions for  $H=0.25\text{m}$  and  $H=0.5\text{m}$  were both in Jet-like or transitional impingement regime (see Table 3-3) with initial horizontal flow that behaves as wall-jet with energy to suspend particles back to the water column due to turbulence eddies.

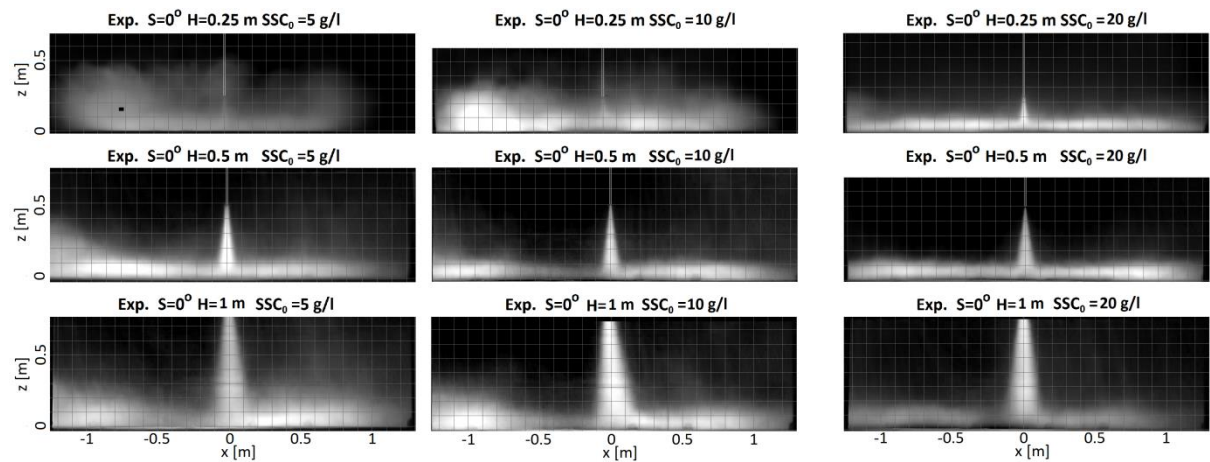


Figure 5-5 Steady states 60 seconds averaged images of each experiment plotted on a 100x100mm grid.

Results of steady-state images shown in Figure 5-5, it can be seen that for experiment with low  $SSC_0$ , for instance, 5 g/l,  $h_c$  is higher compared to the case of higher  $SSC_0$ , for instance, 20 g/l. The present seems to stay close to the bottom. An explanation could be the plume released with higher bouncy force  $B_0$  due to suspended sediments, has also higher density. This is the case of  $SSC_0 = 20\text{ g/l}$  compared to the density of the lower  $SSC_0 = 5\text{ g/l}$ .

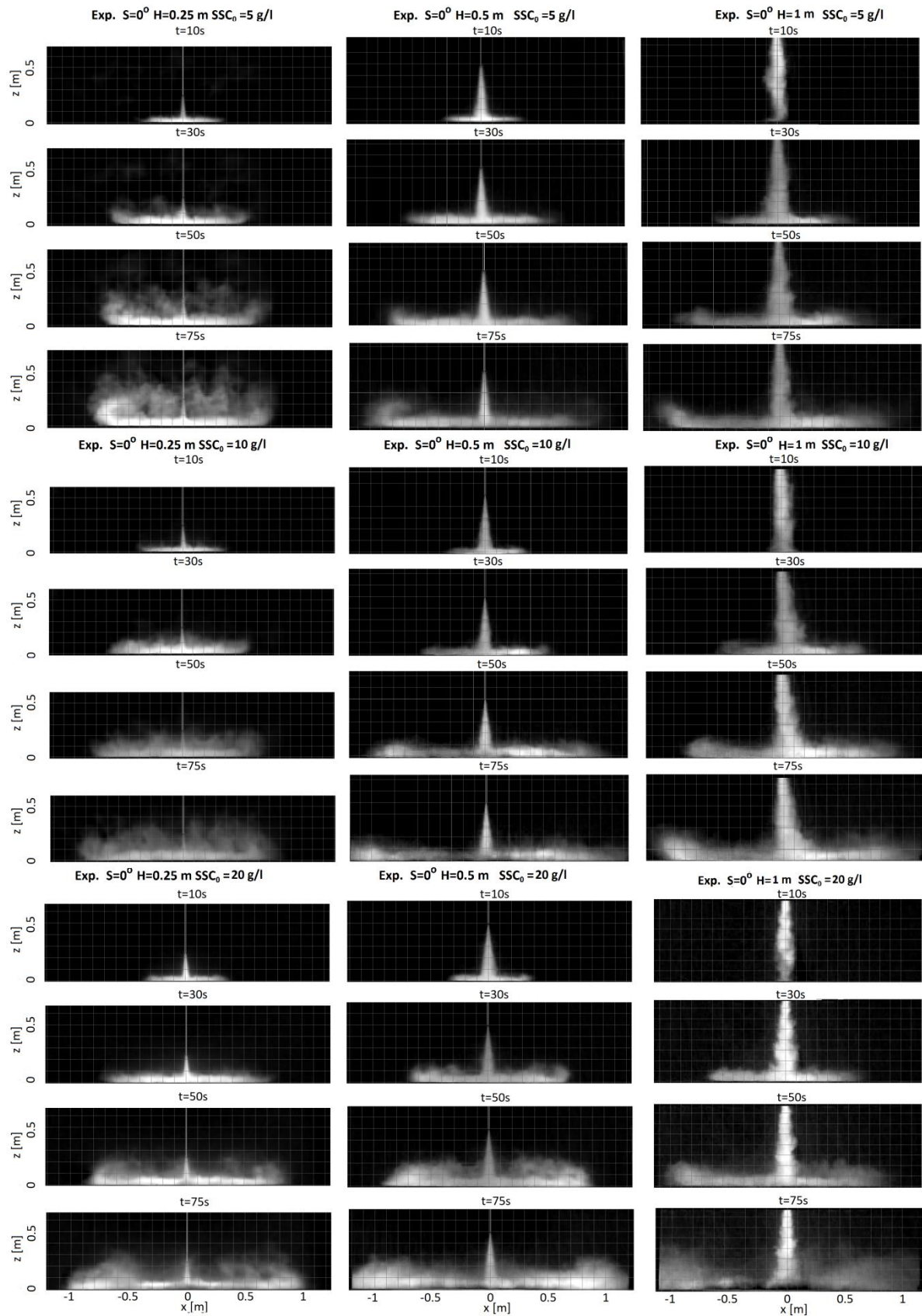


Figure 5-6 Snapshots at time = 10s, 30s, 50s, and 75s, images are plotted on 0.1x0.1m grid. Note that for H=1, the turbidity current front is out of the camera frame.

### 5.2.2. Turbidity current front Position

A density current at a flatbed flows radially in the outward direction of the impingement point under influence of momentum; see the current development in Figure 5-6. For this research, after the video analysis, the front position determined by defining the edge of the plume. An arbitrary grayscale intensity value of 80 was chosen since this gave the best match to the plume contour (see Figure 5-2).

Using contours, the position of the plume front was determined and stored for given times. An alternative could be to trace the plume by following the progress in time of the edge of the plume at the bed. Results obtained from both technics were similar.

Plumes front position presented in Figure 5-7 are obtained with a grayscale intensity value of 80. Results show that denser plumes travel greater distances than the ones released with low SSC. Also, it can be seen that plumes discharged from high H travel greater distances while when the plume is disposed of closer to the bed, stays closer to the disposal location. An explanation for that is that discharged plumes with moderate concentration with a higher discharge height H became much more diluted because of the entrainment at the impingement and, hence, the viscosity of the fluid is reduced. Therefore, they traveled further.

Figure 5-19 (bottom) shows the effects of a sloped bed. This unprocessed snapshot image taken after  $t=30$  shows that after the impingement, due to both buoyancy and momentum, the horizontal flow is mainly in the downslope direction. Also, partly the current flows a short distance in the upslope direction due to the horizontal momentum in that direction. The upslope distance was larger during the tests with less dense plume compared to the denser plume. For example during Exp1010005 which has  $SSC_0=5g/l$ , the current overtopped the bottom table at the upslope edge of the table. This did not happen during Exp1010020 with  $SSC_0=20g/l$  as the current is heavy and hence pulled downslope by gravity. It is important to note that not all with  $SSC_0=5g/l$  had the currents overtopped the upslope edge of the table. As it was introduced in section 5.2.1, plumes released closer to the sloped bed ( $H=0.5m$  and  $H=0.25m$ ) stayed closer to the impingement point, hence their horizontal flow did not reach the upslope edge of the sloped table.

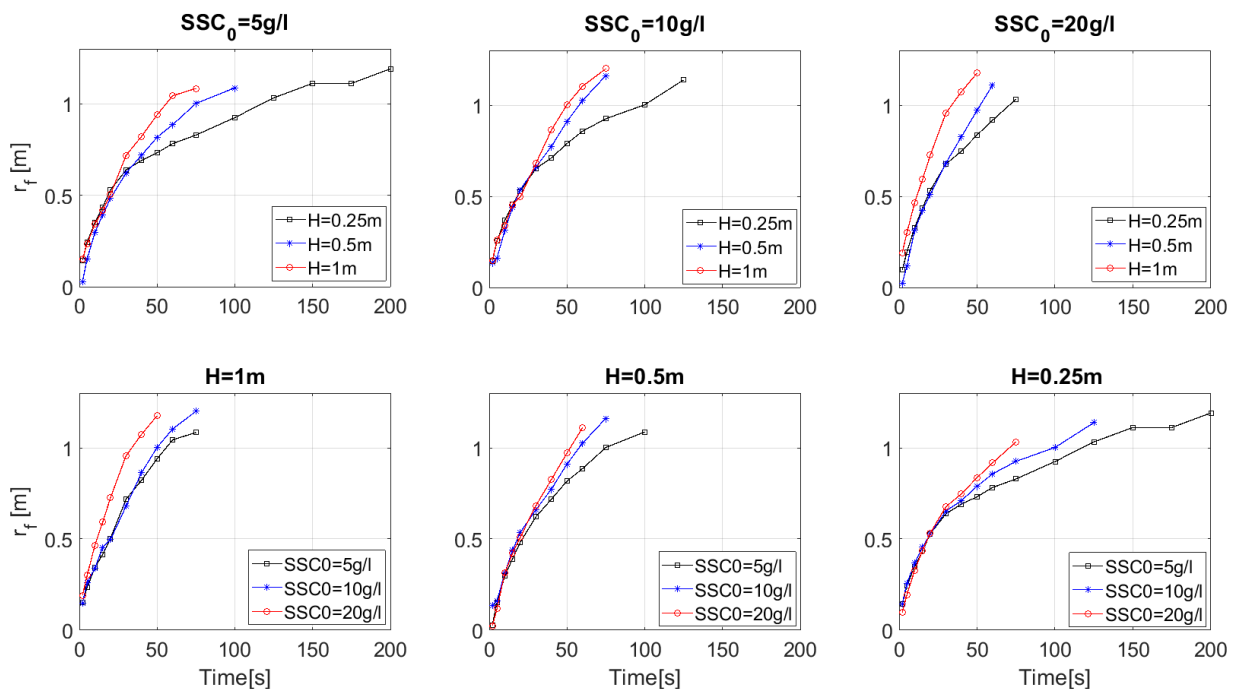


Figure 5-7 Radial spreading turbid driven current plume at flatbed as a function of time. Note that the curves that end soon for instance for the plume released at  $H=1m$ , means that the front of the turbidity current was already outside the camera frame.

### 5.2.3. Turbidity current front velocity

For a flatbed; friction and entrainment of ambient fluid balance the gravitational acceleration. When a descending plume touches the bed it spread radially creating an inertial gravity current that follows a functional dependency on propagation time. In the present laboratory tests, the horizontal spreading position of the current front as introduced in section 5.1.2 was traced by following the progress in time of the edge of the plume at the bed using grayscale intensity value of 80. In the CFD model, to track the current position and hence deduct the front velocity  $U_f$ , time-lapse images are plotted by setting the minimum SSC at 10% of the initial SSC<sub>0</sub> which were the inputs boundary conditions for TUDflow3D at the pipe exit, see Table 4 1. Figure 5 1(C) shows an example of 2D (x,z) plot of SSC by setting the SSC at 10% of SSC<sub>0</sub> for Run1010020 at t=60s. Results presented in Figure 5-8 shows that the gravity current front speed  $u_f$  is higher for denser plumes. Also, plumes released at higher water depth (higher H), gravity current resulted after the impingement at the bed travels faster compared to closer to the bed release. Hence, plume release height H with higher initial SSC<sub>0</sub> at the orifice produces faster spreading plumes.

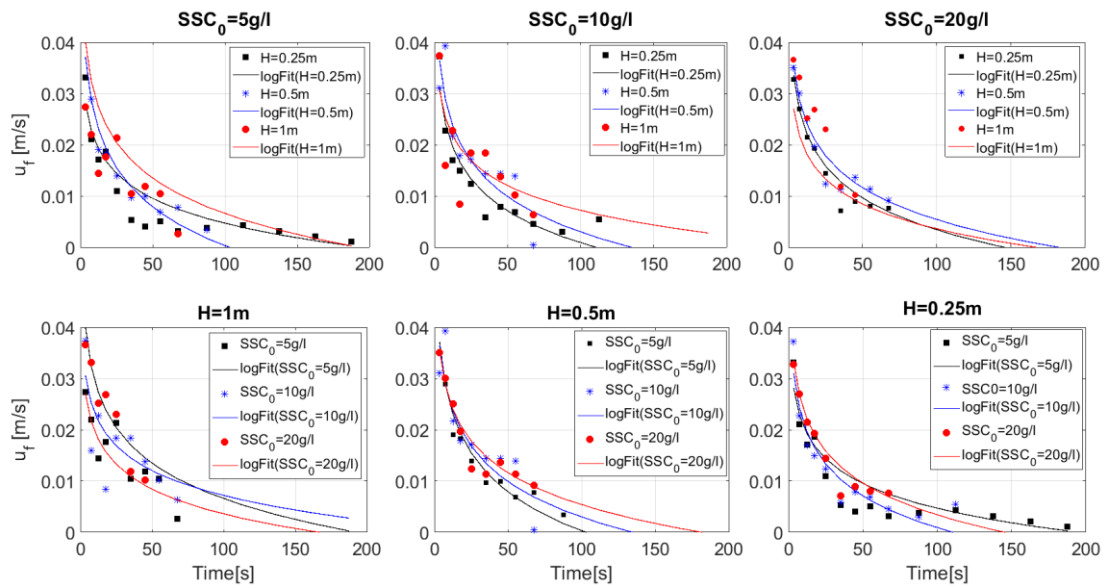


Figure 5-8 Density current front velocity  $u_f$  as a function of time and logarithmic fitting curve.

### 5.2.4. Sediment deposition ring

Due to the bottom horizontal boundaries in flow domain, complex flow interactions occurred, for instance, the phenomena of jet impingement, internal hydraulic jumps and other flow instabilities and recirculation flow due to turbulence. When the type of descending jet/plume flows such as in this research hit the bottom boundary, the underflows exhibited two well-documented propagation phases (Chowdhury, 2014). The first one is a radial momentum-driven wall jet phase near the impingement region or Zone of boundary influence. The second phase is an inertial gravity current phase after the completion of the wall jet phase.

In this research, both phases were present. In table Table 3-3, types of observed jet impingement in the laboratory experiments were classified. These types of impingement depend on the initial release parameters and the distance from the release height from the bed. In this research, all plumes released closer to the bed ( $H = 0.25m$ ) were Jet-like impingement. The experiment of the plume released at 1m high impinged at the bed as plume-like impingement while the rest of experiments were in transition regime.

During cases jet-like impingement, the jet flow reached the bottom with relatively higher velocities. Because of that, no sediment was deposited inside a radial momentum-driven wall jet region. All sediment was transported away from this region. The observed transport at the bed is a form of a circular shape for a flatbed (see Figure 5-6). It was observed that the sediment ring was a half-oval shape in the presence of the slope with the oval-shaped towards the downslope direction due to gravity;

see Figure 5-9 (c). In the later time, sediment accumulated and formed a deposition ring around the impingement point. During the formation of the deposition ring in a 30 minutes experiment, three waves in circular form were observed to follow each other.

Inside the zone of boundary influence introduced earlier, the spreading density current has been regarded as an internal hydraulic jump in several earlier studies (Wilkinson and Wood 1971; Lee and Jirka 1981). The location of the hydraulic jump has been linked to initial flow parameters (FO, MO, BO, and VO). Experimentally, the hydraulic jump was observed at a distance of about ten times the orifice pipe diameter ( $x=10D$ ) (Chowdhury, 2014).

Although there are not enough flow measurements done very close to the Impingement point, it is believed that the observed deposition ring was located at the inner diameter of the depositions ring hence there. Due to the Hydraulic jumps, the flow with is in supercritical regime reduces its velocity due to mainly the wall friction leading to deposition of the sediments forming a deposition ring. When the buoyant jets impinge on the bottom as plume-like impingement, there was no deposition rings observed, see Figure 5-9 (b) which was the test with initial SSC equal 20g/l release at 1 m height from 10 degrees sloped bed. During this particular experiment, the descending buoyant flow reached the bottom in plume regime when it means flow velocity had decreased considerably at the bed allowing part of the sediments to deposit at the bed. Finer sediments were transported with the density current to a farther distance outside the radial momentum-driven wall jet region.

In the LES model, for all cases the no deposition ring was observed because Erosion/Deposition was off. Sediment that reached the bed has counted depositions and do not come back into the flow domain. Therefore, the total deposition of sediments is in a form of a volcano with more sediment that deposited closer to the impingement pointed and counted as deposition.

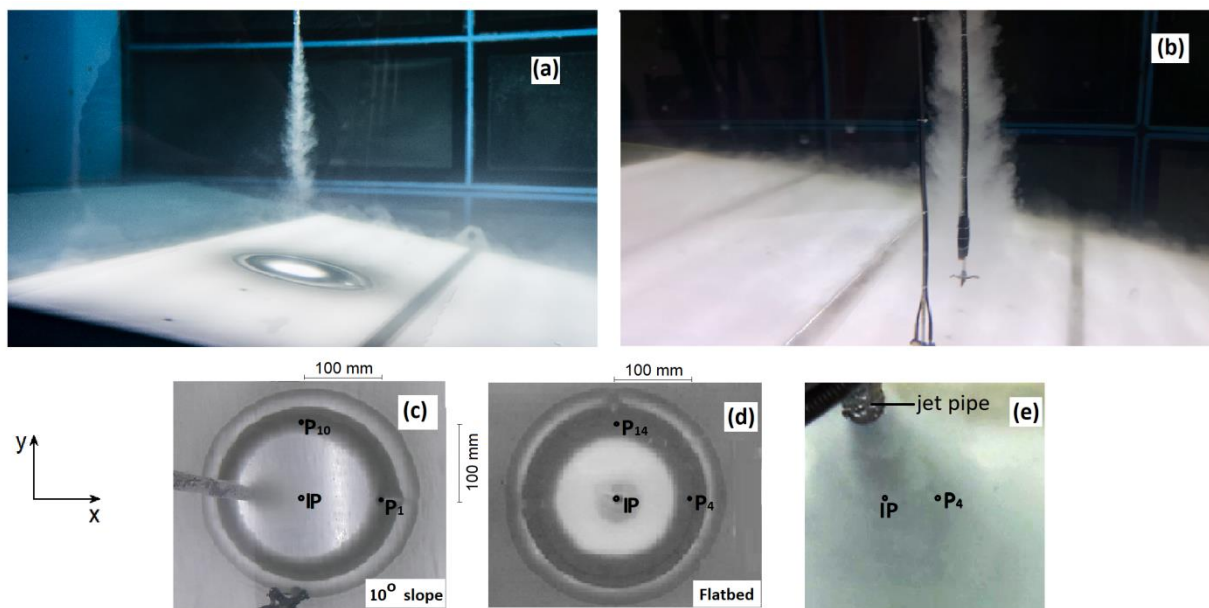


Figure 5-9 Sediment deposition rings formed after 30 minutes. (a) shows a side view of a semi-elliptic sedimentation ring formed during the experiment ( $H=0.5m$ ,  $SSC_0=20g/l$ ) impinging on a sloped bed and (c) shows its top view. (d) shows a top view of a circular sedimentation ring of the same experiment source parameters ( $H=0.5m$ ,  $SSC_0=20g/l$ ) but impinging on a flatbed. (b) and (e) show a side and a top view for the experiment ( $H=1m$ ,  $SSC_0=20g/l$ ) impinging on a sloped bed. Note that for this test there are no sediment deposition rings observed (they are plume-like impingement regime).

### 5.3. Direct local turbidity measurements

The original plans for Direct local NTU measurements were to obtain near-bed SSC of the plume current. However, as introduced earlier, this plan did not work because when the valve was open for sampling, fluid near the bed flowed into the sampling tube from an area around the tube inlet for approximately 60 mm high from the bed, see in Figure 3-11 the velocity profile measured above the tube inflow when the tapping valve is opened for sampling.. For this reason, results shown in Figure 5-11 are called local SSC. After converting the measured NTU measurement into SSC in mg/l, different experimental initial conditions were compared. Results from Direct local SSC measurements taken at locations shown in map Figure 3-3 measurements agree qualitatively with results from image analysis.

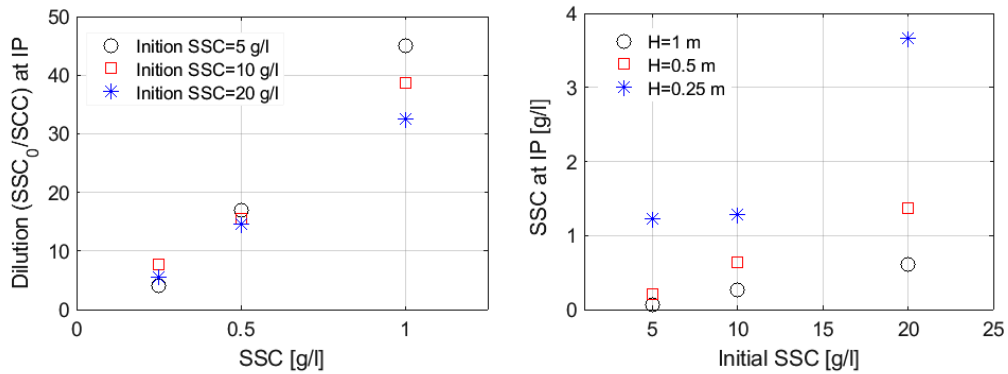


Figure 5-10. SSC (right) and average dilution (left) measured at the impingement point.

As it can be seen in Figure 5-11, plume release from higher distance H from the bottom, resulted in less SSC near the disposal location. This can clearly be seen in Figure 5-11, especially for an area closer to the impingement point (small  $x < 0.5m$ ). On the other hand, plumes released closer to the bed (small H) stays near the disposal location, especially for the release height H=0.25m. Furthermore, when released plume the initial condition was higher SSC<sub>0</sub>=20g/l, local SSC inside the plume current became also higher compared to less dense plume released at the same height from the bottom.

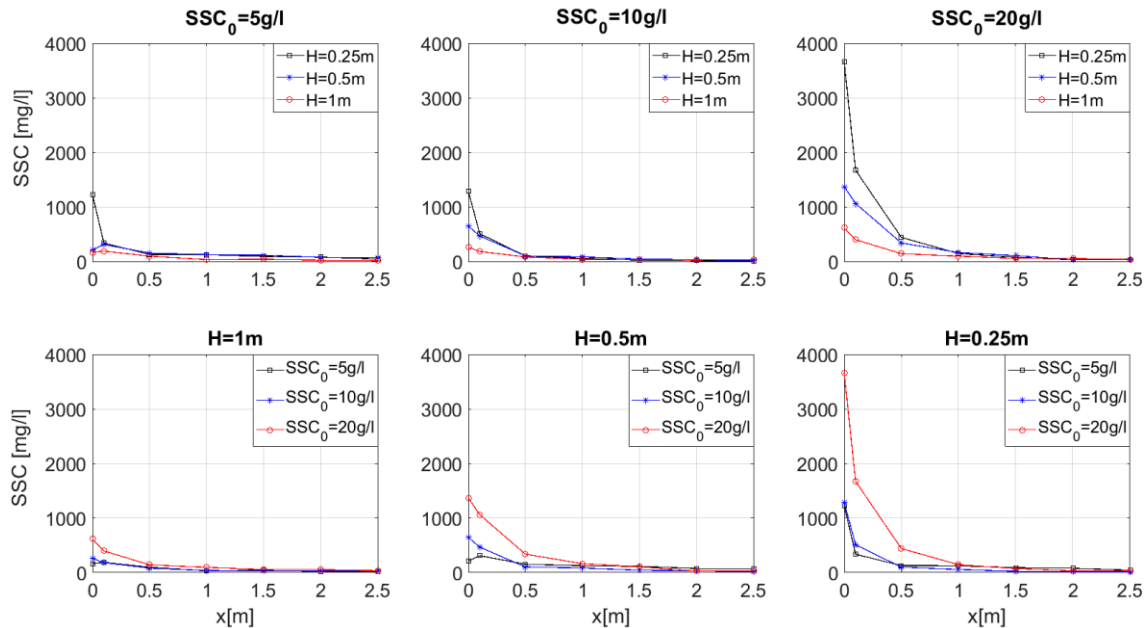


Figure 5-11 Direct local turbidity measurements by AL450T-IR standards NTU.

Comparison of the experimental initial conditions for Local SSC shown in Figure 5-11, gives clear indications only closer to the impingement point for  $x < 0.5m$ . To have a detailed analysis for greater distances from IP  $x > 0.5m$ , results from Figure 5-11 were reported on a logarithmic plot in Figure 5-12.

Although it is clear that for the same  $SSC_0$ , plume released at  $H=1m$  diluted 4 times more as they traveled a long distance before reaching the bed. However, it seems that after  $x > 1.5m$  higher local SSC was a measure for the release from 1m height compared to release from 0.25 m and 0.5m height from the bed. Although this is clearly observed in Figure 5-12 for tests with  $SSC_0=10g/l$  and  $SSC_0=20g/l$ , it is not clear for  $SSC_0=5g/l$ . Also, it is important to note that unfortunately due to the limited size of the experiment, local SSC is only measured up to  $x > 2.5m$ . Probably measurements at larger  $x$  would make it clear.

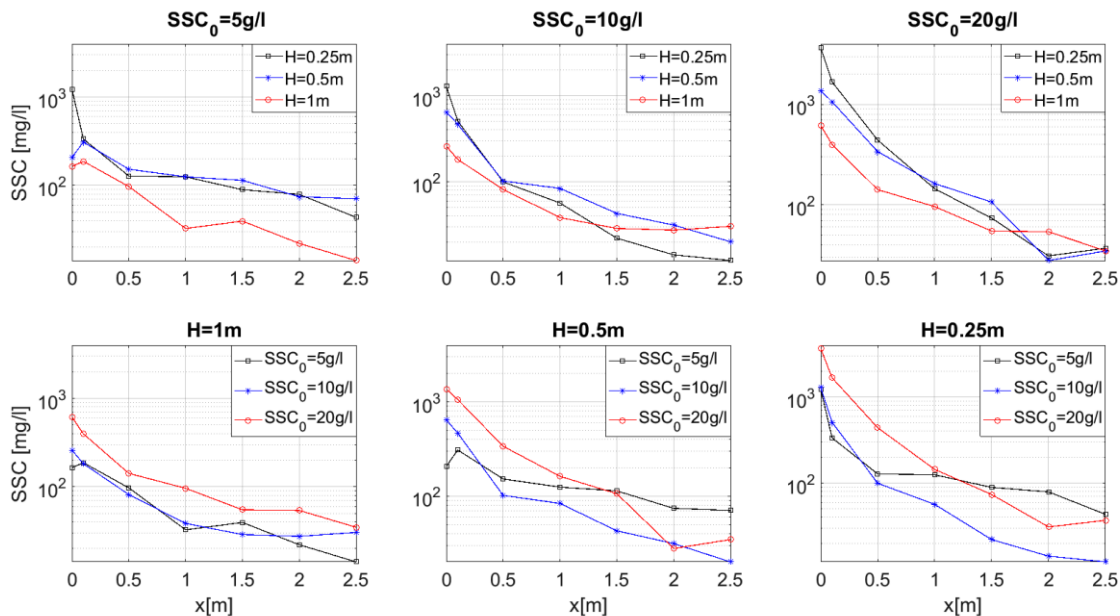


Figure 5-12 Logarithmic plots of Direct local turbidity measurements by AL450T-IR standards NTU.

## 5.4. Foslum optical suspended sediment concentration

Foslum optical suspended sediment concentration results are introduced here while detailed analysis is given in Chapter 6. The results from the series of experiments performed to study the spreading of negatively buoyancy jet released into ambient clean water show that the local SSC concentration depends on the initial jet parameters as well as the release heights. SSC measured in the density current show that the release of height has a significant effect on the turbid current. The jet released from a one-meter height diluted 4 times more than the jet released at 0.25 m height before it reached the bottom. With the same initial SSC of 20g/l, at the impingement point, an average of 3.7g/l was measured for a release height of 0.25m and 0.6 g/l for a release height of 1 m. Direct SSC measured at the impingement point is shown in Figure 5-10.

## 5.5. Density current velocity profile (ADV)

In Figure 3-8 shows a comparison of the velocity time series taken at the same elevation ( $z = 10$  mm) above the bed for a point located at a distance closer to the impingement point ( $x=100$  mm) and a point located at  $x=500$  mm. Velocity measurement presented in Figure 3-8 shows that the velocity fluctuations depends on the plume release height and is higher in the case of release close to the bed. The differences are due to turbulence present in the flow. This is in agreement with results from section 5.2 where it was observed that for the release elevations 0.25 m and 0.5m above the bed, the plume hit the bed as jet-like impingement or in transition, hence more turbulent eddies leading to more velocity fluctuations compared to release from 1 m above the bed where the plume could reach the bed as plume-like impingement. Furthermore, Figure 3-8 shows that both the magnitude of the mean velocities and fluctuations reduce with increasing  $x$  distance from the impingement point. This is shown in the same figure by a lower and almost constant  $u_x$  time series taken at the same elevation but at  $x=0.5m$ . Detailed analysis ADV data and CFD simulation results are given in Chapter 6.



## CHAPTER 6

# CFD Simulations results

---

The topic of this chapter is results of CFD simulations of the Near Field spreading of the DSM plumes with continuous negatively buoyant jet/plume discharged in ambient water with different initial conditions. CFD results are compared with experimental results. Furthermore, some interesting observations about the impinging jet/plume are discussed.

### 6.1. Introduction

Deep-sea mining wastes will be disposed back to the sea as negatively buoyant plumes released in the water column close to the seabed. To predict environmental impacts caused by these plumes, a numerical model tool was used. The used model simulates the plume behavior and mixing with ambient water as well as the interactions with the seabed. For such a numerical model to be trusted, it must be validated. To validate a numerical model, laboratory experiments measurements reported in the previous chapter can be used. To reach one of the goals of this research, the laboratory experiments were reproduced in TUDflow3D CFD model introduced in Chapter 4. In this chapter, results obtained by simulating the same conditions as in the laboratory tests are compared. Eighteen laboratory experiments cases were reproduced in the CFD model by setting similar initial conditions at the boundaries as done in the experiment. Simulated initial flow characteristics and boundary conditions reported Table 4-1. They included three different plume release heights  $H$  from the bed (0.25m, 0.5 m and 1 m), three different initial  $SSC_0$  (5 g/l, 10 g/l, and 20 g/l), two different bed slopes (horizontal and 10 degrees slope bed). In addition, one simulation that counted the effects of a uniform ambient current  $u_c = 0.014\text{m/s}$  was run. The jet outflow was a pipe of 10 mm diameter releasing the plume at a constant flow rate  $Q_{jo} = 3.3\text{ l/min}$  (or average pipe outflow velocity  $W_{jo} = 0.7\text{m/s}$ ).

Figure 6-1 show an overviews example of CFD results. The center slice images show the time evolution of sediment plumes spreading for the simulation where the mixture was released at an elevation  $H=0.5\text{m}$  and contained an initial  $SSC_0 = 20\text{ g/l}$ . The left side of the figure shows results for flatbed and no ambient current, the same simulation but with an ambient current in the middle image and sloped bed with no ambient current on the right. As it can be seen in this figure, due to current the evolved turbidity current is drifted in the ambient current direction and more sediment particles are kept in suspension. The slope has a significant influence on the mixing rate, as can be seen in Figure 6-1, after 6 minutes, the plume has traveled more than double the distance in x-direction compared to other two cases shown in the same figure. Another observation is that due to the gravity pull in the downslope direction, the size of the turbidity current front is much larger.

Detailed analysis and comparisons of CFD results and the laboratory measurements will be discussed in the following section where the effects of initial  $SSC_0$ , the presence of a sloping bed, the plume release height and uniform ambient current will be discussed separately and the compared to each other later on.

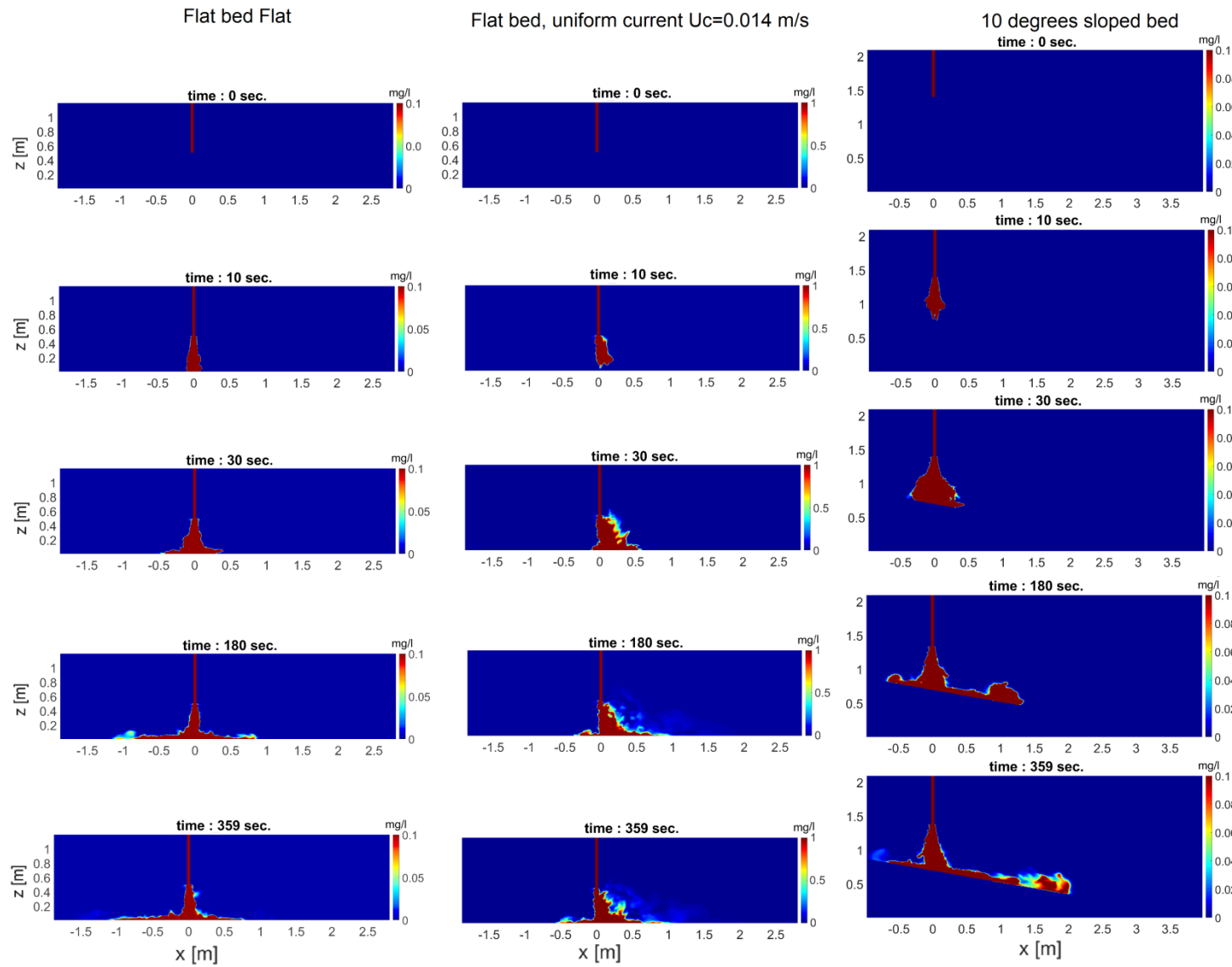


Figure 6-1 CFD LES model results. Centre slices images of sediments plume spreading for the simulation  $H=0.5$  m and  $SSC_0=20$  g/l. On a flatbed and without ambient current(left column). Flatbed and ambient current (middle column) and sloped bed without ambient current(right column).

### 6.2. CFD simulation results of impinging Jet under submerged condition

At the plume source, the jet flow is driven by both momentum and buoyancy forces. The momentum force is due to initial pipe exit flow velocity and buoyancy force is caused by excess density due to suspended sediment in the plume. Experiments and CFD results show that close to the exit ( $Z^* < 10D$ ), the flow is mainly dominated by vertical momentum. After some distance, the velocity reduces when the release mixture flows towards the bed. Based on submerged jet flow theory explained in 2.2.3 and the experimental conditions from section 3.7, results obtained this research agreed well with theory. It was observed in model simulation results that depending on the plume releases height  $H$  from the bed, there is a transition from initially vertical momentum dominated regime to a buoyancy dominated plume flow regime. After the plume hit the bed, a horizontal wall jet was created and turbidity current was evolved.

Inside the turbidity current, whereas all suspended particles have a tendency to sink, large particles sink faster than small particles. Large particles rained out of a plume and settle on the seabed near the disposal location. Due to turbulent and diffusion flow characteristics, finer particles were transported in suspension to a greater distance away from the disposal location. As shown in Figure 6-2, the CFD model simulations show similar impinging plume behavior and phenomena as observed during the laboratory tests. In this figure, instantaneous experimental front views and CFD center slices for both a flatbed (Top) and 10-degree bed (bottom) are shown. In both cases, similar initial characteristics ( $H = 1m$   $SSC_0 = 20 g/l$ ) were used. Results show that when the plume impinged on a horizontal bed, it spread radially and symmetrically. On the other hand, in the presence of an inclined bed, the turbid current flowed mainly in the downslope direction due to gravity pull. Little flow in the upslope direction was observed, see Figure 6-2 (bottom panel).

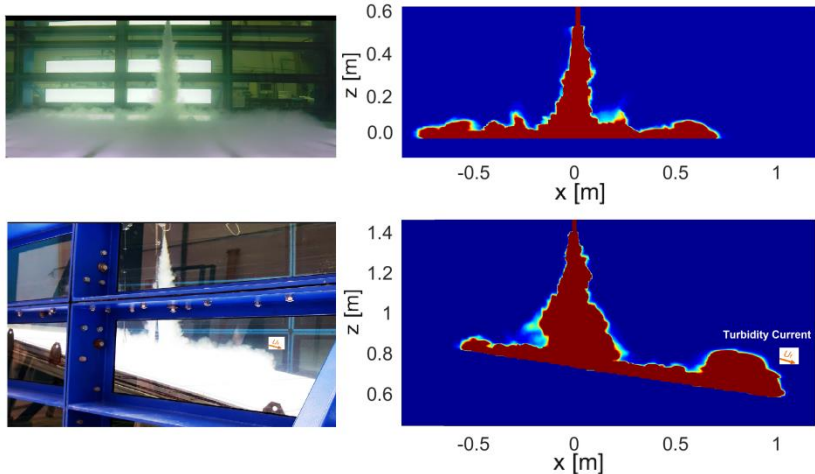


Figure 6-2 Instantaneous front view images of laboratory tests and CFD centre slice images. Flatbed,  $SSC_0=20g/l$ ,  $H=1m$  (Top panel) and 10 degree slope bed,  $SSC_0=20g/l$ ,  $H=1m$  (lower panel). **Note** that the laboratory images are not scaled and show front views while the CFD images are cross sections at the plume center.

### 6.3. Turbidity current flow reflection on the vertical sidewalls

The table representing the seabed during laboratory experiments allowed for the sediment plume to fall over the table when it reached the edges. On both sides of the table, 0.25m gaps were left. However, it was noticed that 0.25m distance left between the table and the modular tank wall was not enough. The plume current flowed horizontally closer to the bed and outside the table surface, the plume falls over the table but due to the still existing horizontal momentum at the modular vertical walls, part of the plume reflected. Most of the reflected sediments fell into the gap and fell downward the tank bottom. Part of the reflected plume flowed upward and returned back towards the impingement point hence affecting measurements closer to the walls at locations  $P_{17}$ ,  $P_{13}$  and  $P_9$ . Due reflected plume influences on measurements at these locations, these points were kept out of the measured data analysis. It is

important to remind that gap at the table edges during experiments was not implemented in the CFD model. This can be seen in the 3D sediment plume shown in Figure 6-3. CFD results show the turbidity current reflected upwards when the flow reached the vertical sidewalls.

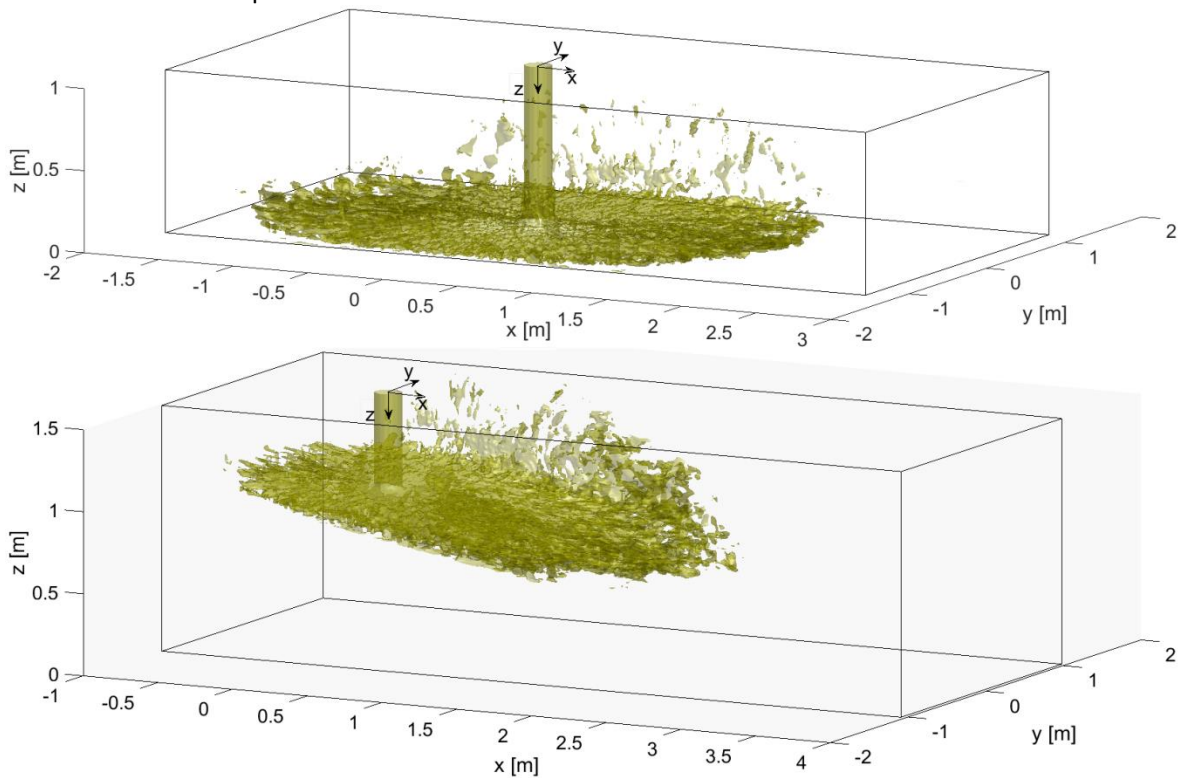


Figure 6-3 Three dimensional CFD results, sediment plume spreading after 6 minutes for the plume mixture release at  $H=1m$  with  $SSC_0=20g/l$ . The top figure shows the spreading on a horizontal bed while the bottom figure shows a similar simulation with the same boundary conditions but falling on a 10 degree sloped bed.

#### 6.4. Turbidity current interactions with the bed

Figure 6-4 shows two dimensional CFD simulation results of the time-averaged horizontal flow velocity (top panel) and cumulative sediment deposition (bottom panel) on a horizontal bed. For both cases, the plume is released at elevation  $H=1m$ . From left to right, images represent results obtained for initial  $SSC_0=20g/l$ ,  $SSC_0=10g/l$  and  $SSC_0=5g/l$  respectively. When the descending plume hit the solid bed, the flow must spread radially and symmetrically in all horizontal directions causing the horizontal velocity components at the impingement point to be zero (stagnation point at coordinates  $x=0, y=0$ ).

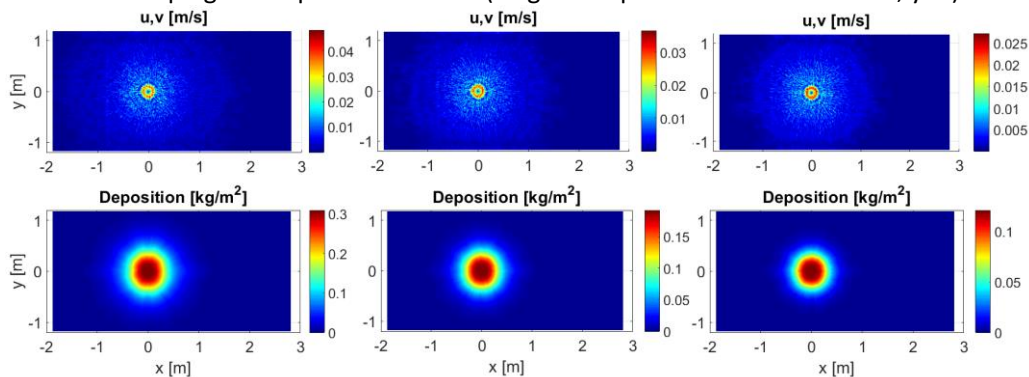


Figure 6-4. Two dimensional (x,y) top views of CFD resulted in horizontal velocity (top images) and cumulative sediment deposition (bottom images) at the bed after 360s. Simulation of experiment with a flatbed and three different cases of initial  $SSC_0=20g/l$ ,  $SSC_0=10g/l$  and  $SSC_0=5g/l$  all released from  $H=1m$ . Note that the color-bar have different scales. The size of the deposition ring and color-bar scale decrease from left to right.

In both scenarios shown in Figure 6-4, the stagnation point at the impingement point was observed. Inside the impingement region, the horizontal flow velocities are higher and reduce with decreasing initial  $SSC_0$ . CFD Most sediment deposited at the bed and accumulated mainly close to the disposal location in a form of a pancake, which is thicker near the impingement region where a larger amount of discharged sediment stayed. The size and magnitude of the deposition is wider and larger for simulation denser plume ( $SSC_0=20g/l$ ) compared with initially less concentrated plumes ( $SSC_0=10g/l$  and  $SSC_0=5g/l$ ). Note that the colour-bar in Figure 6-4 has different scales. The deposited sediments formed a circle or symmetric pancake shape, as Figure 6-4 shows for tests done on the horizontal bed. With a sloped bed, the shape of the deposition was not symmetric over the  $y$ -axis anymore, as more sediment deposited in the downstream  $x$ -direction, see Figure 5-9(c).

Figure 6-5 shows the instantaneous  $y$ -axis cross-sectional at  $x=0$  of the SSC and velocity slices. These results are obtained for a simulation where the plume was released from a height  $H=1m$  with  $SSC_0=20g/l$  spreading on a flatbed. In this figure, it is clearly shown that the turbidity current contains higher SSC closer to the release location and dilutes outwards towards the boundaries. As discussed earlier, the simulation shows that the plume reflects on the sidewall. This can be seen in the following 2D Figure 6-5 as well in 3D Figure 6-3.

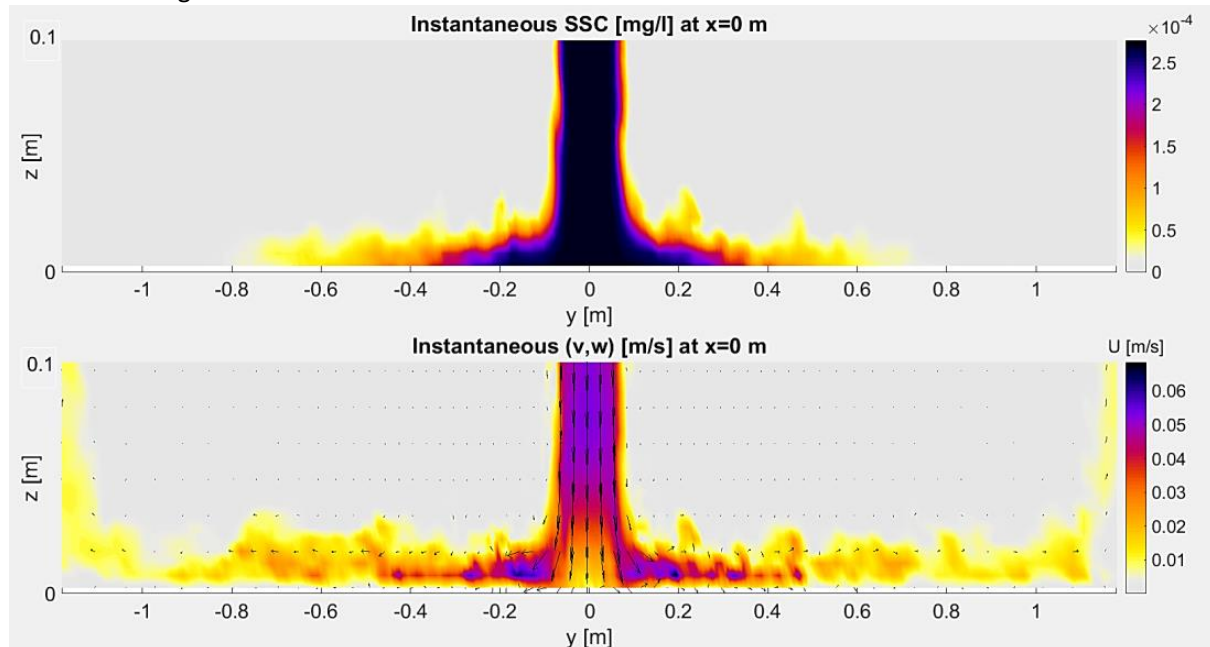


Figure 6-5  $y$ -axis centre slice at  $x=0$  of LES results. Predicted horizontal velocity and SSC ( Run 00 100 20).

## 6.5. Turbidity current flow velocity and SSC profiles CFD prediction

Figure 6-6 shows a typical time averaged turbidity current flow velocity and SSC measurements profiles. Each image in this figure shows three profiles measured at distances  $x = 0.1m, 0.5m$  and  $2 m$ . In addition Figure 6-6 compares results obtained for bed inclination of  $0^\circ$  and  $10^\circ$  and results of plume released at  $H = 1m$  (the first two column) and  $H = 0.250m$  (column 3 and 4) for both release initial  $SSC_0 = 20g/l$ .

Based on Figure 6-6, the CFD model simulated well the experimental results; both the flow velocity and SSC were predicted with acceptable accuracy. In addition, one can conclude that the model was able to capture the physics involved and flow regimes. However, little differences are observed in the upper parts of the velocity profile where high velocities were measured compared to CFD predictions. These differences can be explained by the fact that for elevations  $z > 40 mm$  above the bed, the ADV sensor was not accurate enough due to a lack of signal strength. For example, for the profile at location  $x = 0.1m$ , one can locate the interface between the ambient water and the turbidity current to be at an elevation of  $z = 35mm$ , hence the turbidity current thickness  $h_c$  is about  $35mm$ . This explains why single

point velocity measured at  $z > 40$  mm are inaccurate due to bad signal to noise ratio(SNR), see the SNR profiles in Figure 6-7. When collecting raw data (e.g. at 25 Hz), it is recommended that the SNR should be consistently above 15 dB. The lack of enough particle scattering is also observed for measurements farther away from the impingement point, for instance at  $x > 2$ m, see Figure 6-7. Hence inaccuracy in the average velocity profile results shown for instance in Figure 6-10 or Figure 6-11 measured at  $x = 2$ m.

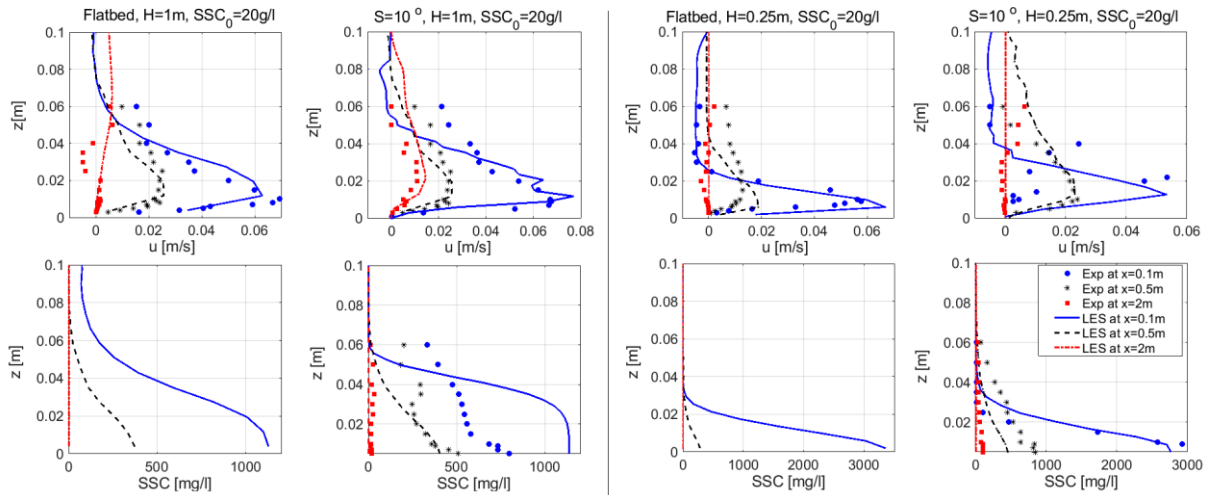


Figure 6-6 Typical (top row) velocity and (bottom row) suspended sediment concentration profiles of turbidity current flow generated by impinging plumes.

In Figure 6-6 SSC experiment data for inclined bed are missing, the Foslum optical suspended sediment concentration measurements were not carried out due to the sensor calibration issues. The problem with the Foslum was that during the measurement SSC profile measurement starts from the highest measured point at  $z = 60$ mm, after few point measurement, the sensor probe surface where IR-light is emitted could become dirty. When the sensor is moved downwards for the next point measurement, the sensor would then measure excess local SSC because the IR-light passing through the measuring volume was already attenuated by particles fixed on the light emitting or receiving sensor probes. A definite solution for this inaccuracy would require cleaning the Foslum probe for each single point measured, which was not possible due time issue and would also make the steady state flow condition to become unstable. However, the accuracy of the Foslum was improved by cleaning the sensor at least before each test that produces a complete SSC profile.

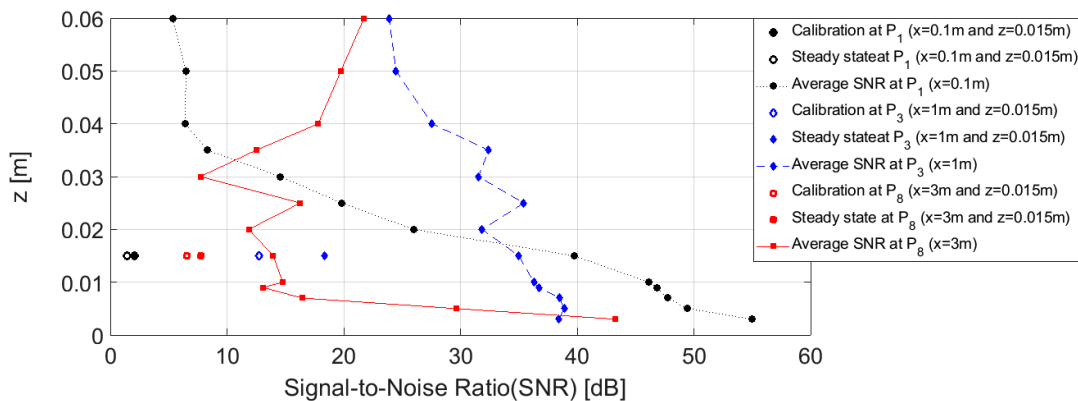


Figure 6-7. ADV Signal-to-Noise Ratio during the flow velocity measurements. The calibration measurement was done before the plume release and followed with steady-state measurement. After a steady state, the velocity profile is measured by a single point from  $z = 60$ mm). This figure is produced for Experiment  $S = 10^\circ$ ,  $H = 0.25$ m and  $SSC_0 = 20$ g/l.

As shown in Figure 6-6, the CFD model predicted less SSC, especially at further horizontal distances  $x$  from the impingement point. This inaccuracy can be explained first of by the fact that at these locations, the turbidity current was much diluted and the amount of sediment still in suspension is very low, hence out the Foslum sensitivity and accuracy range. Secondary, the difference can also be explained by the fact that

in the CFD model, the sediment was represented by a single median particle size ( $D_{50}$ ), hence the absence of finer particles that are easily transported in suspension to further distances. Part of the fine sediment in the particle distribution curve was missing in the CFD model. The last possible explanation is that during the laboratory experiments, sediment deposition was observed to be the dominant interaction between the plume and the seabed. The CFD model was setup in such way that erosion is ignored. When sediments reach the bed they were not allowed to come back into suspension. It means that if particles reach the seabed are counted as deposited particles and do not come back into the computation domain. As a consequence, even if locally the flow velocity would be capable to pick up already deposited sediments from the bed, it was not possible as erosion was switched off. Hence, a part of fine sediments are already counted as deposited when reached the bed in the vicinity of the impingement zone. Otherwise, the fine particle would be picked up and transported in suspension to further distances. This was different in laboratory experiments, although erosion was negligible compared to deposition, fine particles were allowed to be eroded and transported at the bed.

The explanation given in the above paragraph explains the reason why the plume reached further distances and more SSC was measured in the lab compared to the CFD predictions. Probably, the results would have been improved by using multiple sediment fractions in the numerical calculations or by switching on both deposition and erosion in the numerical model. However, this would also be costly due to increased CPU-time.

### **6.5.1. Turbidity underwater current flow velocity profile**

In comparison SSC and velocity profiles obtained in this research to the literature, specifically, the work of Sequeiros (2012), different flow regimes are observed in this research. Sequeiros (2012), used a Froude number approach to estimate the turbidity current flow conditions from channel morphology. The author gave characteristics of two typical gravity flow conditions, a case with supercritical and another one with subcritical gravity flow velocity and concentration profiles. In this research, similarly to Sequeiros (2012) profiles shapes are observed, it seems that the shape of the velocity profiles at  $x = 0.1\text{m}$ , shows characteristics of supercritical flows with the velocity peak located at an elevation  $z_p$  at about 0.3 times the current layer thickness  $h_c$  (meaning that  $z_p/h_c \sim 0.3$ ). These velocity profiles measured at  $x = 0.1\text{m}$  are steeper with positive slopes above the peak and have negative slopes below the peak. While at the distance  $x$  increases, the profiles steepness reduces at the same time the ratio  $z/h_c$  increases to around 0.5 leading subcritical velocity profiles characteristics, see for example Figure 6-6.

### **6.5.2. Turbidity underwater current SSC profile**

SSC profiles at  $x = 0.1\text{m}$  for plumes released at  $H = 1\text{m}$ , exhibit an inflection point slightly above the velocity peak and below the peak, the concentration can become uniform (see an example of SSC profile at  $x=0.1\text{m}$  in Figure 6-6). This is a characteristic of a typical SSC profile of subcritical turbidity current flow, also observed by Sequeiros (2012). In the present research, for considered boundary conditions at plume orifice, there is a clear link between the plume release height and the type of flow regime at the bed, a plume released at  $H = 1\text{m}$  impinged at the bed as plume-like impingement regime, hence it makes sense to observe subcritical flow regime after the impingement. This is also the reason why the flow allowed sediment particles deposition below the jet source and absence of a deposition ring discussed in section 5.2.4. On the other hand, for plumes released close to the bed,  $H = 0.25\text{m}$ , jet-like or transition impingement regimes were observed, hence supercritical flows regime inside the impingement zone. In this condition, the SSC profile may lack the inflection point and reach high concentrations near the bed. this can be seen in Figure 6-6 for profiles for  $H = 0.25\text{m}$  (third and four columns). This also explains that for a supercritical flow regime, the flow velocity was strong enough to push horizontally and transport all the sediment particles outside the supercritical zone which led to the formation of a deposition rings.

Another important observation is that while the flow velocity peak decreased with increasing distance  $x$ , in contrast, the time-averaged turbidity current thickness  $h_c$  increased respectively. The velocity profile thickness  $h_c$  shown in Figure 6-6 are higher at  $x = 0.5\text{m}$  compared to profile at  $x = 0.1\text{m}$ . In addition, due to gravity, the slope pulls the flow downstream leading to a faster, denser and thicker turbidity current flow.

## 6.6. Comparison for different initial plume conditions at the source

### 6.6.1. Effects due to changes in initial suspended sediment concentration

Figure 6-8 shows time-averaged flow velocity- and SSC profiles resulted from plumes released from  $H = 1$  m high above the bed. In this figure, the profiles comparison show clearly that denser plume, in this case with an initial  $SSC_0=20\text{g/l}$  accelerate and descends faster than the plume released at the same height but containing less initially  $SSC_0=10\text{g/l}$  and  $5\text{g/l}$ .

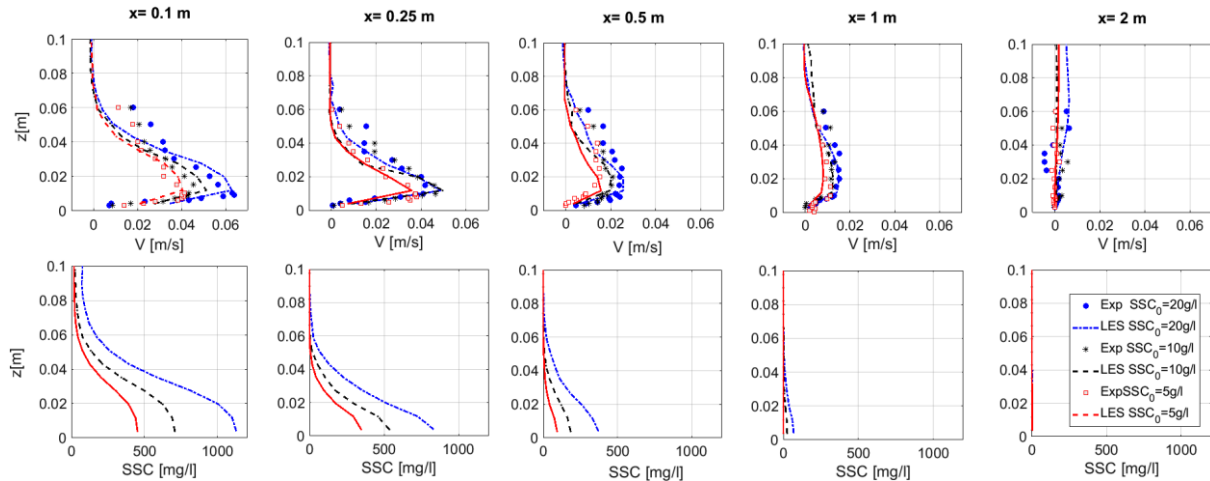


Figure 6-8 Comparison of the velocity and SSC profiles for turbidity current generated by plumes released at the same height ( $H=1\text{m}$ ) but containing different initial SSC (20 g/l, 10g/l, and 5g/l). Exp. on a horizontal bed.

The excess vertical acceleration for a dense plume eventually caused stronger impacts when the plume impinged on the bed leading to higher velocity turbidity currents. Also, profiles plotted in Figure 6-8 show that close to the impingement point, location  $x=0.1\text{m}$ , the peak flow velocity measured at elevation  $z=10\text{mm}$  was 30% higher for denser plumes  $SSC_0 = 20\text{g/l}$  compared to less dense plume for  $SSC_0 = 5\text{g/l}$  all released from the same height  $H = 1$  m. This difference was observed to be 40% for maximum SSC measured 3 mm above the bed. Because of high horizontal velocities in a dense flow mixture, resulting horizontal momentum makes the turbidity current to travel longer distances  $x$  compared to the less dense plume. However, in both cases, the turbidity current velocity reduced considerable after a distance  $x=2\text{m}$  and almost all particles had deposited at the bed.

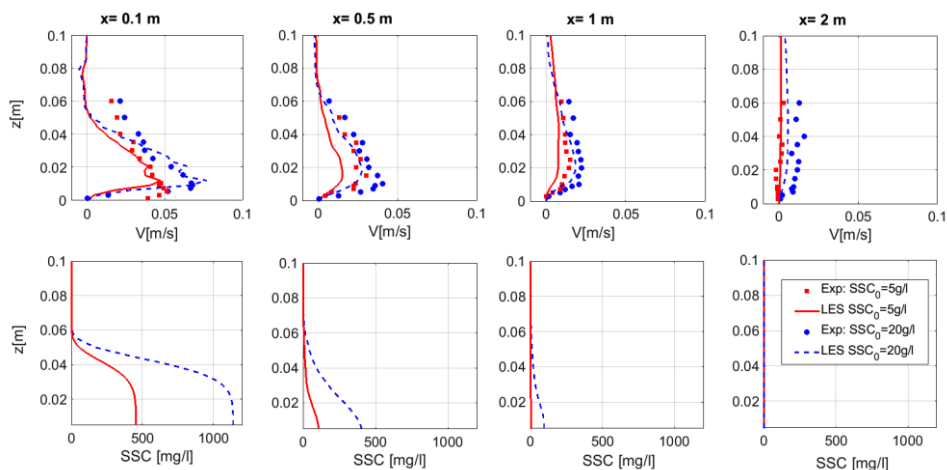


Figure 6-9 Comparison of the velocity and SSC profiles for turbidity current generated by plumes released at the same height ( $H=1\text{m}$ ) but containing different initial SSC (20 g/l and 5g/l). Impingement on  $10^\circ$  sloped bed.

Another observation is that both experiments and CFD results agreed that denser plumes generated thicker horizontal turbidity currents. The thickness  $h_c$  increases from the impingement point towards

further horizontal  $x$  distance. Observations stated in above paragraphs are the same for the plumes impinging on a sloped bed, see Figure 6-9. Dense plumes have stronger impacts on the bed and generated turbidity current after impingement are stronger compared to less dense plumes. It is also important to note that the differences are increased as an effect of the slope. The plume accelerates in the downslope direction.

### 6.6.2. Effects due to changes in the plume release heights from the bed

Results presented in Figure 6-10 show comparisons of experiments three different plume release height from the bed ( $H = 1\text{m}, 0.5\text{m},$  and  $0.25\text{m}$ ). CFD predictions for the turbidity current velocity and local SSC profiles at different locations  $x$  along the central  $x$ -axis are compared with laboratory data. Compared tests have the same initial suspended sediment concentration of  $SSC_0 = 20\text{g/l}$ .

Plumes released from  $H = 1\text{m}$  had a high falling distance leading to excess acceleration hence generated stronger turbidity currents. However, at the impingement point, the plume released at  $H = 1\text{m}$  has less horizontal velocity compared to release plume closer to the bed ( $H = 0.5\text{m}, 0.25$ ). This can be explained by the fact that due to a long falling distance, the plume entrains more ambient water and lose its momentum and buoyancy forces before it reaches the bed. The consequences are that the ratio  $Z^*/L_M$  increases considerably while buoyancy takes over momentum. The plume test with  $SSC_0 = 20\text{g/l}$  released from  $H = 1\text{m}$  hit the bed as a plume-like impingement, see Table 3-3. On the other hand, the plume released close to the bed, for instance,  $H = 0.25\text{m}$  with the same source sediment in suspension ( $SSC_0 = 20\text{g/l}$ ) reached the bed in a jet-like impingement regime, hence the low ratio  $Z^*/L_M$  and higher horizontal velocity at the impingement point. However, due to bed friction, the velocities reduce considerably after a short horizontal distance. Another explanation of the reduction of horizontal velocity for plumes released close to the bed is the deposition ring discussed in section 5.2.4. The ring located close to the impingement point ( $x \sim 0.1\text{m}$ ) and acts as a barrier for the horizontal flow after impingement, this lead to loss of the flow energy. This sediment ring barrier was not present for plume released from  $H = 1\text{m}$  hence no loss of energy due to the sediment ring. As result, the generated turbidity current has high flow velocities outside the impingement region for  $H = 1\text{m}$ .

It is also important to note that, when the plume was released at high elevation reached the bed with a large diameter (see Figure 4-1 and Table 4-1); this means that when the plume reached the bed, part of the plume has already traveled some distance in the horizontal direction from the impingement point. For example, the velocity and SSC profiles measured at location  $x = 0.1\text{m}$  were taken under the falling plume for  $H=1\text{m}$ . At this location, when the plume hits the bed its diameter was  $2b=0.1580\text{m} > 0.1\text{m}$ , hence the velocity and SSC profile measured close to IP at  $x=0.1\text{m}$  were taken under the falling part of the plume.

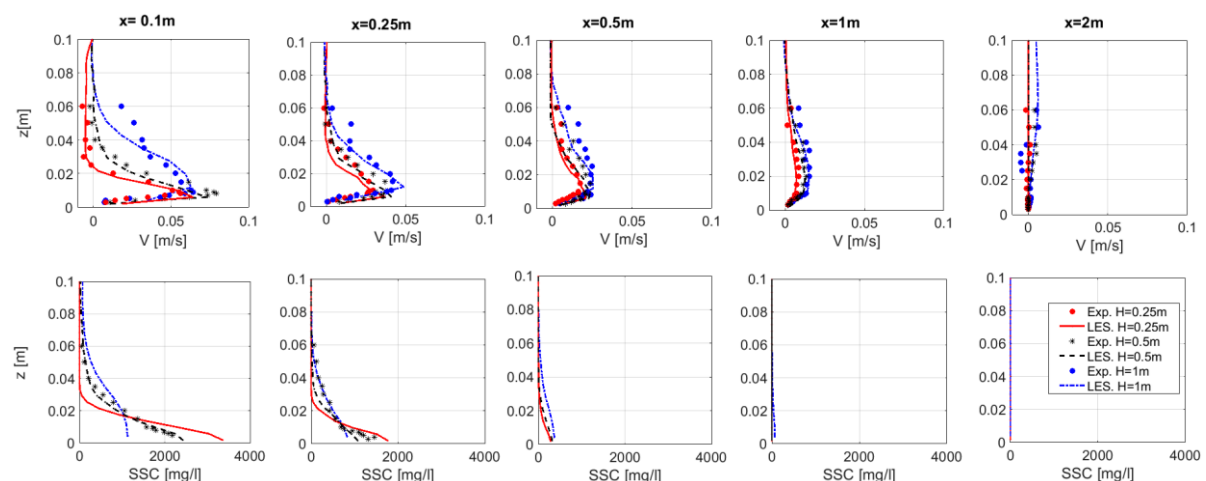


Figure 6-10 Comparison of the velocity and SSC profiles for turbidity current generated by a source of plumes with similar  $SSC_0 = 20\text{g/l}$  but released at different height  $H = 1\text{m}, 0.5\text{m}$  and  $0.25\text{m}$  from an a flarbed.

Figure 6-11 shows the same comparison as in Figure 6-10 but for tests done on a 10 degrees sloping bed. Due to the flow instability, as can be seen in this figure, the average flow velocity profile measured at

$x=0.1\text{m}$  resulted in a less smooth velocity profile closer to the bed due to the presence of the deposition ring. In Figure 5-9 that shows the deposition ring, it can be seen that at location point  $P_4$  ( $x = 0.1\text{m}$ ) was under the sedimenting during all tests with plume released at  $H=0.25\text{m}$  and  $H=0.5\text{m}$ . Velocity profiles at this location measured with a single point ADV, by starting from  $z = 60\text{ mm}$  from the bed downward, measurement closer to the bed were always taken after 30 minutes when the deposition ring had grown bigger. This means that low elevations,  $z < 10\text{ mm}$ , are measured with the bed referenced at  $z=0$  which was not the case anymore as the bed level changed with time due to the growing height of the deposition ring.

In Figure 6-10, it is observed that local SSC profile measured at locations ( $x > 25\text{ cm}$ ), shows more sediment in suspension for the test when the plume was released close to the bed ( $H = 0.25\text{m}$ ). An explanation for this is that when sediment plumes are discharged close to the bed, the flow doesn't have enough time and distance to entrain ambient water before it hits the bed. Hence compared to the case of plumes released at high elevation  $h=1\text{m}$ , the plume released close to the bed is less diluted at the impingement point. Inside the impingement zone, the horizontal flow velocity magnitude was till high and a turbulent flow. The effects are then that this region, all sediment particles are eroded and brought back into suspension, creating a sediment cloud, This can be seen in Figure 5-6. However, in this condition sediment particles were observed to rain out of the flow again and re-deposited just outside the deposition ring. The same observation were observed for the test with sloping bed, see the following Figure 6-11.

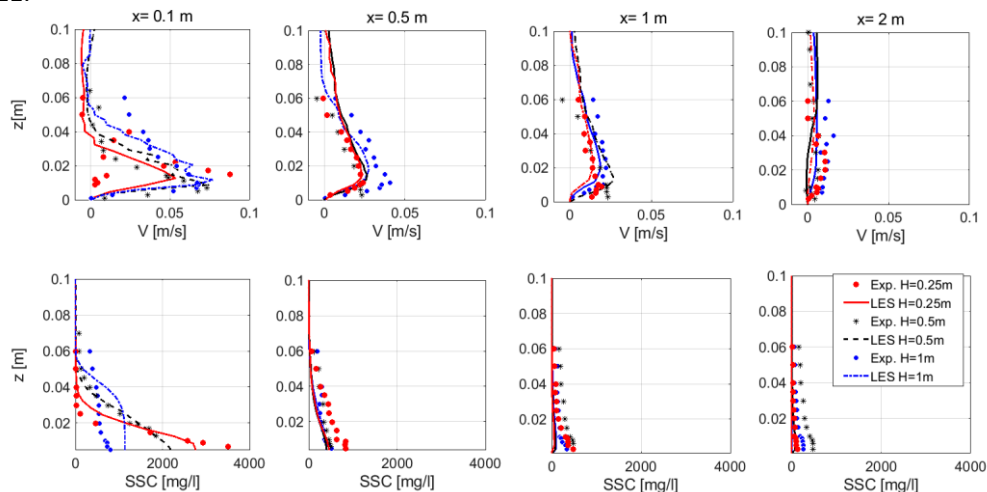


Figure 6-11. Comparison of the velocity and SSC profiles for turbidity current generated by a source of plumes with similar  $SSC_0 = 20\text{g/l}$  but released at different height  $H = 1\text{m}, 0.5\text{m}$  and  $0.25\text{m}$  from a  $10\text{ degrees}$  sloping bed.

SSC measurements and their CFD prediction plotted in Figure 6-10 and Figure 6-11 show high concentration near the bed and the turbidity current thickness  $h_c$  increases with increasing release height  $H$ . In addition, the turbidity current generated with plume release at  $H = 1\text{m}$  transported fine sediments to greater distances  $x$ . Although the falling height is the dominant parameter causing the acceleration of the turbidity current after the impingement causing the plume to reach further distances; it is also possible that due to dilution resulting from entrainment of ambient water in the falling plume, the fluid viscosity reduced inside the plume and therefore the current can travel faster. Using the equation of Thomas, (1965), the relative viscosity ( $\mu_r$ ) at the impingement point for an initial  $SSC_0=20\text{g/l}$  released at  $H=1\text{m}$  was  $\mu_r = 1.0034$  while for  $H=0.25\text{m}$ ,  $\mu_r = 1.0084$ . The difference between these relative viscosities of plumes released at different height is too low, hence it can be concluded that falling height is the dominant parameter influencing the flume dispersion rate.

### 6.6.3. Effects of the sloping seabed topography

The observations made during the experiments demonstrate conclusively that a turbidity current followed the impingement of a buoyant flow on a sloped bed disperse faster and is thicker (higher  $h_c$ ) compared to the one falling on a flatbed. See Figure 6-12 and Figure 6-13. The flow accelerated on the

sloping bed due to gravity, more ambient water was entrained and the turbidity current traveled faster transporting sediment into suspension to longer distances away from IP. Results presented in Figure 6-13 for a plume released from  $H=0.5\text{m}$  with  $SSC_0=20\text{ g/l}$  compared to the case where  $SSC_0$  was reduced to  $5\text{ g/l}$  (Figure 6-12) show that for 10 degrees sloped bed; the velocity of a turbidity current decreased modestly with reducing buoyancy at the source. The differences are observed clearly at  $x=2\text{m}$  where the flow velocity for a flatbed experiment became already zero.

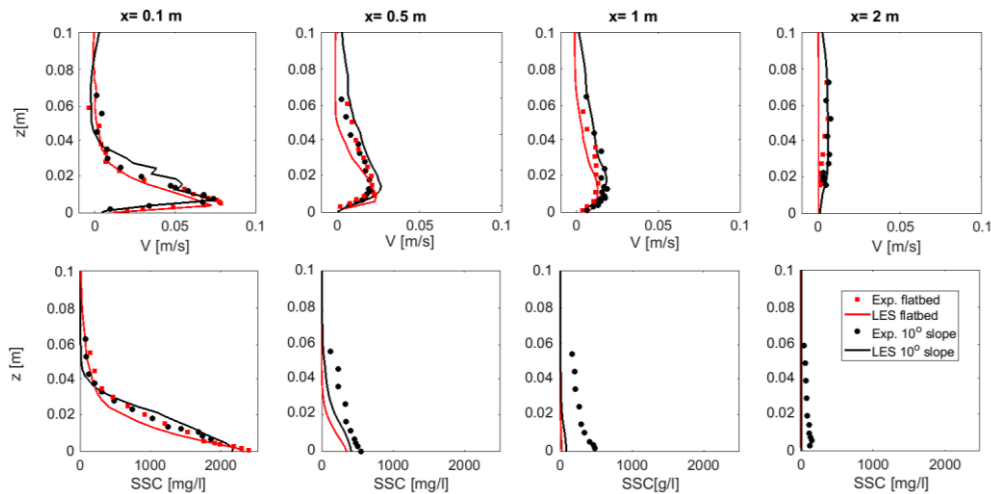


Figure 6-12 Effects of 10 degrees sloping bed during the experiment:  $H=0.5\text{m}$ ,  $SSC=20\text{g/l}$  compared to results with a flat table.

Visual observations, Figure 5-1, and average velocity profiles plotted in Figure 6-12 and Figure 6-13 show that the turbidity current thickness increases due to the presence of a slope. The laboratory measurement compared with CFD prediction is in a good agreement. The flow velocity was predicted accurately. Unfortunately, there was no SSC measurement during test on a flatbed and the measurement done on the sloping bed did not match well with the model prediction due to the same issues explained in section 6.6.2.

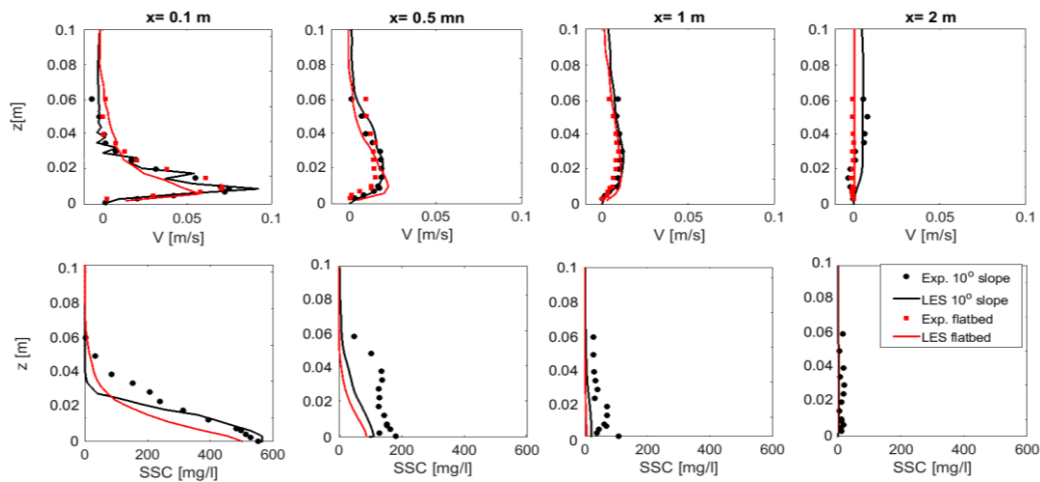


Figure 6-13 Effects of 10 degrees sloping bed. Experiment with  $H=0.5\text{m}$ ,  $SSC=5\text{g/l}$  compared to results with a flat table.

#### 6.6.4. Effects of a uniform ambient current on deep-sea mining plume dispersion

The motion of water, dissolved and suspended matter in the deep ocean is slower compared to surface water motion. The latter is largely driven by surface influences such as the modifications in the density of water near the surface, the direct action of wind and other meteorological factors (evaporation, rainfall or solar heating, etc.). Although deep near the bed, water motions are slower, they can be complex, three

dimensional and turbulent because of density stratification or complex bathymetry. These water motions complexities and the absence of current field measurements or observations make very difficult to find trustable data for the CFD model input.

During offshore mining operating, local currents and project-induced currents in combination with the changes in local bathymetry will probably have effects on the plume dispersion. There are chances that the return plumes and generated plumes from mining machines (spill) could be re-suspended due to currents. Re-suspension of sediment could negatively affect the benthic ecosystems as well as the mining operation itself; hence, it is too simplistic to ignore the effects of currents. In this research, based on a rough assumption, a uniform current equal to  $u_c = 0.1\text{m/s}$  in the field was modelled on a 1:50 scale in CFD model ( $u_c \text{ model}=0.014 \text{ m/s}$ ) to analyse what could be its effects of current on deep-sea mining plume dispersion.

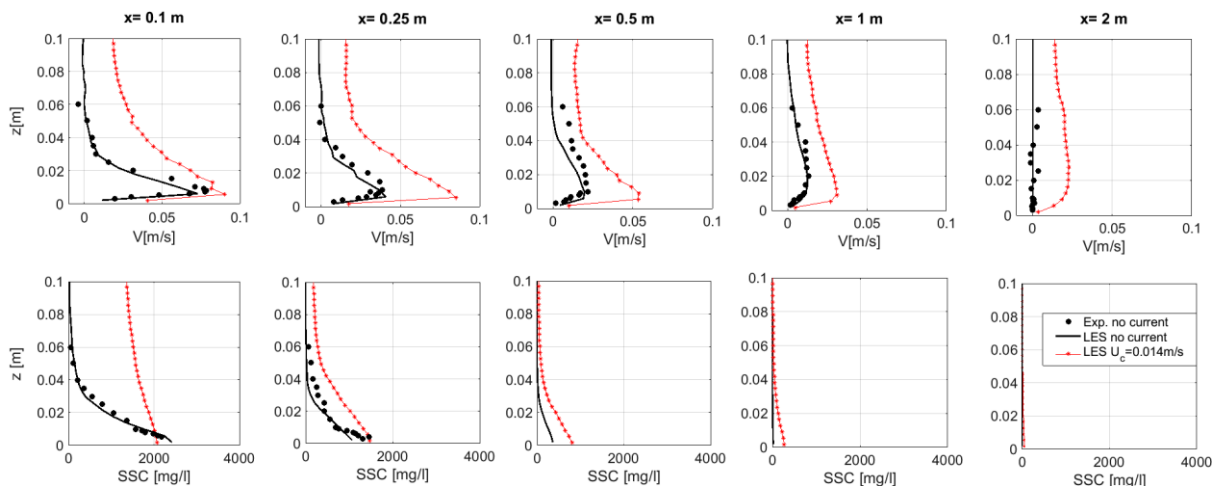


Figure 6-14 Effects of uniform current ( $u_c=0.014\text{m/s}$ ). Experiment/Run Flatbed  $H=0.5\text{m}$  and  $SSC_0=20 \text{ g/l}$ .

CFD Results in Figure 6-14 clearly show that the ambient current has significant effects on the dispersion and mixing of the DSM plume dispersion, high flow velocities are predicted compare to the case with no ambient current. As shown in Figure 6-15, a uniform ambient current deviates the plume and disperse it in the main direction of the ambient water current. Higher velocities in the ambient current were predicted and the sediment plumes dispersed to larger distances from the disposal location. In addition, ambient current will transport the sediment plume further away from the disposal location compared to the case of non-ambient currents.

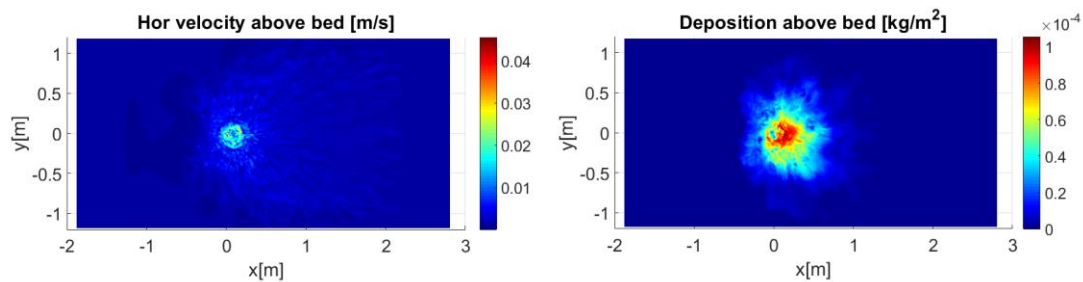


Figure 6-15 Two dimensional ( $x,y$ ) top views of CFD resulted horizontal velocity and and cumulative sediment deposition at the bed after 360s. Simulation of experiment with a flatbed,  $H=0.5\text{m}$ ,  $SSC_0=20\text{g/l}$  and uniform ambient current  $u_c=0.014\text{m/s}$ .

Figure 6-16 shows a comparison of plume spreading after 360 seconds. For simulations with the ambient current situation for a plume released at a height  $H=0.50\text{m}$  with initial  $SSC_0 = 20 \text{ g/l}$ , the model predicted that the sediments will be kept in suspension downstream in the ambient current direction compared to situations without ambient current. Furthermore, compared to the effects of the sloped bed that the turbidity current to accelerate in the downslope direction, leading to plume current that travels a greater distance from the disposal location, the sediments inside the turbidity current is transported and stay

closer to the seabed. On the other hand, compared to the case with the ambient current, sediment clouds can be seen higher up in the water column, see Figure 6-12.

The CFD model simulation results in above Figure 6-14 show that at a distance  $x=1\text{m}$  from the impingement point, the suspended sediment profile shows that results obtained with no ambient current, the concentration of suspended particles reduced considerably to almost zero. In the presence of ambient current similar SSC profile is obtained at a double distance ( $x=2\text{m}$ ). At the same distance of  $x=2\text{m}$ , the velocity profile was still quite high due to ambient current. Lees sediments while there is still high velocity can be explained by the fact that, in the CFD model, sediment was represented by a single sediment fraction with  $D_{50}=36$  microns, hence there was more deposition that is in reality within the domain  $x<2\text{m}$ . Finer particles that could have been transported to further distances are missing in the CFD model. Also, in the CFD model particles that reached the bed are counted as deposition and were not allowed to come back in the computational domain, hence predicted SSC profile at  $x=2\text{m}$  shows less SSC. An important conclusion to this end is that apparently the effects of ambient current cannot fully be predicted well with a near-field model with on sediment fraction. To predict accurately the effects of ambient current, one should consider more sediment fractions and a far-field model is needed to also put the focus on what happens kilometers farther away from the disposal location.

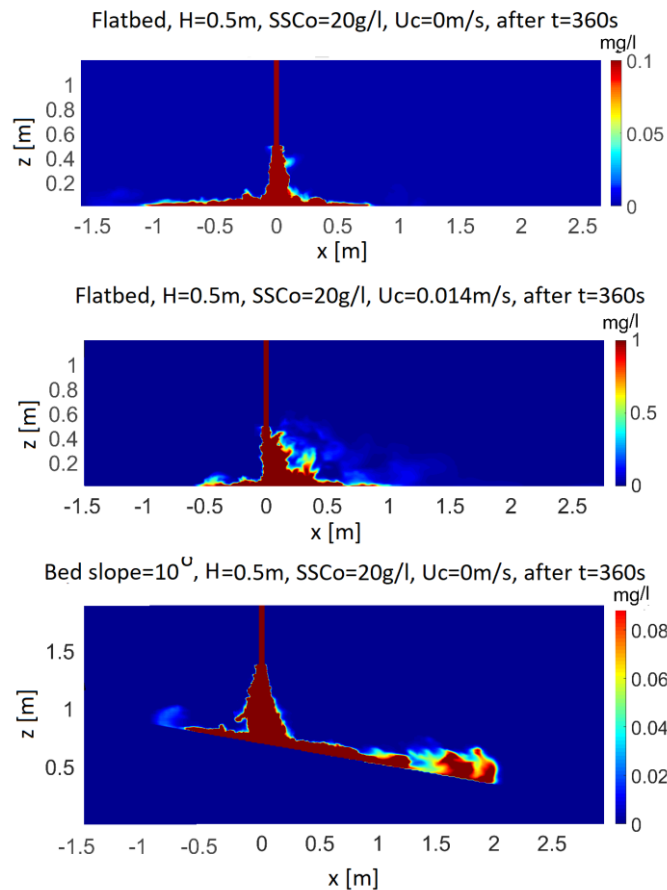


Figure 6-16 LES simulation results in comparison to different input parameters. Center slices images of 360s plumes spreading ( $H=0.5\text{ m}$  and  $SSC_0=20\text{ g/l}$ ). Flatbed without ambient current(top), flatbed and ambient current (middle) and  $10^\circ$  sloped bed without ambient current(bottom). It is reminded to the reader that the effects of ambient current were not included in the laboratory experiments.

## CHAPTER 7

# Conclusions and recommendations

---

Introduced goals of this research were to provide on a laboratory scale, a unique set of validation data for numerical models and to run several large eddy CFD simulations to predict the near-field spreading of DSM plumes. Results obtained give a valuable insight to a comprehensive investigation on the propagation and dynamics of plumes as turbidity currents. Plumes generated from DSM activities were studied using noncohesive particle-laden flows on a laboratory scale and a drift-flux CFD model with LES running the same conditions as in the experiments. It is important to mention that these results are based on scaled simulations in the laboratory and numerically. Full field-scale results could deviate, hence similar work should be done but in the Field.

Three-dimensional information data on the flow velocities suspended sediments concentrations, local plume path and dilution on a laboratory scale is now available to be used by other researchers to validate their numerical models. Over a wide range of initial parameters, CFD analysis is done for the sediment-water mixture released at a constant flow rate from a submerged vertically downward pipe into a uniform body of water. Observed flow characteristics and physical phenomenon for formed underflows after the impingement of the negatively buoyant plume on the horizontal bottom and sloped bottom are presented in Chapters 5 and 6.

Plumes release height from the bed was found to be an important parameter. Releasing plumes closer to the bed leads to the formation of a circular levee around the impingement point. Consequently, the levee, which is a form of a sedimentation ring, acts as a barrier against the turbidity current leading to the deposition of sediments on the bed just outside the ring. Therefore, the presence of a barrier reduced the plume dispersion rate thus returned DSM wastes stayed closer to the disposal location. The presence of a deposition levee is related to the source fluxes and the type of impingements, which is also highly dependent and linked to the plume falling distance from the bed. Based on observed impingement flow regimes and seabed morphology changes, it is concluded that erosion and deposition cannot be neglected under jet-like impingements conditions. In addition, it is concluded that these plume interactions with the seabed should be considered within numerical models even for simplified laboratory experiments without a pre-existing bed.

Based on detailed analysis of obtained results considering simulations for a wide variety of initial flow cases, accurate results are obtained and the following conclusions and recommendations are made:

### 7.1. Conclusions

- Releasing the plumes at a higher elevation in the water column from the seabed will increase the effects of environmental pressures due to turbidity currents with higher velocities at the bed, but

a reduced release height will also reduce the amount of suspended sediments concentration and therefore the effect of siltation in the near-field region.

- Releasing the plumes near the seabed does show slightly better results as the plume stays closer to the disposal locations. However, deposition is increased inside the impingement region, which leads to changes in siltation hence effect of high-pressure smothering.
- Reducing the amount of suspended sediments flux at the tailings source has a higher benefit for the pressures reduction when the plume hit the bed and leads to less siltation.
- It was observed that due to an ambient current, particle settlement is limited. As an effect, sediment clouds are kept in the water column and transport in suspension far from the disposal location and in the same direction of the local ambient currents.
- The TUDflow3D LES CFD model is found to be fast and efficient in terms of computational time and is capable to accurately predict the near-field spreading of the Deep-sea mining plumes.

## 7.2. Recommendations

A set valuable laboratory measurements data is given and a 3D CFD LES model is tested and found to give good predictions on the studied flow conditions in this research. Results obtained give valuable insights in near-field DSM plume mixing. Therefore, a first recommendation is to use the provided laboratory data to validate numerical models. For similar cases to the ones studied in the present research, it is recommended to use LES models rather than heavy computational models like DNS. TUDflow3d LES model used in this research is approved to be a faster and an accurate tool. Therefore, this specific CFD model is recommended to be used in support of the environmental licensing process of DSM activities. Based on assumptions made and obtained during the research, additional recommendations are the following:

- It is recommended that DSM sediment waste and other effluents should be released closer to the seabed and initial suspended sediment concentration at the source should be kept low.
- In order to reduce the velocity at the seabed, which is to prevent re-suspension of already deposited sediments, it is advised to release DMS waste via multiple pipes in a form of diffusers.
- Further study including real sea-bed sediments to capture the possibility of re-suspension of already deposited sea-bed sediments.
- The far-field study is needed to be coupled with the present near-field model counting for sediments plumes created by mining activities, sediments spilling as well as the natural sediments plume. In addition, the far-field model would better predict the effects of the ambient current.
- Based on observed seabed morphology changes, it is recommended that erosion should be considered within numerical models to predict the interactions between DSM plumes with the seabed topography even for simplified laboratory experiments without a pre-existing bed. As there is a limited literature on this topic, it is recommended that future work should also focus more on the plume interaction with the bed.
- It is recommended to study impacts of more pressures due to DSM activities such as the cutting machines movements, substrate loss, underwater sounds, smothering of the seabed, changes in the background siltation, among others.

# Reference

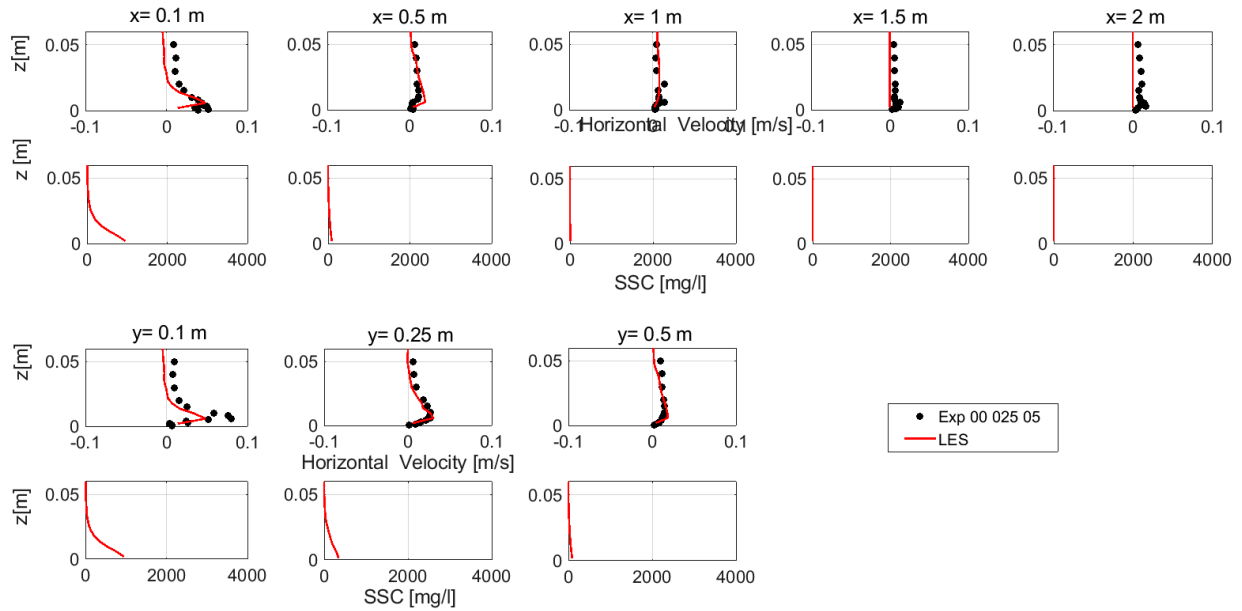
- Browning, D. S. (1968). Exploitation of Submarine Mineral Resources Beyond the Continental Shelf. *Tex. Int'l LF*, 4, 1.
- Christodoulou, G., Nikiforakis, I., Diamantis, T., & Stamou, A. (2016). Near-field dilution of a vertical dense jet impinging on a solid boundary. *Desalination and Water Treatment*, 57(11), 4898-4905.
- Chu, P. C., Lee, J. H., & Chu, V. H. (1999). Spreading of turbulent round jet in coflow. *Journal of Hydraulic Engineering*, 125(2), 193-204.
- Cooper, P., & Hunt, G. R. (2007). Impinging axisymmetric turbulent fountains. *Physics of Fluids*, 19(11), 117101.
- Corliss, B. H. (1985). Microhabitats of benthic foraminifera within deep-sea sediments. *Nature*, 314(6010), 435-438.
- Dai, Z., Tseng, L.-K., & Faeth, G. (1994). Structure of round, fully developed, buoyant turbulent plumes. *Journal of Heat Transfer*, 116(2), 409-417.
- Dai, Z., Tseng, L., & Faeth, G. (1995). Velocity statistics of round, fully developed, buoyant turbulent plumes. *Transactions of the ASME-C-Journal of Heat Transfer*, 117(1), 138-145.
- Darbyshire, A., & Mullin, T. (1995). Transition to turbulence in constant-mass-flux pipe flow. *Journal of Fluid mechanics*, 289, 83-114.
- Fernando H. J. S., S. S., Tobias Bleninger, Robert Doneker. (2013). Handbook of environmental fluid dynamics, Volume one: Overview and fundamentals. *CRC Press.*, 1.
- Garcia, M. H. (1994). Depositional turbidity currents laden with poorly sorted sediment. *Journal of Hydraulic Engineering*, 120(11), 1240-1263.
- García, M. H. (1993). Hydraulic jumps in sediment-driven bottom currents. *Journal of Hydraulic Engineering*, 119(10), 1094-1117.
- Glasby, G. (2000). Lessons learned from deep-sea mining. *Science*, 289(5479), 551-553.
- Hogg, A. J., Hallworth, M. A., & Huppert, H. E. (2005). On gravity currents driven by constant fluxes of saline and particle-laden fluid in the presence of a uniform flow. *Journal of Fluid mechanics*, 539, 349-385.
- Hunt, G., & Kaye, N. (2001). Virtual origin correction for lazy turbulent plumes. *Journal of Fluid mechanics*, 435, 377-396.
- Jirka, G. H. (2004). Integral model for turbulent buoyant jets in unbounded stratified flows. Part I: Single round jet. *Environmental Fluid Mechanics*, 4(1), 1-56.
- Kaye, N., & Hunt, G. (2007). Overturning in a filling box. *Journal of Fluid mechanics*, 576, 297-323.
- Krausmann, F., Gingrich, S., Eisenmenger, N., Erb, K.-H., Haberl, H., & Fischer-Kowalski, M. (2009). Growth in global materials use, GDP and population during the 20th century. *Ecological Economics*, 68(10), 2696-2705.
- Lee, J. H.-w., & Chu, V. (2003). *Turbulent jets and plumes: a Lagrangian approach*: Springer Science & Business Media.
- Lipari, G., & Stansby, P. K. (2011). Review of experimental data on incompressible turbulent round jets. *Flow, turbulence and combustion*, 87(1), 79-114.
- Morton, B. (1959). Forced plumes. *Journal of Fluid mechanics*, 5(1), 151-163.
- Morton, B., Taylor, G., & Turner, J. (1956). *Turbulent gravitational convection from maintained and instantaneous sources*. Paper presented at the Proceedings of the Royal Society of London A: Mathematical, physical and engineering sciences.
- Panchapakesan, N., & Lumley, J. (1993). Turbulence measurements in axisymmetric jets of air and helium. Part 1. Air jet. *Journal of Fluid mechanics*, 246, 197-223.
- Papanicolaou, P. N., & List, E. J. (1988). Investigations of round vertical turbulent buoyant jets. *Journal of Fluid mechanics*, 195, 341-391.
- Petersen, S. (2014). Marine Mineral Resources. *Encyclopedia of Marine Geosciences*, 1-9.
- Schriever, G., & Thiel, H. (2013). *Tailings and their disposal in deep-sea mining*. Paper presented at the Tenth ISOPE Ocean Mining and Gas Hydrates Symposium.
- Van Den Bremer, T., & Hunt, G. (2010). Universal solutions for Boussinesq and non-Boussinesq plumes. *Journal of Fluid Mechanics*, 644, 165-192.
- van Grunsven, F., Keetels, G., & van Rhee, C. (2016a). MODELING OFFSHORE MINING TURBIDITY SOURCES.
- van Grunsven, F., Keetels, G., & van Rhee, C. (2016b). Modeling offshore mining turbidity sources. *WODCON XXI: Innovations in dredging*.

- Welling, C. G. (1981). *An advanced design deep sea mining system*. Paper presented at the Offshore Technology Conference.
- Wilkinson, D., & Wood, I. (1971). A rapidly varied flow phenomenon in a two-layer flow. *Journal of Fluid mechanics*, 47(2), 241-256.
- Wood, M. C. (1999). International seabed authority: the first four years. *Max Planck UN Yearbook*, 3, 183.
- Wu, R., Geng, Y., & Liu, W. (2017). Trends of natural resource footprints in the BRIC (Brazil, Russia, India and China) countries. *Journal of Cleaner Production*, 142, 775-782.

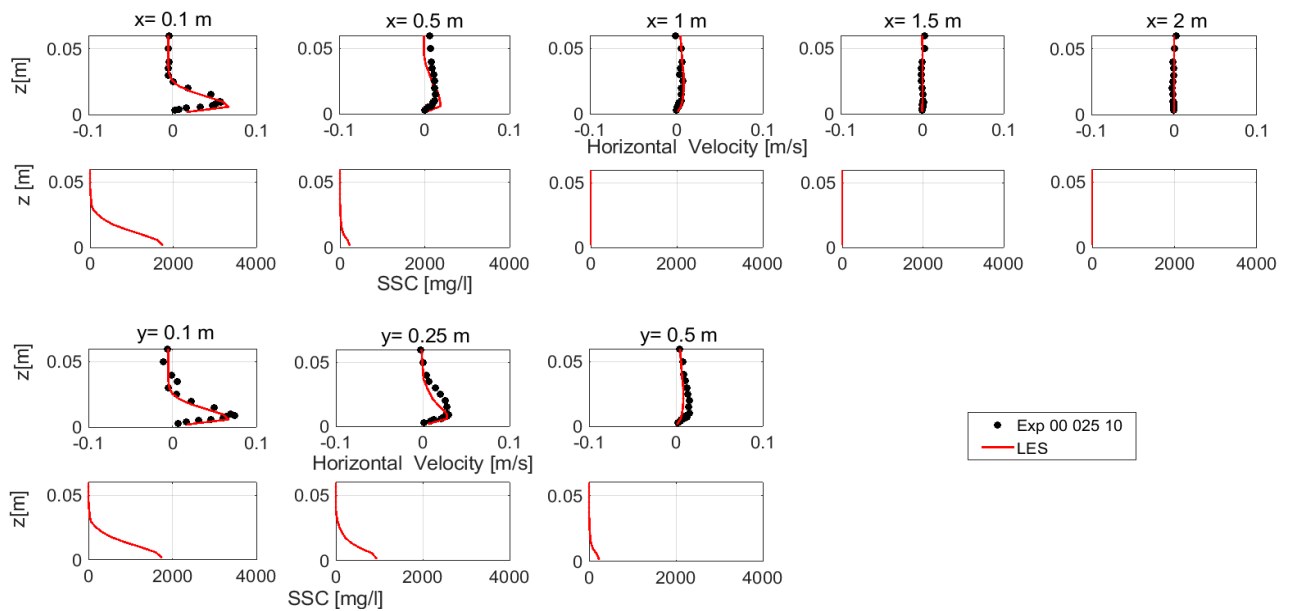
# Appendices

# APPENDIX A. Average flow velocity and SSC profiles

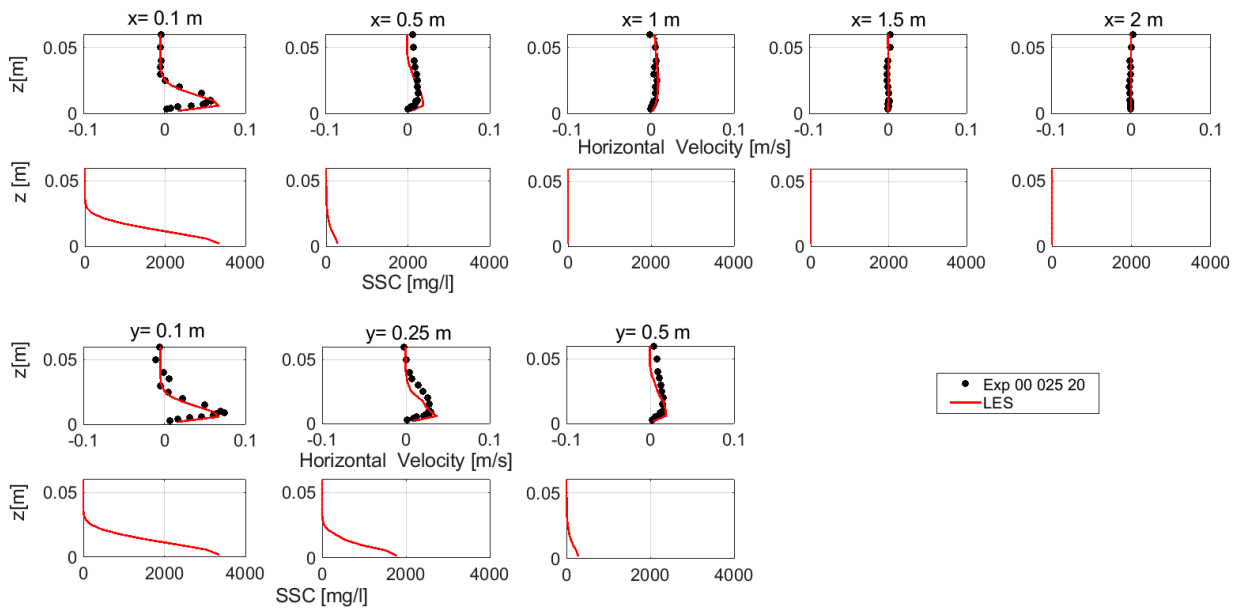
**Experiment: Flatbed, H=0.25m SSC<sub>0</sub>= 5g/l**



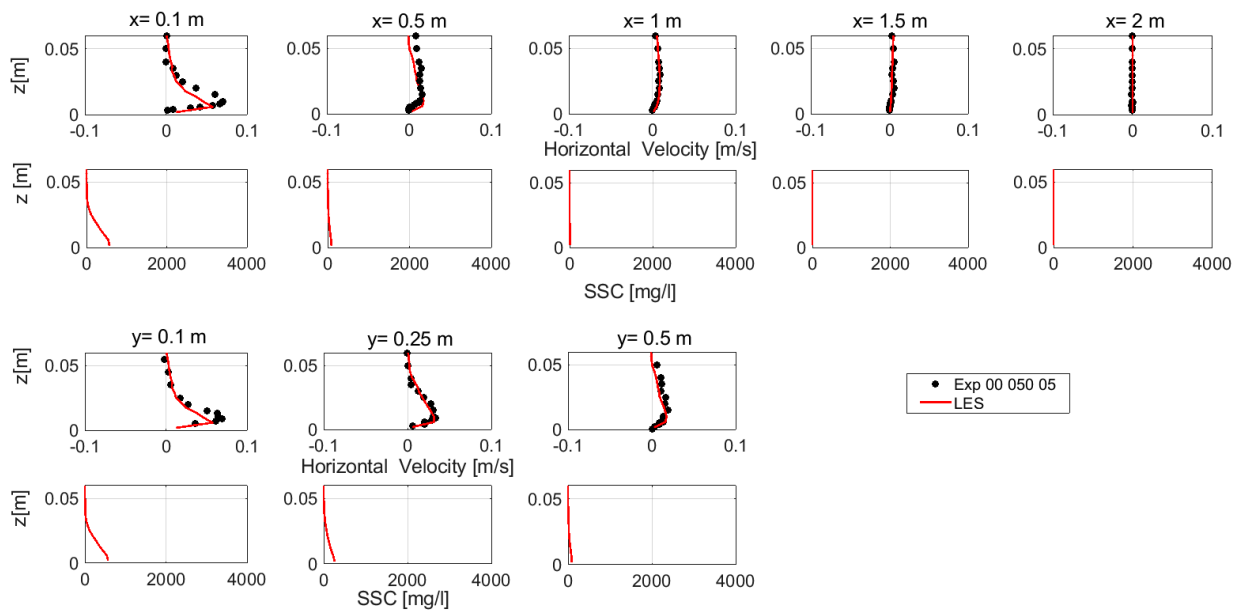
**Experiment: Flatbed, H=0.25 m SSC<sub>0</sub>=10 g/l**



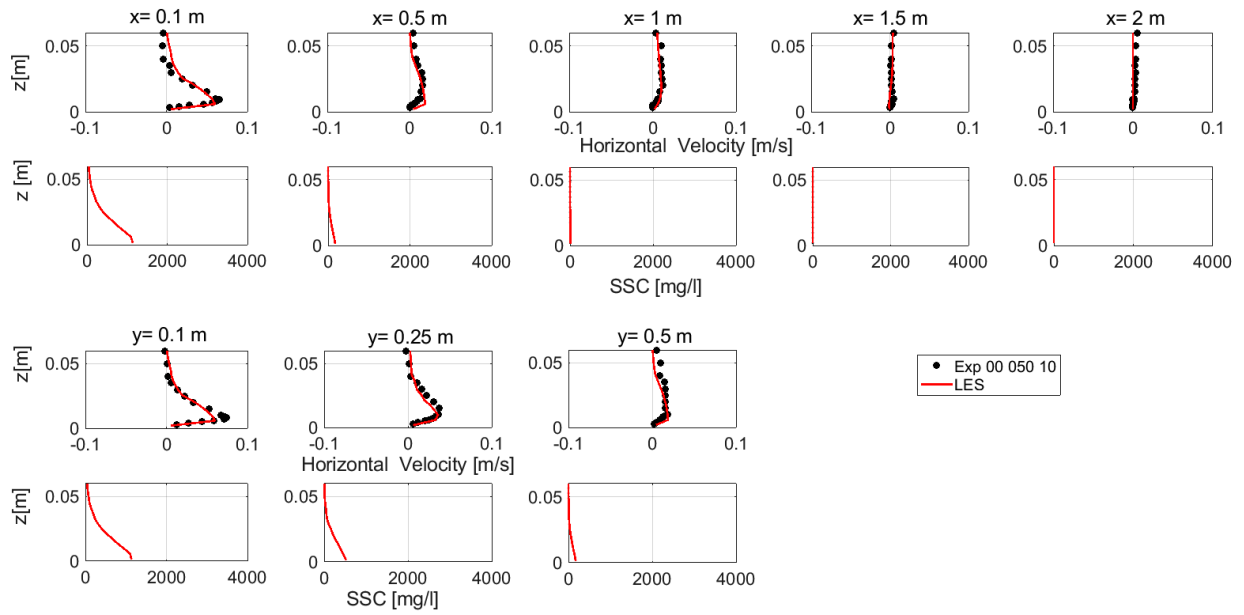
**Experiment: Flatbed, H=0.25 m SSC<sub>0</sub>=20 g/l**



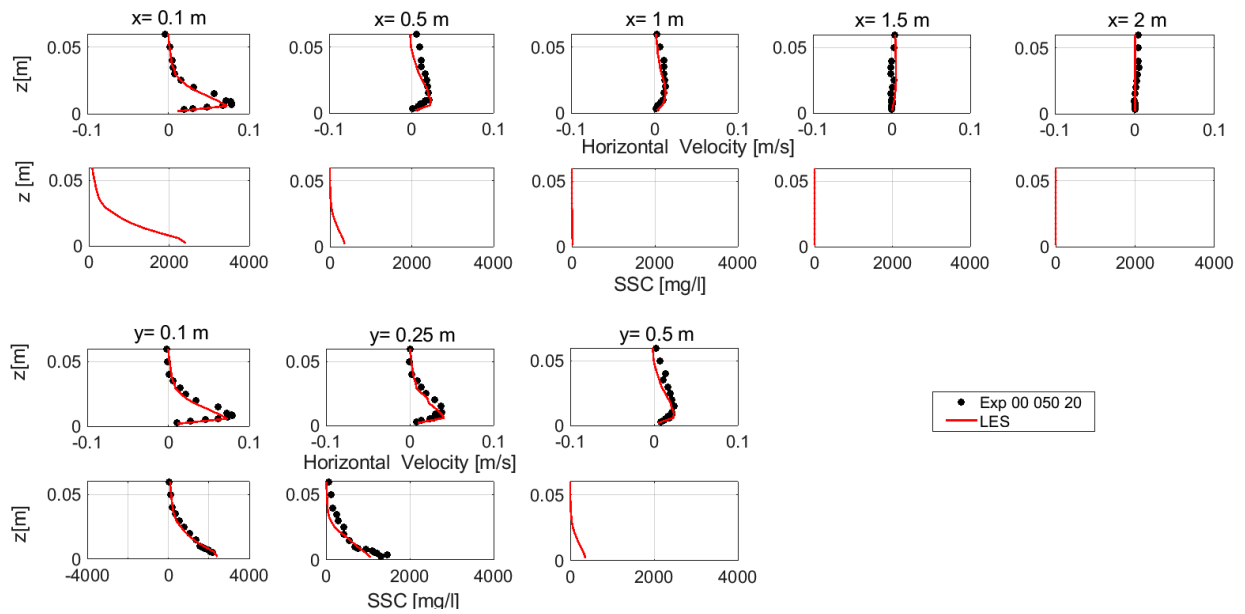
**Experiment: Flatbed, H=0.5 m SSC<sub>0</sub>=5g/l**



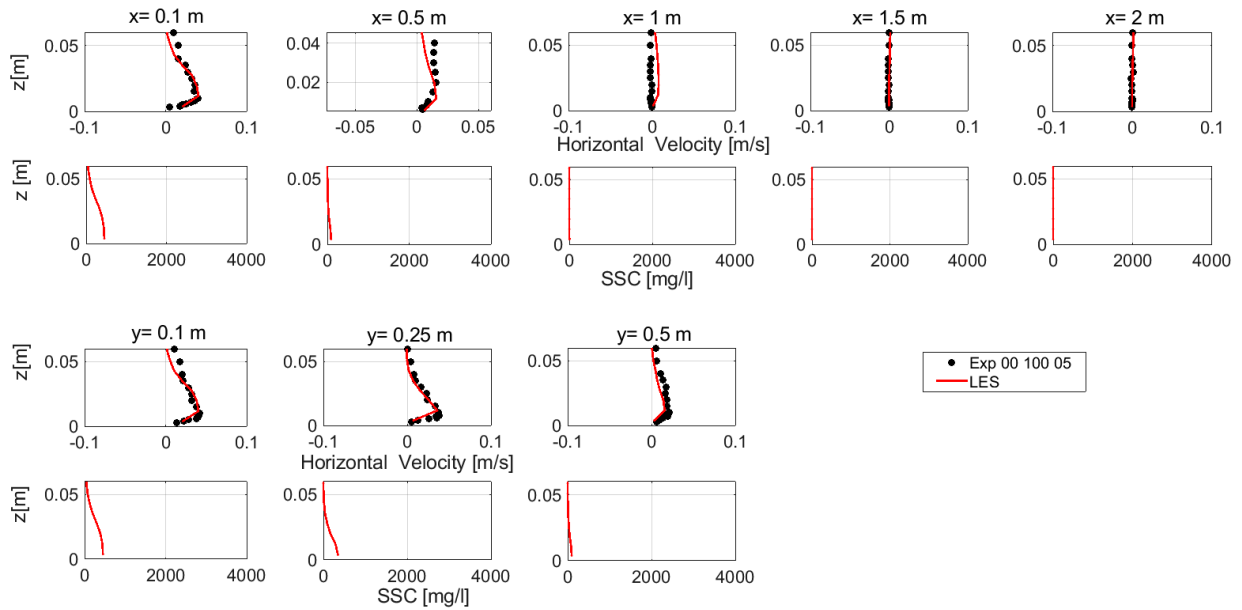
**Experiment: Flatbed, H=0.5 m  $SSC_0=10$  g/l**



**Experiment: Flatbed, H=0.5 m  $SSC_0=20$  g/l**



**Experiment: Flatbed, H=1 m  $SSC_0=5$  g/l**



**Experiment: Flatbed, H=1 m  $SSC_0=10$  g/l**

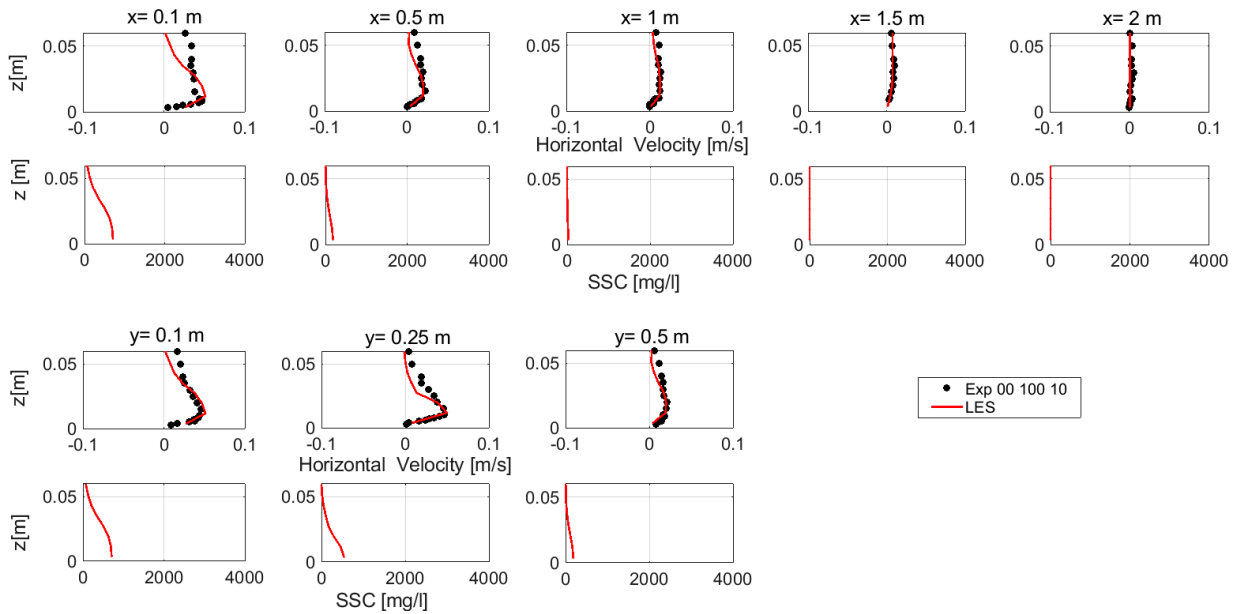
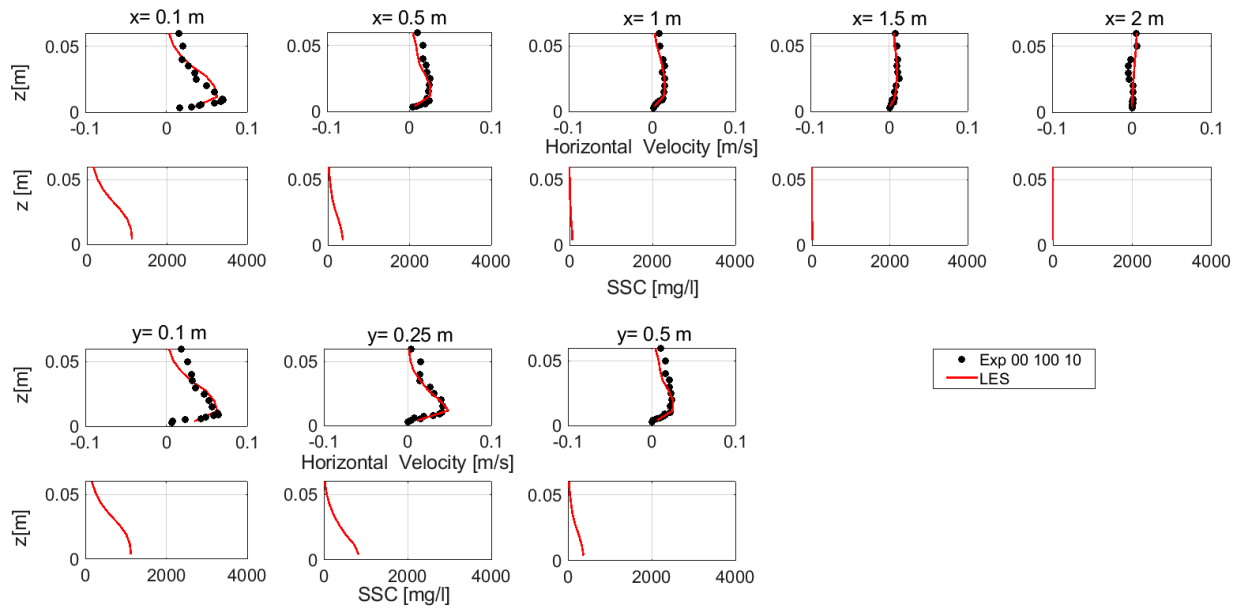
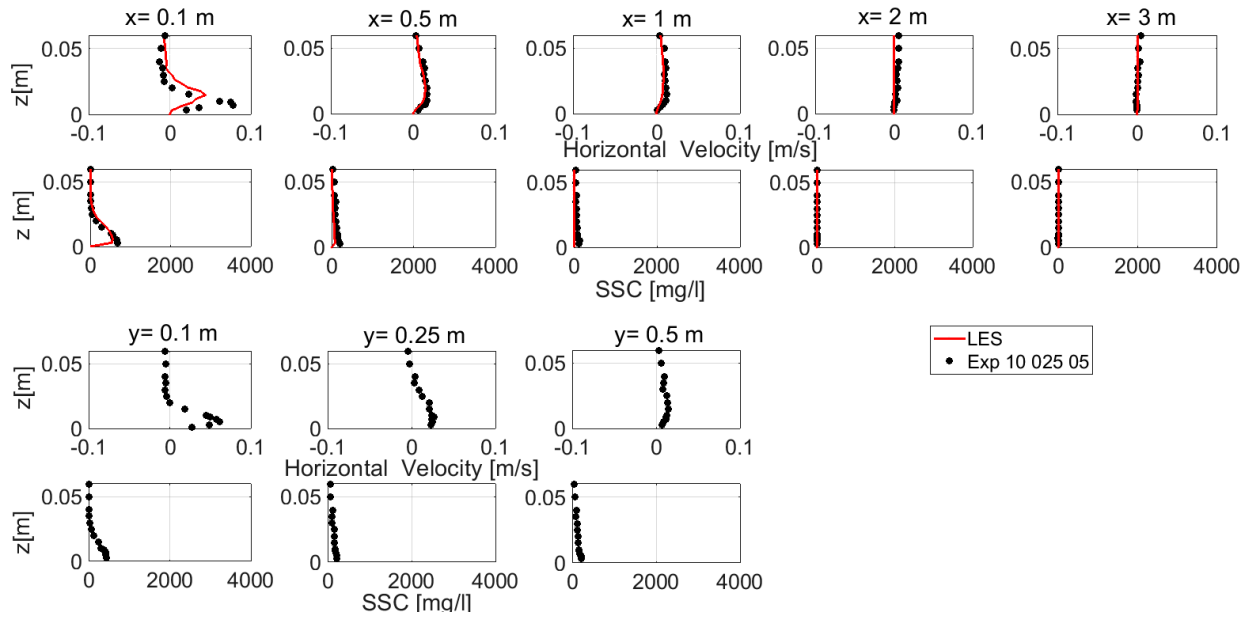


Figure 0-1 Average and SSC profiles for experimrnt serie A (Flatbed, slope= $0^\circ$ )

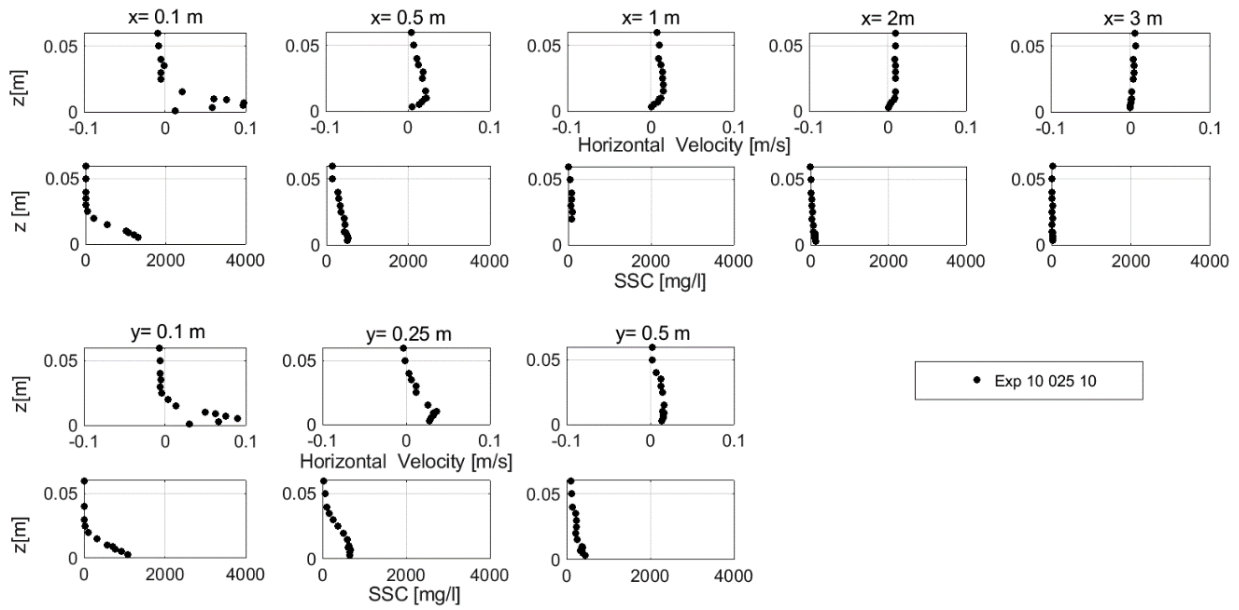
**Experiment: Flatbed, H=1 m SSC<sub>0</sub>=20 g/l**



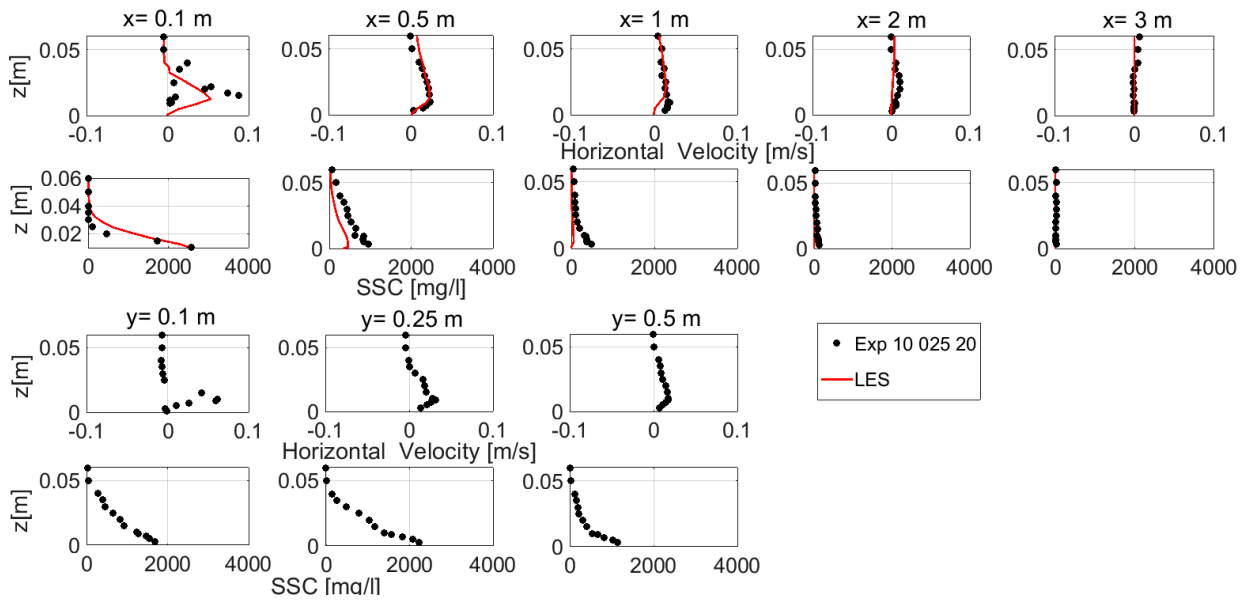
**Experiment: S=10 degrees, H=0.25 m SSC<sub>0</sub>=5 g/l**



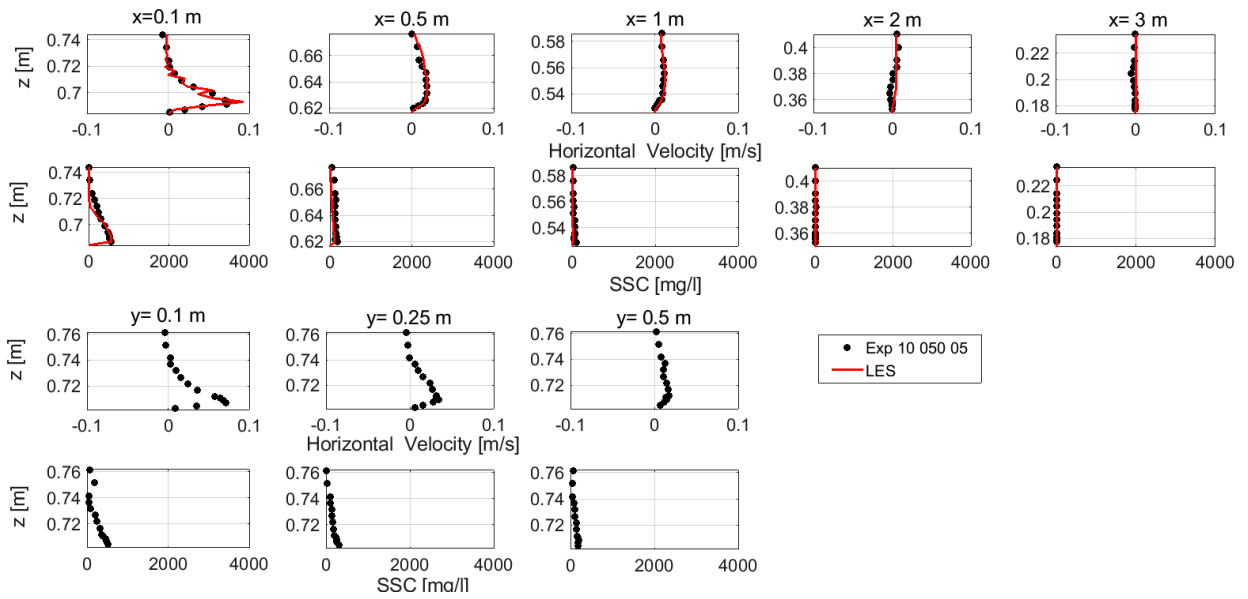
**Experiment:  $S=10$  degrees,  $H=0.25$  m  $SSC_0=10$  g/l**



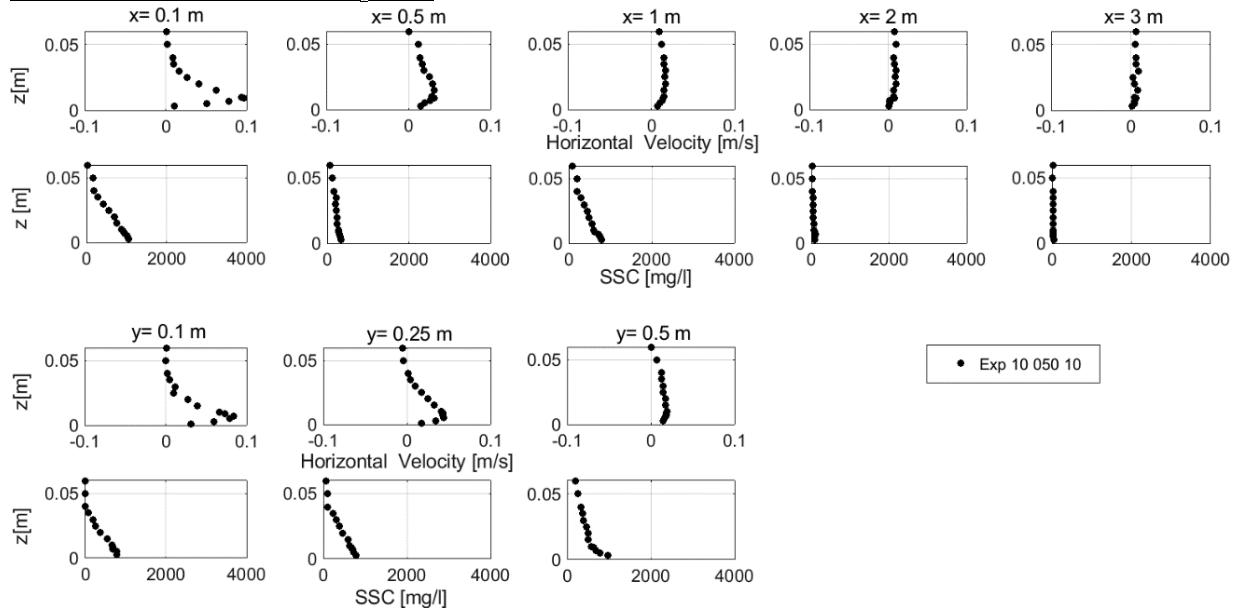
**Experiment:  $S=10$  degrees,  $H=0.25$  m  $SSC_0=20$  g/l**



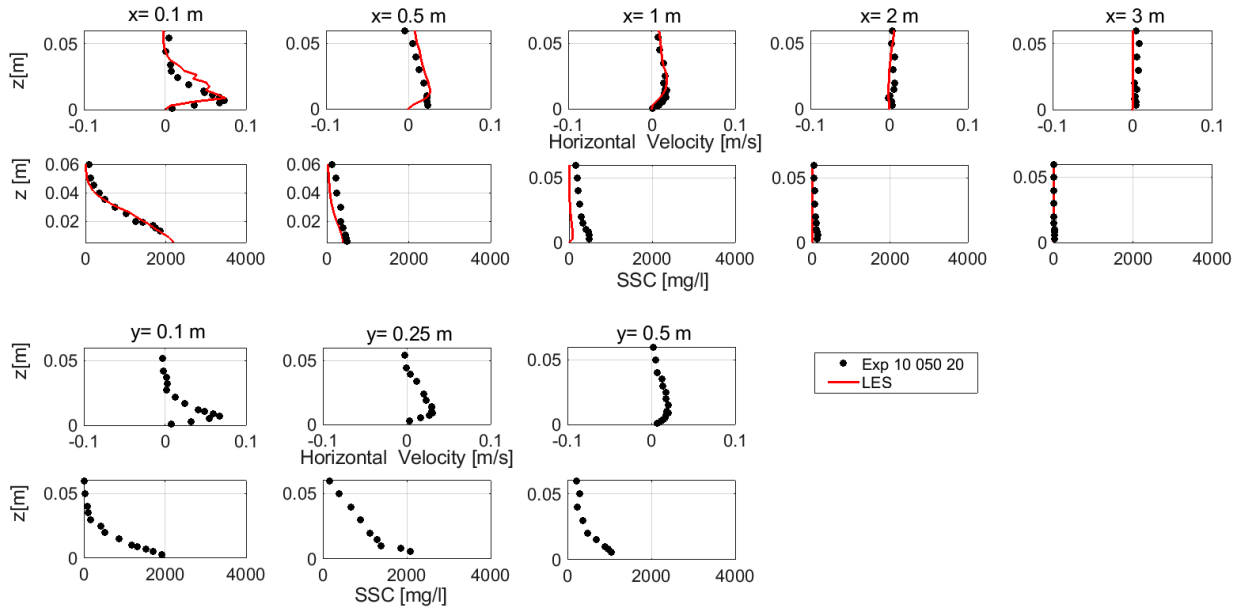
**Experiment: S=10 degrees, H=0.5 m SSC<sub>0</sub>=5 g/l**



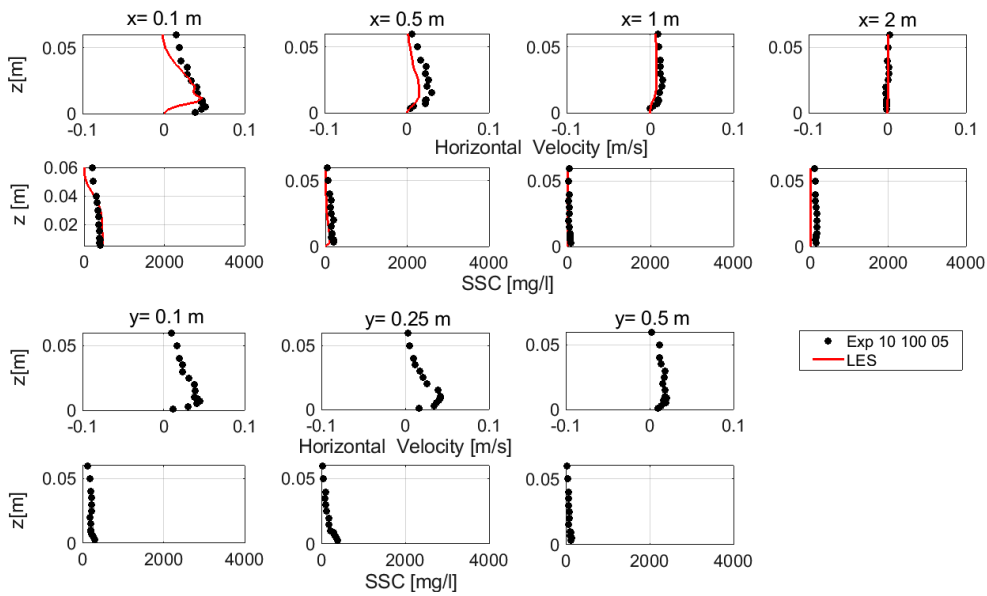
**Experiment: S=10 degrees, H=0.5 m SSC<sub>0</sub>=10 g/l**



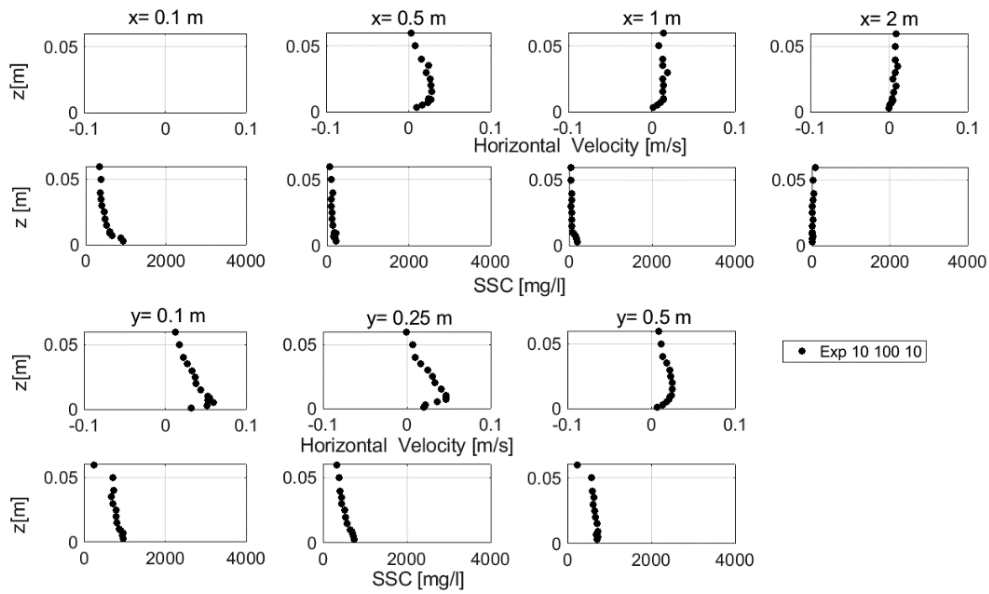
**Experiment: S=10 degrees, H=0.5 m SSC<sub>0</sub>=20 g/l**



**Experiment: S=10 degrees, H=1 m SSC<sub>0</sub>=5 g/l**



**Experiment: S=10 degrees, H=1 m SSC<sub>0</sub>=10 g/l**



**Experiment: S=10 degrees, H=1 m SSC<sub>0</sub>=20 g/l**

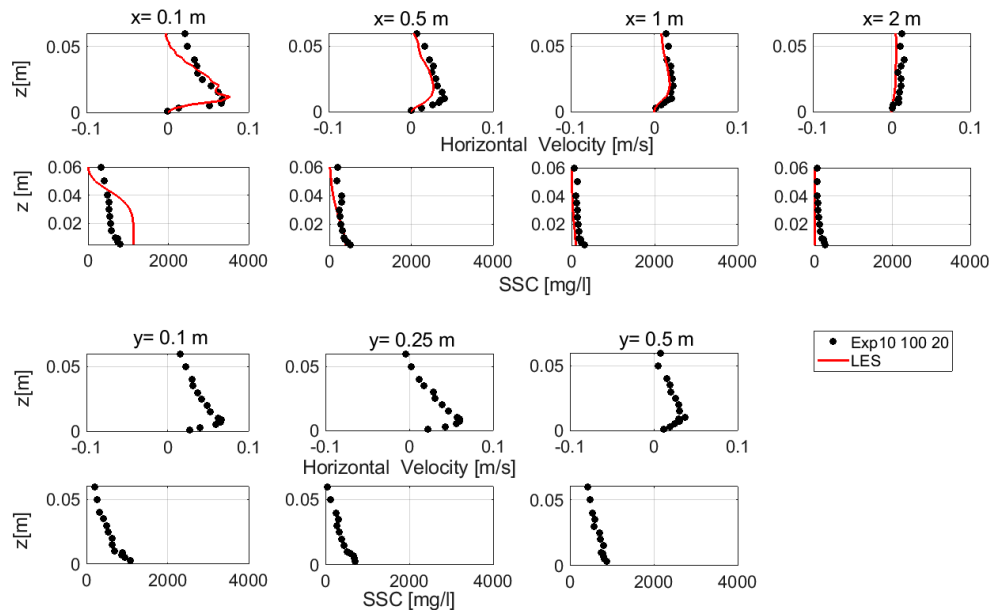


Figure 0-2 Average and SSC profiles for experimrnt serie B (slope=10°).

## APPENDIX B. ADV flow velocity and SNR measurements

The Acoustic Doppler Velocimeter is based on the Doppler principle. First, a short acoustic pulse of known frequency is transmitted along the vertical axis. The echo from the water is received in three small transducer elements, amplified in the conditioning module and digitized/analysed in the processing board. The frequency shift between the transmit pulse and the received echo is proportional to the water velocity. To ensure proper operation, the echo must be strong enough to allow proper calculation of the frequency shift. If the echo is weak, the calculation will be statistically "noisy" and the velocity data will show significant short-term variability leading to inaccuracy in the measured velocity. The strength of the echo is quantified in terms of a "signal-to-noise ratio" (SNR) expressed in dB and displayed for each receiving beam in the upper part of the data collection display. When collecting raw data (e.g. at 25 Hz), we recommend a SNR that is consistently above 15 dB.

Figure B-0-1 shows the average signal-to-noise ratio profiles measured at  $x=0.1m$ ,  $x=1m$  and  $3m$  for Experiment  $S=10$  degrees,  $H=0.25M$  AND  $ssc_0=20g/l$ . the flow velocity and SNR times series were measured for experiment  $S=10^0$ ,  $H=0.25m$ , and  $SSC_0=20g/l$ . Whenever the SNR is below 15 dB, the accuracy of the flow velocity is questionable and leads to inaccuracy as shown in the velocity profiles presented in 6.2.2.

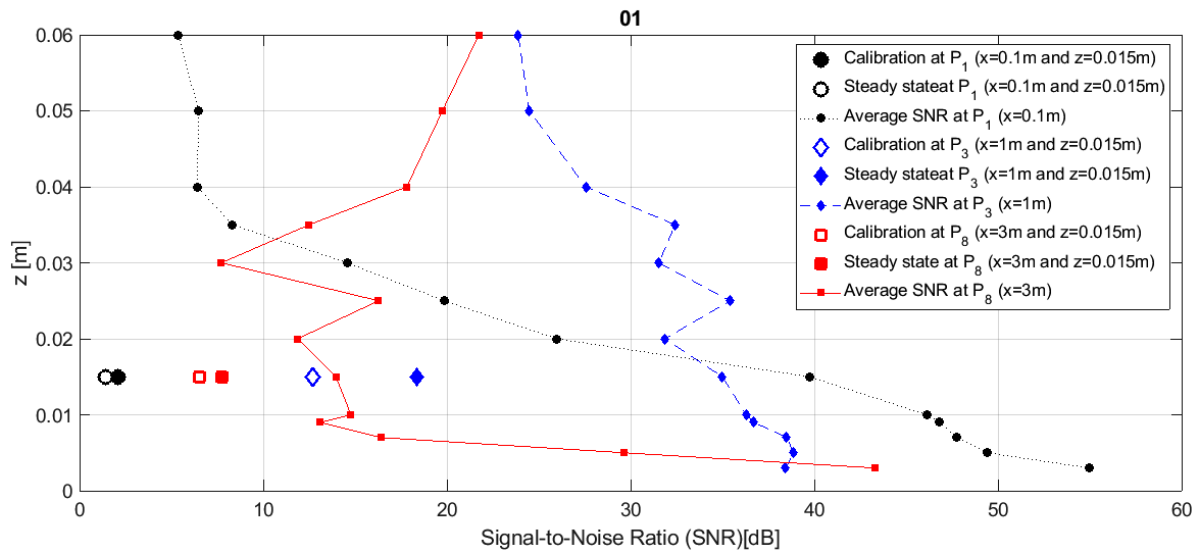


Figure B-0-1 Average signal-to-noise ratio profiles measured at  $x=0.1m$ ,  $x=1m$ , and  $3m$  for Experiment  $S=10$  degrees,  $H=0.25m$  and  $SSC_0=20g/l$ .

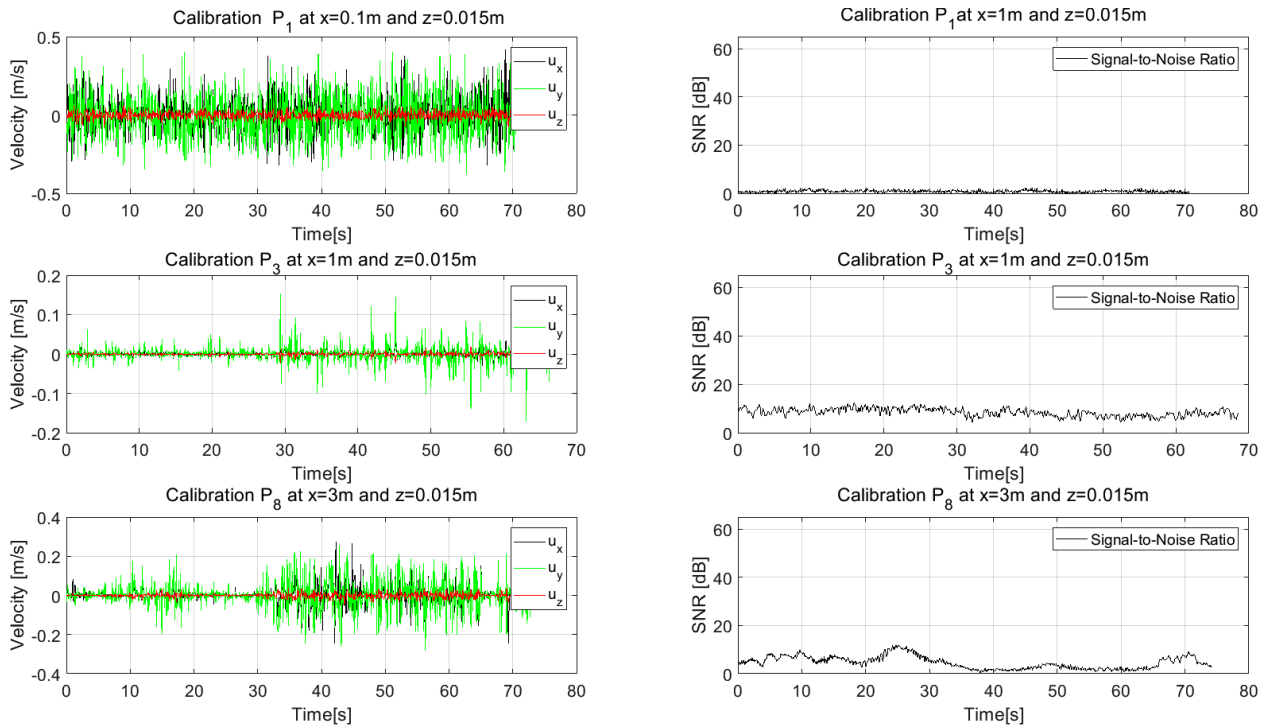


Figure B-0-2. Steady state measurement at  $z=0.015m$  to check the steady state of the plume spreading before the start of the flow velocity and SSC profile.

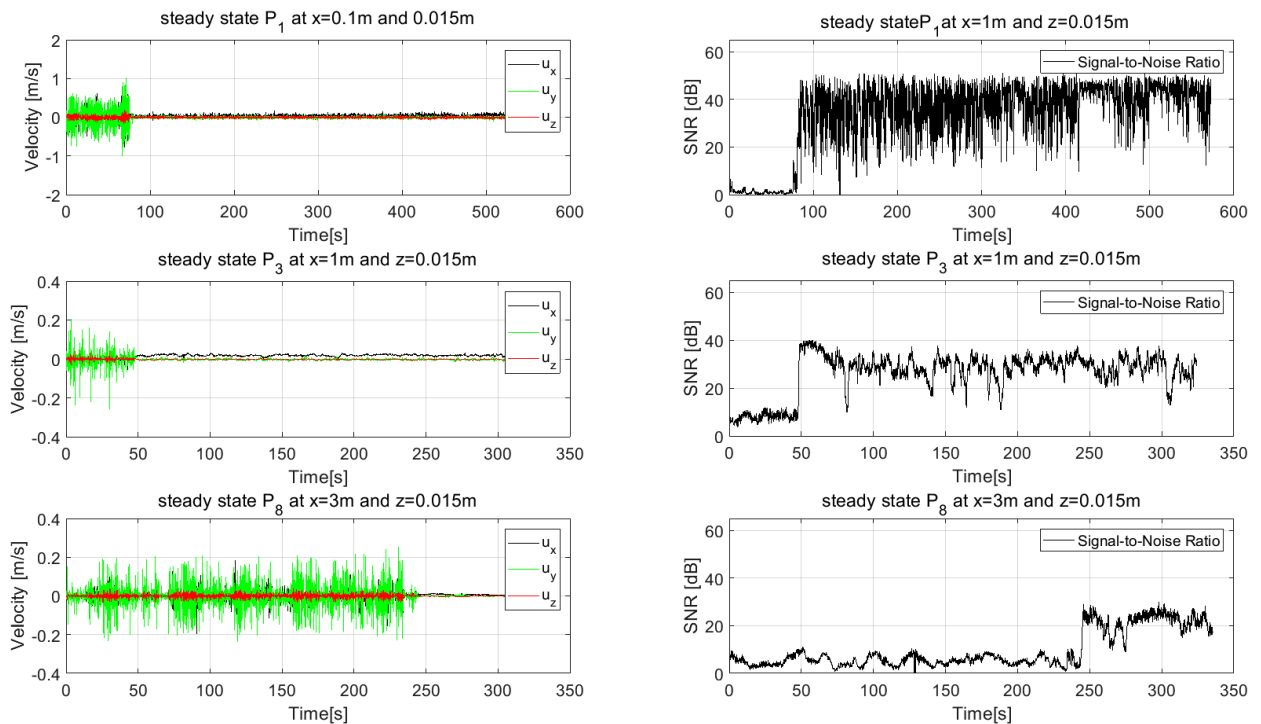


Figure B-0-3 Calibration measurement at  $z=0.015m$  to check the background flow velocity and SSC.

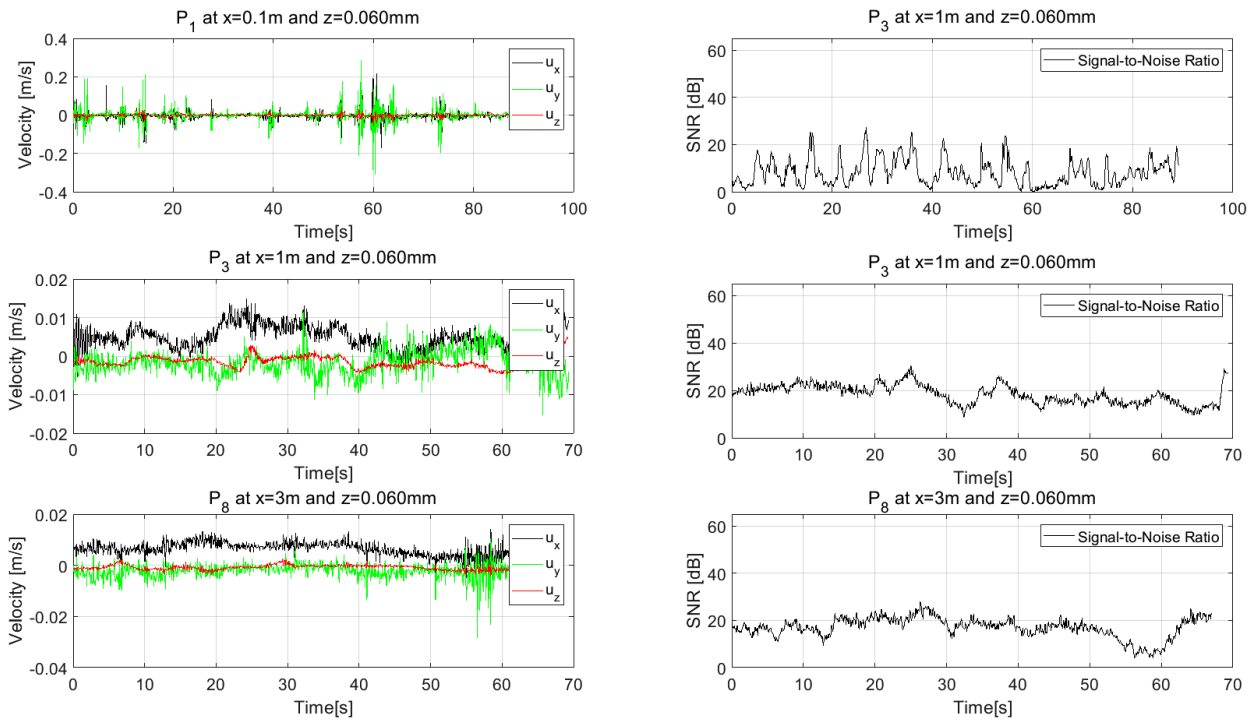


Figure B 0-4. Flow velocity and SNR time series measured at the distance  $x$  from the impingement point at elevation  $z=0.060m$ .

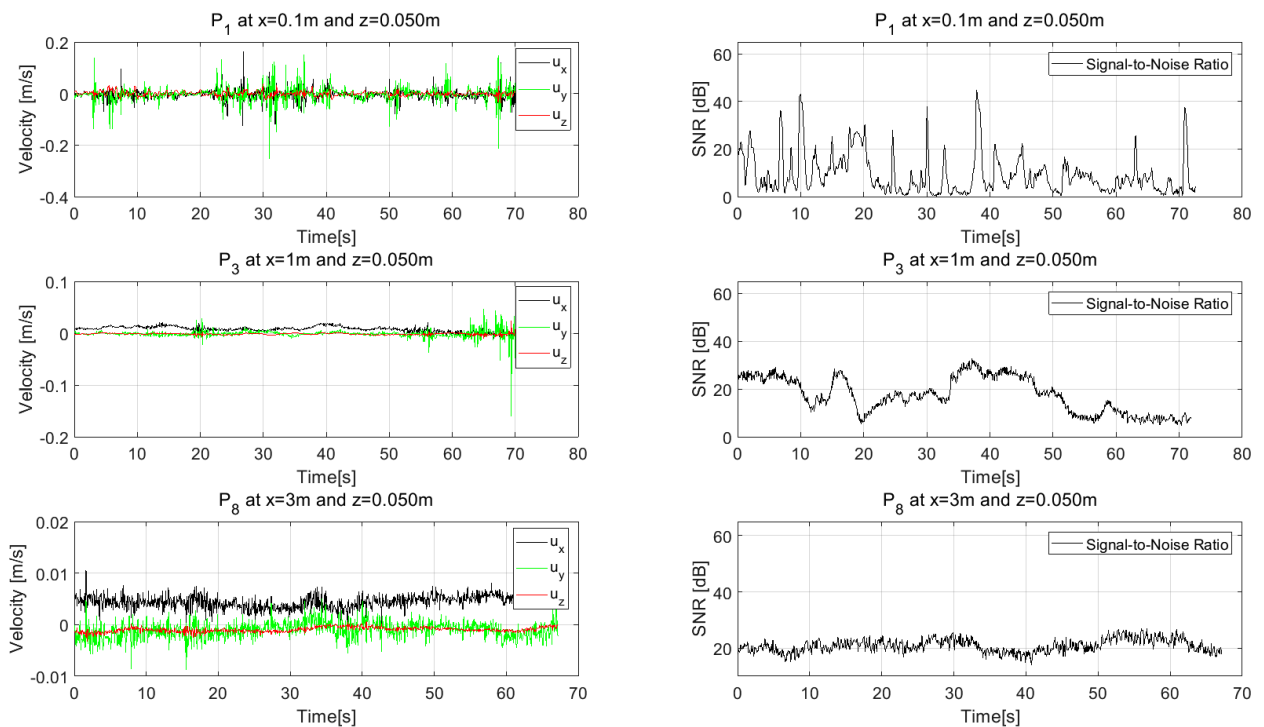


Figure B 0-5. Flow velocity and SNR time series measured at the distance  $x$  from the impingement point at elevation  $z=0.050m$

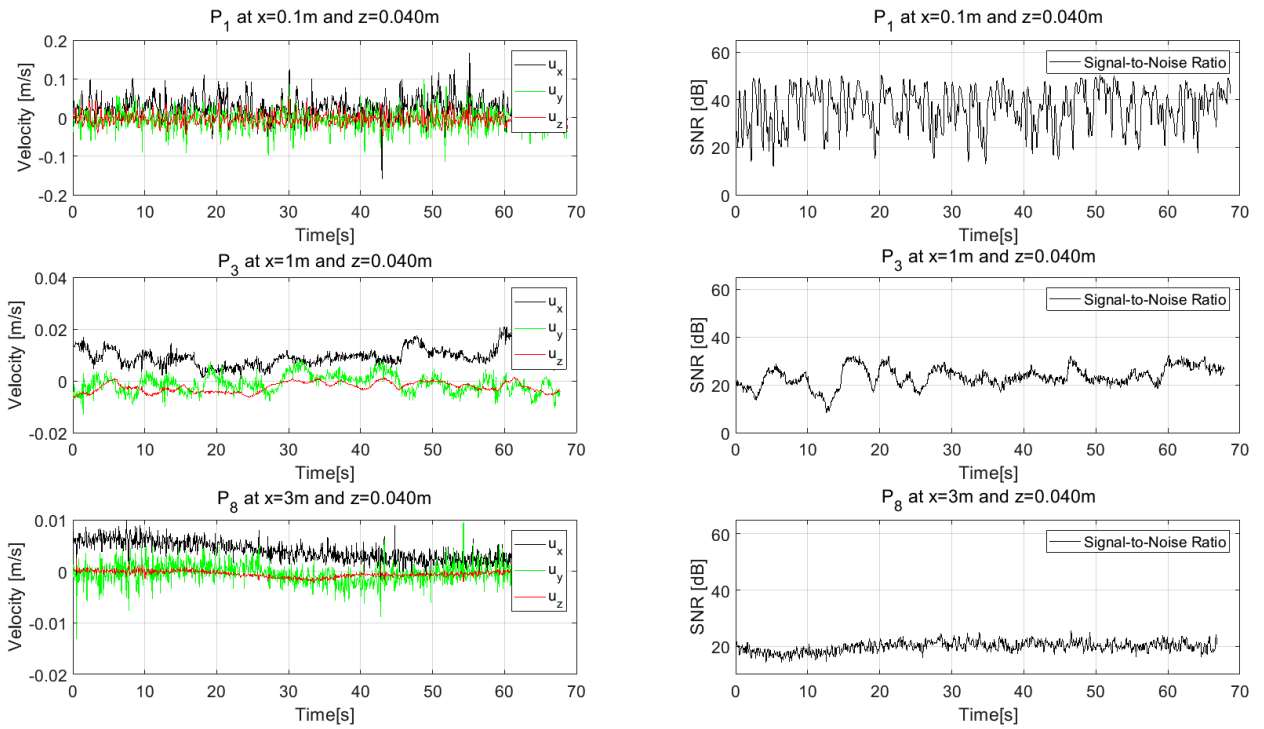


Figure B 0-6. Flow velocity and SNR time series measured at the distance  $x$  from the impingement point at elevation  $z=0.040m$ .

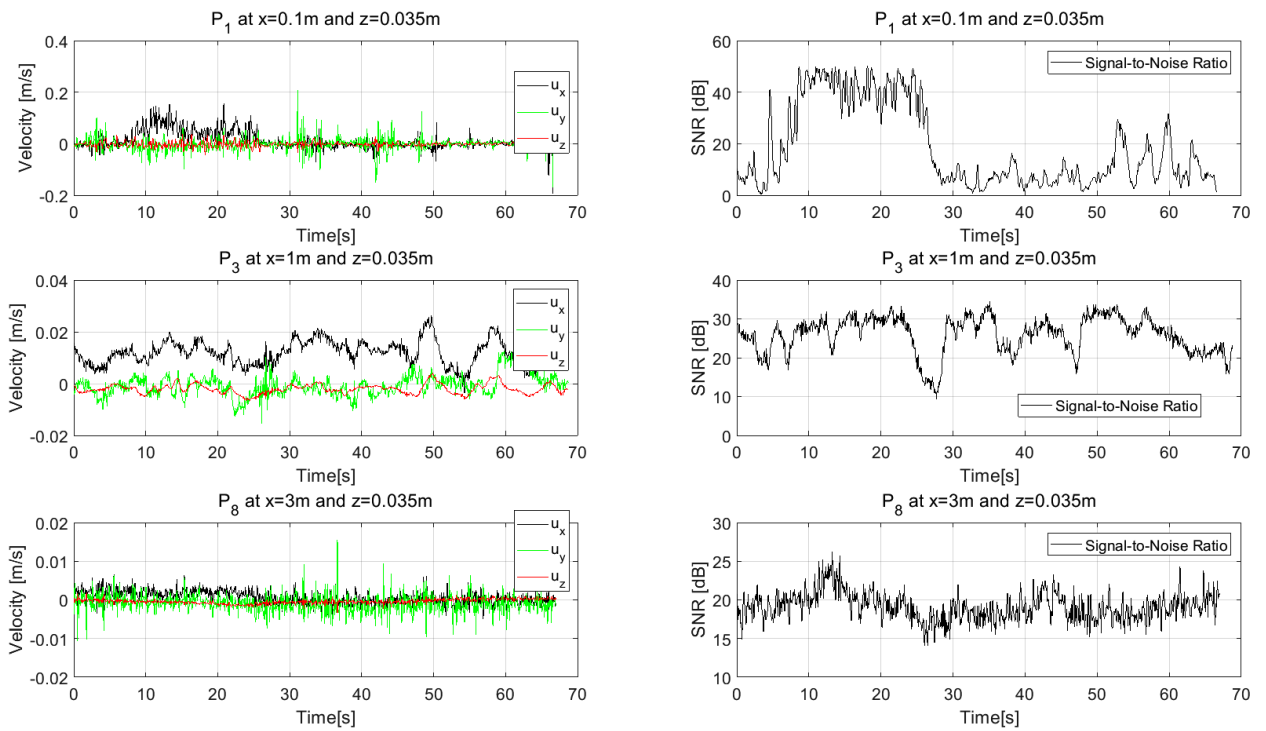


Figure B 0-7. Flow velocity and SNR time series measured at the distance  $x$  from the impingement point at elevation  $z=0.035m$ .

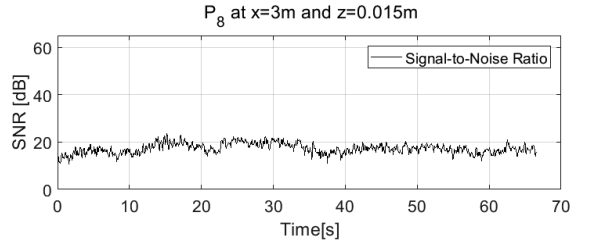
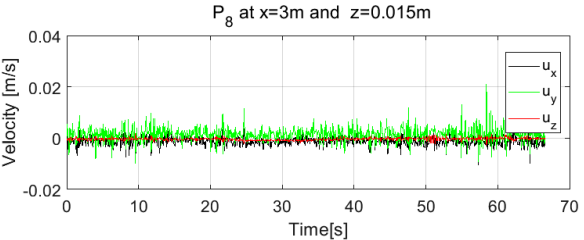
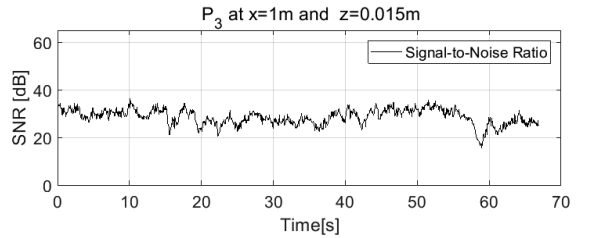
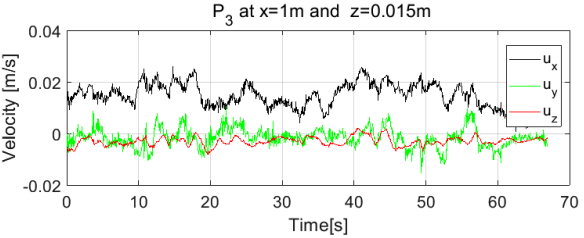
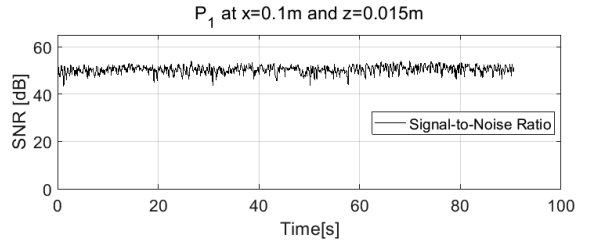
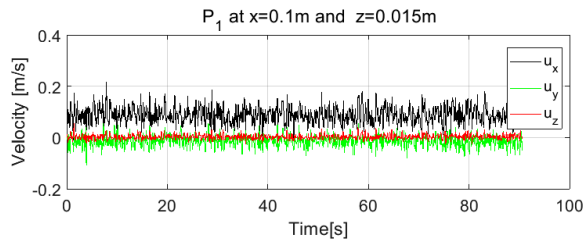


Figure B 0-8. Flow velocity and SNR time series measured at the distance  $x$  from the impingement point at elevation  $z=0.015m$ .

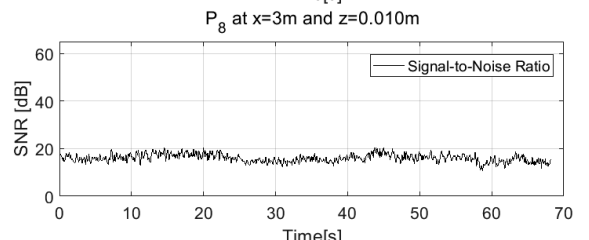
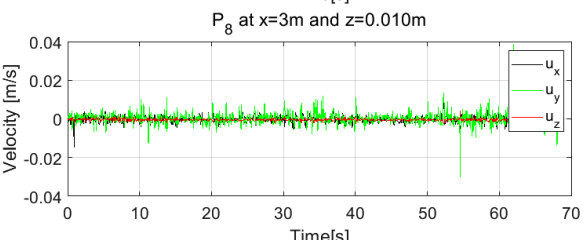
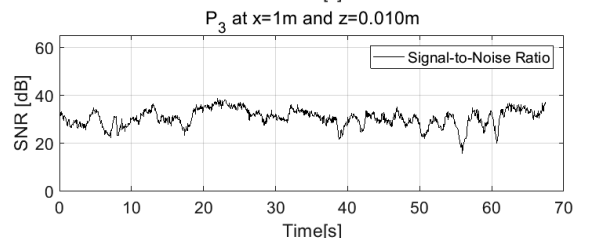
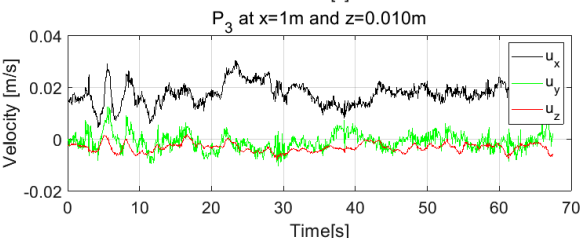
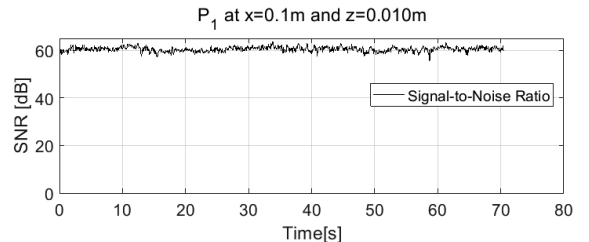
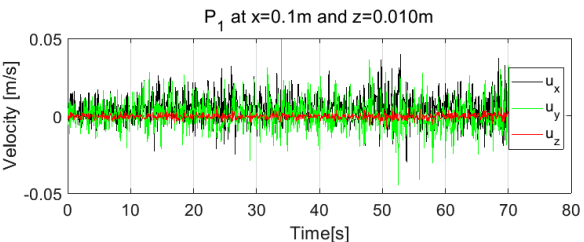


Figure B 0-9. Flow velocity and SNR time series measured at the distance  $x$  from the impingement point at elevation  $z=0.010m$ .

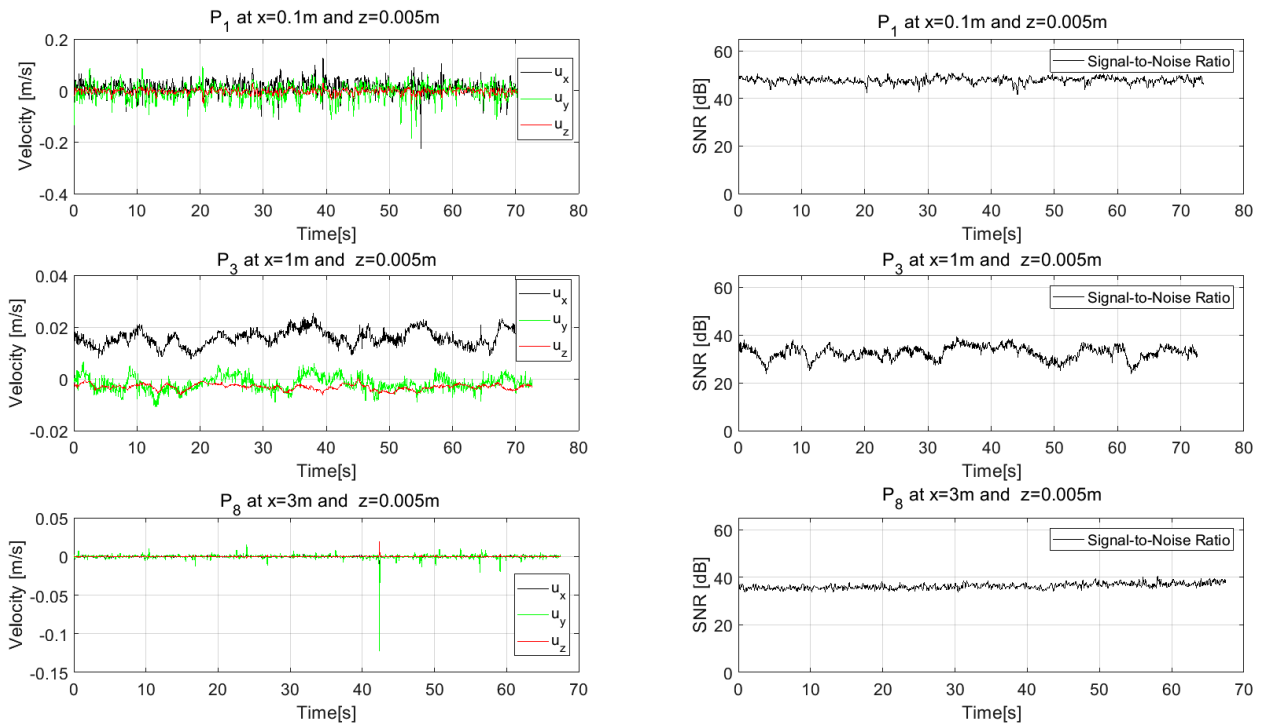


Figure B 0-10. Flow velocity and SNR time series measured at the distance  $x$  from the impingement point at elevation  $z=0.005\text{m}$ .

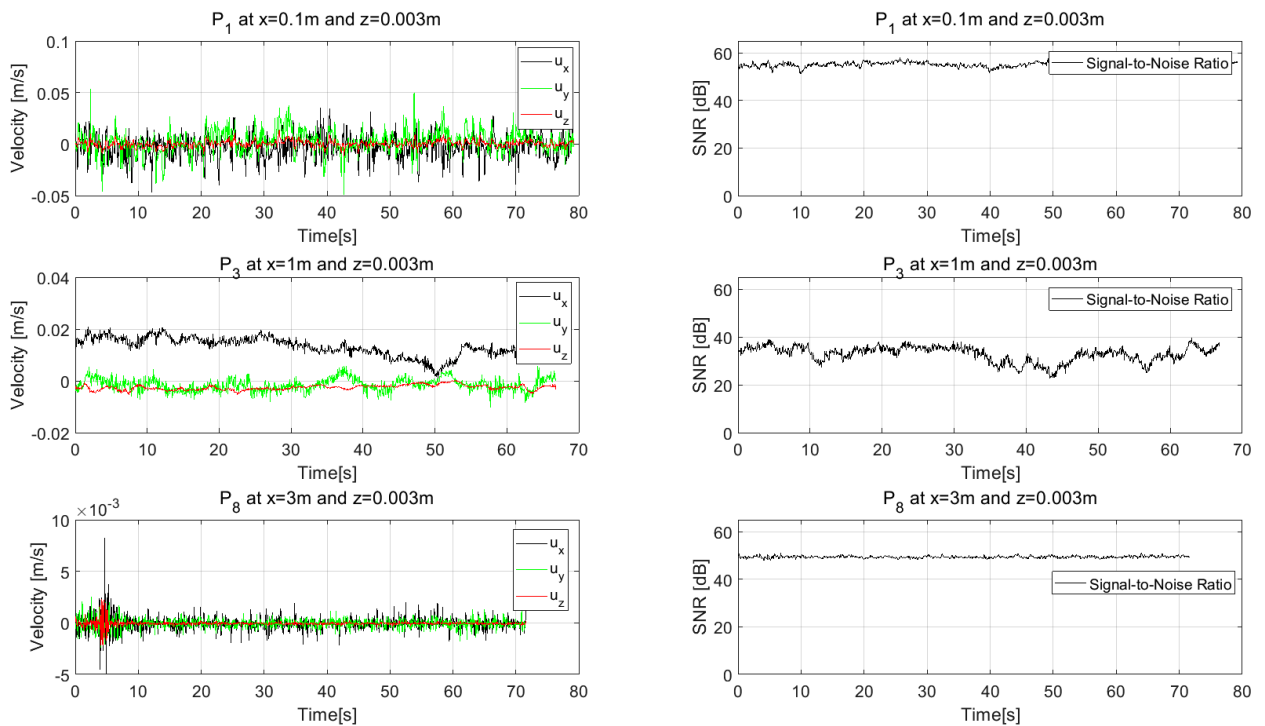


Figure B 0-11. Flow velocity and SNR time series measured at the distance  $x$  from the impingement point at elevation  $z=0.003\text{m}$ .

# APPENDIX C. Granulometric data and physical characteristics

## MILLISIL® M6 - M10

MILLISIL® is produced by iron-free grinding and accurate sieving by means of air-separators. A selected silica sand with a SiO<sub>2</sub>-content of over 99 % is used as raw material. The purity, controlled particle size distribution, chemical inertness, optical properties and hardness make MILLISIL® the performance standard in ceramics, tile-glues, special mortars, refractory material, investment casting,...

### GRANULOMETRIC DATA AND PHYSICAL CHARACTERISTICS

	M6	M10		Method
control-sieve > 63 µm	14	2	%	Alpine
D10	5	4	µm	Malvern MS 2000
D50	30	23	µm	Malvern MS 2000
D90	95	60	µm	Malvern MS 2000
density	2.65	2.65	kg/dm <sup>3</sup>	
bulk density	1	0.9	kg/dm <sup>3</sup>	
specific surface	0.8 2450	0.9 3600	m <sup>2</sup> /g cm <sup>2</sup> /g	BET Blaine
oil absorption	16.5	17.5	g/100 g	
hardness	7	7	Mohs	
loss on ignition	0.12	0.12		
pH	7	7		
colour	L* 90 a* 0.87 b* 4.13	91 0.74 3.57		Minolta CM-3610d D65/10°
refractive index	1.55	1.55		

Technical Data

TDS.03.05.32 2012-06-25 1/2

## MILLISIL® M6 - M10

# Technical Data

### CHEMICAL ANALYSIS (XRF) %

SiO <sub>2</sub>	99.5
Fe <sub>2</sub> O <sub>3</sub>	0.03
Al <sub>2</sub> O <sub>3</sub>	0.20
TiO <sub>2</sub>	0.03
K <sub>2</sub> O	0.04
CaO	0.02



The above given information is based on mean values. The typical properties and chemical analyses are intended as examples and are not to be considered as substitutes for actual testing and analyses in those situations where properties and chemical compositions are critical factors. Sales and supplies will always be according to our general sales conditions.

CAS-Nr.: 14808-60-7

EINECS-Nr.: 238-878-4

MSDS available on request

ed.11

TDS.03.05.32 2012-06-25 2/2

Sibelco Benelux  
De Zate 1 - BE-2480 Dessel  
tel. +32 14 83 72 11 - fax +32 14 83 72 12  
[www.sibelco.be](http://www.sibelco.be)